Dynamic Optimization of Microgrid with Reversible Fuel Cell and Lithium Ion Battery

A Case Study of Kaya Imani Cottages, Msambweni, Kenya

Juri Volodin

Delft University of Technology | Norwegian University of Science and Technology

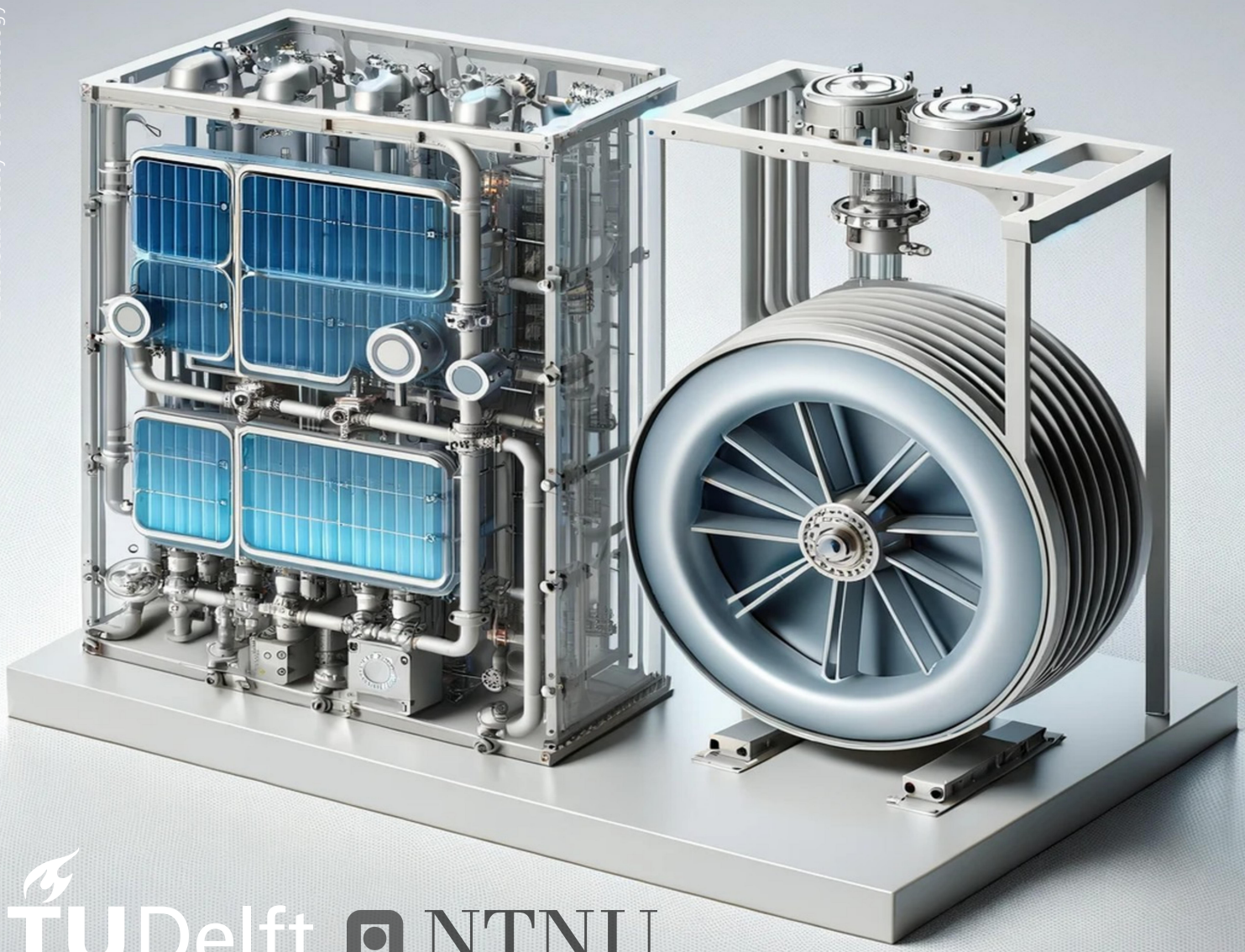

TU Delft NTNU

Dynamic Optimization of Microgrid with Reversible Fuel Cell and Lithium Ion Battery

A Case Study of Kaya Imani Cottages, Msambweni, Kenya

by

Juri Volodin

to obtain the degree of Master of Science

at European Wind Energy Master program at Delft University of Technology and Norwegian University of Science and Technology,

to be defended publicly on July 29, 2024 at 9:00 AM.

Student number at TU Delft:	5850436	
Student number at TU NTNU:	103142	
Project duration:	1st December 2023 – 29th July 2024	
Thesis committee:	Prof. Olimpo Anaya-Lara,	NTNU, supervisor
	PhD Ida Fuchs,	NTNU, co-supervisor
	Asst. Prof. Jianning Dong,	TU Delft, co-supervisor
	Prof. Pavol Bauer,	TU Delft, Committee Chair
	Asst. Prof. Mohamad Ghaffarian Niasar,	TU Delft, Committee Member

Cover: Dynamic Optimization of Microgrid with Reversible Fuel Cell and Lithium Ion Battery

An electronic version of this thesis is available at http://repository.tudelft.nl/.

TU Delft NTNU

Preface

This master's program has been both challenging and incredibly exciting, laying a solid foundation for one of my dreams: making this world a better place by contributing to the development of renewable energy. Over these two years, I have met many inspiring people and formed lasting friendships. Transitioning from my Bachelor's background in Physics, Chemistry, and Material Science to a Master's in Electrical Engineering was initially daunting. I am especially grateful to my coursemates Mark, Sander, Jens, and Julian for their support and companionship during this time, as well as to other friends who made these two years truly unforgettable.

The topic of hydrogen and fuel cells was familiar to me even before I began this degree. Initially, I considered hydrogen to have very limited potential in the sustainable energy revolution. However, as I deepened my knowledge of electrical engineering, I realized that battery storage systems and the electrical transmission grid have their own limitations. This understanding led me to see that the optimal solution lies in combining all these technologies together.

Moreover, I learned that while transmission grids are suitable for traditional energy systems, which largely exclude distributed renewable energy sources, the shift towards renewable energy increases the importance of microgrids. Microgrids alleviate the load on transmission and distribution grids and can function as independent energy islands. A comparison can be drawn between the human body and the electrical system, with blood vessels transporting large amounts of energy similar to transmission lines, and individual biological cells accumulating, consuming, and exchanging energy akin to microgrids. This way the grid stays balanced just as the human body maintains homeostasis. This analogy inspired me to combine these topics in my thesis, exploring the role of new hydrogen developments in microgrids.

My master's thesis was an interesting journey with its ups and downs. I extend my deepest gratitude to my main supervisor, Professor Olimpo Anaya-Lara, for his unwavering support, motivation, and positive attitude, as well as for our stimulating discussions. I am also thankful to Ida Fuchs for proofreading my thesis, significantly assisting with the Kaya Imani Cottages case study, and introducing me to RAMP. I appreciate Lindsay Sanner, the resort owner, for her cooperation and for providing valuable information about the resort's consumption patterns. Furthermore, I thank Assistant Professor Jianning Dong for his help with the thesis, especially in navigating the bureaucratic procedures. I would also like to thank all the thesis committee members.

Lastly, I want to thank my partner Hana for her constant support and my three-month-old son Leon for being such a good boy.

Juri Volodin
Delft, 2024

Summary

This master's thesis investigated the theoretical development and dynamic modeling of an integrated microgrid system using MATLAB/Simulink, where the grid consists of solar panels, lithium-ion batteries, reversible solid oxide fuel cells (RSOCs), and a DC load. The goal was to create an advanced system for improved energy management and grid stability, utilizing MATLAB/Simulink for simulation and analysis, ensuring applicability in diverse locations and varying economic conditions. The research was motivated by the integration of components with different energy and power densities: the high energy density of lithium-ion batteries and the extensive storage capacity of RSOCs. This combination aims to enhance microgrid performance, addressing renewable energy variability and demand fluctuations.

Energy storage plays a crucial role in decentralized generation systems, offering needed capacity and flexibility. This microgrid energy storage addresses two main functions: lithium-ion batteries provide stable supply on an hourly time scale to manage short-term power peaks, while RSOCs secure larger time scales, making the standalone grid completely independent. Hybrid storage architectures, which combine the strengths of single technologies while addressing their weaknesses, are essential for this purpose. Hydrogen, with its low self-discharge rates, serves as a reliable storage medium. It integrates into microgrids through RSOCs, which perform both electrolysis and hydrogen re-electrification. However, due to their operational characteristics, RSOCs have limited quick response capabilities, necessitating a combination with technology that can offer rapid regulation, such as lithium-ion batteries.

In this thesis, a case study was conducted at Kaya Imani Resort in Msambweni, Kenya, with the objective to develop and simulate innovative microgrid solutions. A critical initial step in this process was the generation and analysis of the resort's load profile using RAMP, a Python library designed for creating detailed multi-energy load profiles. This precise analysis was essential as it identified the resort's specific energy requirements and electrical load patterns. After the load profile analysis was conducted, its findings were utilized by a local company for the precise sizing of the microgrid. Concurrently, the thesis shifted its focus, exploring an alternative topology and storage strategy with potential for broader applicability to future microgrid designs, thus diverging from the direct implementation at the Kenyan site.

The thesis successfully developed an integrated model for simulating the microgrid's dynamics, specifically focusing on the incorporation of RSOCs and their combination with lithium-ion batteries, which offer different energy and power densities. The novelty of this work lies in the dynamic modeling of a microgrid using reversible solid oxide fuel cells, an area not extensively covered in existing literature. The model demonstrates that a rule-based control approach for such a microgrid configuration can be reliably utilized, even with the relatively low storage capacity of batteries and the low power capacity of RSOCs. This research highlights the potential for creating a stable and efficient microgrid using this innovative combination of technologies, encouraging further exploration into optimal control strategy development for such configurations.

Contents

Nomenclature

Abbreviations

Abbreviation	Definition
AC	Alternating Current
AEC	Alkaline Electrolysis Cell
AMI	Advanced Metering Infrastructure
ANN	Artificial Neural Network
ANFIS	Adaptive Neuro-Fuzzy Inference System
CB	Circuit Breaker
CHP	Combined Heat and Power
DC	Direct Current
DC Bus V	Direct Current Bus Voltage
DER	Distributed Energy Resource
DNI	Direct Normal Irradiation
ELE	Elevation
EMS	Energy Management System
FBC	Filtration Based Control
FES	Flywheel Energy Storage System
FLC	Fuzzy Logic Controller
GHI	Global Horizontal Irradiation
GTI	Grid-Tie Inverter
GTI_opta	Global Tilted Irradiation at Optimum Angle
HESS	Hybrid Energy Storage System
HF	High Frequency
H-SOEC	Proton-Conducting Solid Oxide Electrolysis Cell
IoT	Internet of Things
Irrad	Solar Irradiance
IV	Current-Voltage
LCOE	Levelized Cost of Energy
LF	Low Frequency
MG	Microgrid
MGCC	Microgrid Central Controller
MLD	Mixed Logical Dynamical
MPPT	Maximum Power Point Tracking
MPC	Model Predictive Control
NFC	Neuro-Fuzzy Controller
O-SOEC	Oxygen Ion-Conducting Solid Oxide Electrolysis Cell
ODE	Ordinary Differential Equation
ode3	Third-Order Runge-Kutta Solver (Bogacki-Shampine method)
P&O	Perturb and Observe
PEMEC	Proton Exchange Membrane Electrolysis Cell
PV	Photovoltaic
PVOUT	Photovoltaic Output
RAMP	Random Access Memory Program
RBC	Rule Based Control
RES	Renewable Energy Source

ROL	Resort Occupancy Level
RSOC	Reversible Solid Oxide Cell
SC	Supercapacitor
SMES	Superconducting Magnetic Energy Storage
SOC	State of Charge
SOEC	Solid Oxide Electrolysis Cell
SOFC	Solid Oxide Fuel Cell
SOH	State of Hydrogen
SVM	Support Vector Machine
TES	Thermochemical Energy Storage

1 Introduction

This chapter introduces the transformative shift in global electricity distribution networks towards the adoption of distributed energy resources (DERs) and microgrids (MGs). It explores the benefits of microgrids, such as enhanced energy efficiency, reliability, and environmental impact reduction, particularly through the integration of renewable energy sources like wind, solar, and hydro. The chapter highlights the technical challenges associated with microgrid implementation, including stability, bidirectional power flow management, and system modeling. It also discusses the evolving landscape of energy storage technologies, focusing on the promising combination of lithium-ion batteries and reversible solid oxide cells (RSOCs) for managing energy needs across different timescales. The overarching aim, hypothesis, and specific technical objectives of the thesis are outlined, detailing the methodologies employed to achieve a stable standalone microgrid capable of reliable, independent operation.

1.1. Background and Motivation

Global electricity distribution networks are being transformed by the adoption of distributed energy resources (DERs) and the creation of microgrids (MGs), which utilize various renewable energy sources. This transformation is shifting the electric power system from traditional, centrally generated power to more localized and resilient configurations. Microgrids can be integrated within existing distribution networks or operate independently in standalone mode, offering greater flexibility and resilience [1], [2].

Microgrids offer significant advantages, such as reducing environmental impact, lowering the need for large-scale power generation infrastructure, improving energy efficiency and reliability, providing backup power through energy storage, and lessening the impact of sudden power outages [3]. Renewable energy sources like wind [4], solar, and hydro are becoming more affordable, offering important benefits, particularly for remote areas, by enhancing local energy independence. This shift is driven by technological progress and environmental considerations, pushing for the integration of renewable energies into the distribution grid.

Introducing microgrids poses several technical challenges, including stability, the need for managing bidirectional power flows [5], [6], system modeling [7], [8], issues with low inertia [9], [10], and dealing with load fluctuations and uncertainty [11], [12]. Microgrids can operate as either DC or AC systems and often involve multiple converters. This versatility and adaptability suggest that microgrids could serve as a model for future energy systems focused on reliability, efficiency, and high-quality power supply [13]. Research in this field covers a wide range of topics, including microgrid classification [14], control methods [15], [16], protection mechanisms, optimization techniques [17], stability, power sharing, and reactive power compensation, reflecting the complex and multifaceted nature of integrating and operating microgrids within the broader electric power system or in standalone mode [18], [19].

The landscape of energy storage technologies is continuously evolving, with recent advancements showing particular promise in enhancing the flexibility and resilience of microgrids. Among these,

lithium-ion batteries and reversible solid oxide cells (RSOCs) stand out as a promising duo for their unique capabilities. RSOCs offer the dual function of efficiently converting electricity to hydrogen and back, providing a sustainable and long-term storage solution, while lithium-ion batteries offer rapid energy discharge and charge capabilities, ideal for managing short-term fluctuations and enhancing system stability, while also assisting RSOC with mid-term fluctuations. The intermittent nature of renewable energy sources like wind and solar necessitates not only the capacity to store excess energy during periods of high production, but also the ability to rapidly respond to fluctuations in energy demand and supply. Hence, this combination of energy storage systems is a promising candidate for future microgrids.

Despite the promising potential of RSOCs, there are notable research gaps that need to be addressed. The technology is still relatively new, and its application in microgrids is limited. While some studies have focused on optimizing the efficiency of RSOCs, their multiphysics simulation, material science, and even optimization algorithms for sizing microgrid components for cost-efficient energy, there remains a significant gap in understanding how to effectively control and integrate RSOCs with other microgrid components. Developing advanced control strategies that can optimize the performance of RSOCs in conjunction with lithium-ion batteries and renewable energy sources is essential for realizing the full potential of this technology in enhancing microgrid resilience and efficiency [20].

1.2. Overarching Aim

The aim of this thesis is to create a stable standalone microgrid that can reliably and independently operate without any connection to a distribution network. This will be achieved by integrating lithium-ion batteries and reversible solid oxide fuel cells (RSOCs) for energy storage, utilizing their complementary characteristics to manage energy storage needs over different timescales. Lithium-ion batteries, with their high power density and fast dynamic response, are well-suited for handling short-term power spikes and rapid fluctuations. They can also manage mid-term storage requirements, providing a buffer for hours of energy supply during periods of intermittent renewable generation. Meanwhile, RSOCs offer a robust solution for long-term energy storage due to their high energy density and ability to efficiently convert hydrogen back to electricity. This long-term capability ensures that energy generated during periods of excess can be stored and used during prolonged periods of low renewable generation. Furthermore, the integration of lithium-ion batteries should not only enhance the microgrid's ability to handle immediate power demands, but also allow for a smaller and more cost-effective RSOC system. By managing the short- and mid-term storage needs with lithium-ion batteries, the RSOC can be optimized primarily for long-term storage, reducing its required size and cost while maintaining overall system efficiency and reliability. This research aims to enhance energy independence and resilience in standalone microgrids, highlighting the hybrid approach's potential as a model for future sustainable energy systems.

1.3. Hypothesis

By integrating lithium-ion batteries and reversible solid oxide fuel cells (RSOCs) within a standalone microgrid and leveraging MATLAB/Simulink for dynamic modeling and advanced control strategy development, it is possible to create a microgrid that is energy efficient and reliable. This system will adeptly manage energy needs across short-term, mid-term, and long-term timescales, ensuring stable and independent operation without relying on a traditional distribution network.

1.4. Research Technical Objectives and Methodologies

Building on this hypothesis, the research aims to achieve several specific technical objectives through a structured methodology. These objectives are designed to ensure the practical implementation and optimization of the standalone microgrid system.

Objective: The first objective focuses on creating a detailed load profile for a case study at Kaya Imani Resort in Msambweni, Kenya. Kaya Imani Resort is a remote eco-resort, providing an ideal case study due to its isolated location, instability of a distribution grid and willingness of the owner to transition to a standalone microgrid powered by renewable sources. Developing an accurate load profile is crucial as it forms the foundation for designing a microgrid that can meet real-world energy consumption patterns.

This load profile will serve a dual purpose: it will be a valuable asset for scientific research, and it will provide critical data to a local company for the precise sizing of a microgrid system.

Methodology: Utilize RAMP, an open-source Python library, for the detailed generation and analysis of the resort's multi-energy load profile. This step involves systematic data collection and analysis to capture the resort's specific energy usage patterns and requirements. The accuracy and granularity of this load profile are crucial for identifying real-world energy demands and consumption behaviors, enabling the design of an optimally sized and configured microgrid. Multiple interviews with the resort owner have to be conducted in order to clarify and integrate in the model the consumption patterns of the resort residents along with the schedules for the electrical devices. Following the creation of the load profile, these insights can be used to assist a local company in determining the correct size and configuration of microgrid components. Additionally, the load profile will be utilized in the next steps to develop a MATLAB/Simulink microgrid model, design control strategies, and optimize performance of the microgrid for efficiency, stability, and resilience.

Objective: The second objective is to develop and size the essential components of the microgrid, including solar panels, RSOCs, lithium-ion batteries, and DC loads.

Methodology: Use MATLAB/Simulink to develop detailed models of the key components, accurately representing their physical behavior. This involves developing MATLAB scripts to simulate the physical characteristics of each component or constructing models using Simulink's basic blocks, or a hybrid of both methods. The parameters will be chosen based on the sizing requirements derived from the load profile to ensure optimal performance and reliability of the microgrid system.

Objective: Integrate the developed models of the microgrid components, including solar panels, RSOC, lithium-ion battery, and DC load, into a comprehensive MATLAB/Simulink model to simulate dynamic interactions within the microgrid.

Methodology: Utilize Simulink's environment to connect the individual component models, ensuring they accurately reflect real-world dynamics. This involves developing local controllers for each component using built-in blocks and custom functionalities to simulate energy conversion, storage processes, and their interactions within the microgrid system, and interconnecting all components to form a functional grid. The integration will focus on evaluating the system's performance in static states and during simple transitions predefined by step functions, ensuring a realistic representation of the microgrid's behavior under common operational conditions.

Objective: Design and simulate advanced hierarchical control strategies within MATLAB/Simulink to dynamically manage the integrated microgrid system, focusing on energy distribution, stability enhancement, and operational efficiency.

Methodology: Implement hierarchical rule-based control algorithms within Simulink. Each energy generation unit will have its own local control, while an overarching control will coordinate the units. Control actions will be adjusted to maintain system stability, optimizing the levels of hydrogen and the state of charge of the batteries. This approach will ensure stable operation even with minimal storage capacity, allowing efficient and reliable performance of the microgrid under varying energy demands and supply scenarios.

Objective: Theoretically evaluate and optimize the performance of the microgrid system using the developed MATLAB/Simulink model, focusing on key metrics such as grid stability and resilience.

Methodology: Perform simulations based on the most hectic day of the year in terms of load profile to test the system for different transitions and realistically demonstrate its characteristics at its extremes. Analyze results to determine the effectiveness of control strategies and to propose improvements based on simulation outcomes.

Summary

In summary, this chapter underscores the significant potential of microgrids in transforming electricity distribution by incorporating DERs and renewable energy sources. It emphasizes the dual benefits of lithium-ion batteries and RSOCs in creating resilient and efficient standalone microgrids. The research

aims to develop a stable microgrid model using MATLAB/Simulink, addressing short-term, mid-term, and long-term energy storage needs. By achieving the outlined technical objectives, the study seeks to demonstrate the feasibility and advantages of a hybrid energy storage system in enhancing the reliability and independence of standalone microgrids, particularly for remote and eco-friendly applications like the Kaya Imani Resort case study.

2

Literature review

This chapter provides a comprehensive review of the existing literature on microgrids and modern energy systems, focusing on their definitions, operational flexibility, and the technologies that enable their effective functioning. It delves into the economic and environmental benefits of microgrids, highlighting their potential for enhancing energy efficiency and resilience. Additionally, the chapter examines the various energy storage systems, including batteries, flywheels, and supercapacitors, and their integration within microgrids. Special emphasis is placed on the Reversible Solid Oxide Cell (RSOC) technology, exploring its capabilities in energy storage and power generation, as well as its integration with other energy storage devices to optimize microgrid performance.

2.1. Microgrids and Modern Energy Systems

2.1.1. Definition

Microgrids are electricity distribution systems that include loads and distributed energy resources (DERs) such as generators, storage devices, and controllable loads. These systems can operate in a coordinated manner, either connected to or isolated from the main power network, as defined by the CIGRÉ C6.22 Working Group [21]. The integration of renewable energy sources (RES) into microgrids is increasingly recognized as a solution to electrical energy deficits, particularly in areas that are difficult to reach by the existing power grids. This approach aligns with global efforts to enhance sustainable and efficient electricity generation [22], [23].

2.1.2. Operational Flexibility and Types of Microgrids

The operational flexibility of microgrids, which can function in both grid-connected and islanded modes, ensures a reliable electricity supply under various conditions, thereby enhancing resilience against grid outages [21]. This flexibility also supports the integration of renewable energy sources (RES), addressing concerns about their variability by using energy storage systems or hybrid systems to maintain the quality and reliability of the supply [22], [24]. Microgrids are categorized into customer-owned, utility or community-operated, and virtual configurations, showcasing the wide range of operational and regulatory frameworks that support these systems. By recognizing the distinct characteristics and potential of each microgrid type, stakeholders can develop strategies to maximize the adoption and efficiency of renewable energy solutions. Such strategic alignment supports the transition to a more sustainable and resilient energy infrastructure as well as ensures that the benefits of distributed generation are fully realized across different scales and contexts of application [21], [22].

2.1.3. Different technologies in Microgrids

The integration of Distributed Energy Resources (DERs), energy storage solutions, and advanced control systems is fundamental to the operation of microgrids. Technologies such as grid-tie inverters (GTIs) enable efficient power transfer between microgrids and the main grid, enhancing system flexibility and stability. Advanced control systems, including Microgrid Central Controllers (MGCC), ensure smooth transitions between operating modes, while protection systems safeguard microgrid compo-

nents against faults, contributing to overall system reliability and efficiency [21], [22], [25].

Additionally, smart meters and advanced metering infrastructure (AMI) provide real-time data monitoring and management, facilitating precise control and optimization of energy use. Energy Management Systems (EMS) are important for optimizing the dispatch of DERs and storage systems, ensuring efficient energy use and cost savings. Communication technologies, such as the Internet of Things (IoT) and wireless sensor networks, enhance the coordination and control of microgrid components.

Advancements in both AC and DC microgrid architecture and control mechanisms have greatly enhanced the integration of various energy sources and storage options. These developments demonstrated the ability of microgrids to efficiently manage energy flows and maintain system stability [22], [26].

2.1.4. Economic and Environmental Benefits

Microgrids present significant economic and environmental advantages. Economically, they enhance energy efficiency by optimizing the generation and distribution of electricity. Through demand-side management and local generation, microgrids reduce overall consumption and decrease the need for long-distance power transmission, minimizing associated losses. Additionally, microgrids provide network operational benefits such as loss reduction and improved voltage control, leading to substantial cost savings [21].

Environmentally, microgrids facilitate the integration of renewable energy sources, thereby reducing environmental impact and contributing to sustainable infrastructure development. This integration lowers reliance on fossil fuels and decreases greenhouse gas emissions, aiding in climate change mitigation. Microgrids also enhance the resilience of energy systems, ensuring stability during outages and climate-related disruptions [22].

A particularly promising aspect is the efficiency improvement through utilizing waste heat from generators in combined heat and power (CHP) systems. These systems capture waste heat from electricity generation for heating or other purposes, significantly increasing the overall efficiency of the energy system. In the context of reversible solid oxide cells (RSOCs), this capability to reuse excess heat is especially noteworthy and promising. Studies have shown that integrating thermochemical energy storage (TES) with RSOCs can effectively mitigate temperature fluctuations during mode switching, significantly enhancing the thermal management of the system [27]. TES materials, such as Co3O4/CoO redox pairs, can store and release heat during the endothermic and exothermic processes of RSOCs, further improving efficiency and reducing energy consumption during standby periods [27]. Despite challenges such as initial costs, regulatory barriers, and market conditions that limit widespread adoption, the potential for efficiency improvements through waste heat utilization in RSOCs represents a largely untapped opportunity that could greatly enhance both economic and environmental outcomes [22], [27].

2.1.5. Stakeholder Impacts and Business Models

The adoption of microgrids affects a broad spectrum of stakeholders, from operators to end-users, offering benefits like cost reductions and improved reliability. They support diverse ownership and operational models, reflective of the various stakeholder interests and the potential for innovative business strategies. Direct benefits include ancillary services provision and investment deferral, while indirect benefits extend to environmental improvements and societal advantages, highlighting the comprehensive value of microgrids in the energy ecosystem [21]. The development of microgrids presents an opportunity for stakeholders to navigate the challenges and leverage the advancements in technology for economic and environmental gains, showcasing a path towards innovative energy solutions [22], [28].

2.2. Microgrid Energy Storage Systems

2.2.1. Introduction

An essential part of a microgrid design is an energy storage system (ESS). In energy storage system frameworks, a variety of storage technologies are implemented to accumulate electrical energy [30]–[32]. The significance of these storage technologies in power systems and microgrids (MGs) lies in

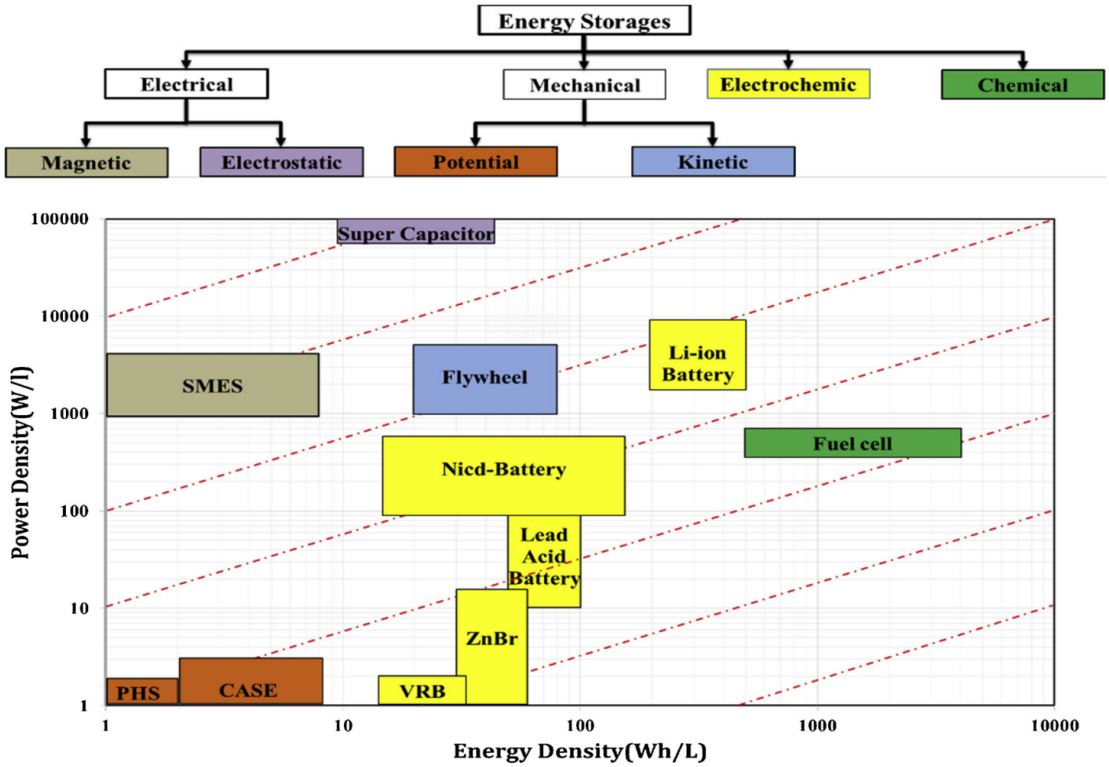

Figure 2.1: Energy storage systems characterized by power density and energy density [29].

their comprehensive coverage of electrical energy storage types, the processes they use to convert energy, and the measures of their operational efficiency [33].

Batteries are recognized for their role in enhancing the stability of electricity networks due to their cost-effectiveness, compact size, and simplicity in deployment [34]. They operate by converting stored chemical energy into electrical energy and vice versa through chemical reactions, with cells arranged either in parallel or series configurations. Different battery technologies demonstrate varied power and energy density capabilities, essential for MG applications, as illustrated in figure 2.1.

For large-scale storage needs, pumped hydro energy storage and compressed air energy storage are notable options. However, their feasibility is often constrained by geographical and environmental prerequisites, posing challenges to their widespread adoption [35], [36]. These systems are effective for bulk energy storage but are limited to locations with specific natural features.

Flywheel energy storage systems, classified under electromechanical storage, comprise components like a back-to-back converter, an electrical machine, a heavy disk, and a dc bus capacitor. Although flywheels offer rapid response times and high power density, their mechanical parts may impact their efficiency and stability [37]–[39]. Research suggests employing superconducting bearing systems to reduce losses and maintenance costs, utilizing a pair of bearings for levitation and stabilization [40].

Supercapacitors (SCs) are known for their capacity in electrostatic energy storage, offering significant benefits such as exceptional recyclability and superior power density. They are particularly useful for applications requiring quick bursts of energy [41]. Concurrently, Superconducting Magnetic Energy Storage (SMES) systems are distinctive for their direct electrical energy storage capabilities. These systems depend on a cooling mechanism, a superconducting coil, and an advanced electrical and control setup tailored for adjusting currents and optimizing storage efficiency [42].

In recent years, hydrogen-based energy storage systems have garnered significant attention for their potential in enhancing microgrid flexibility and sustainability. Hydrogen, as an energy carrier, is produced through water electrolysis using renewable energy sources and can be stored as compressed gas or in liquid form. This stored hydrogen can then be converted back to electricity using fuel cells

when needed, providing a reliable and clean energy supply [43]. The integration of hydrogen storage within microgrids supports the transition to a low-carbon energy system by enabling the effective use of intermittent renewable energy sources such as solar and wind, and by reducing greenhouse gas emissions [43].

Each of these energy storage technologies brings unique advantages and challenges, making them suitable for different applications within microgrids. By leveraging a combination of these technologies, microgrids can achieve higher efficiency, stability, and resilience, ensuring a reliable energy supply in diverse operating conditions.

To further enhance these benefits, hybrid energy storage systems (HESS) combine multiple storage technologies to capitalize on their individual strengths and mitigate their weaknesses.

2.2.2. Hybrid Energy Storage System

Energy storage technologies are characterized by their power and energy densities, which are the main indicators of their performance. Technologies like lithium-ion batteries and fuel cells have distinct advantages and challenges. Lithium-ion batteries, known for their high power and energy densities, can offer a fast dynamic response, making them suitable for applications requiring rapid power control. However, fuel cells, despite their high energy density, present challenges in power control due to their slow dynamic response [44].

Supercapacitors and flywheels also play a role in energy storage solutions. Supercapacitors are capable of meeting high power demands with rapid response times but are limited in their energy storage capacity. Flywheels offer high power density and rapid response but can suffer from mechanical losses and reduced lifespans due to the stress placed on the system [44].

The inherent limitations of individual storage technologies necessitate the development of hybrid energy storage systems (HESS). HESS combine different storage technologies to enhance both transient and steady-state performance. This approach requires a careful selection of storage technologies, power converter topologies, energy management, and control strategies for optimal microgrid operation [45], [46]. By leveraging the strengths of each technology, HESS can effectively manage high power demands while ensuring energy supply security. A typical HESS is depicted in Figure 2.2.

Extensive literature reviews have focused on HESS in various contexts, including electric vehicles and renewable energy sources integration into MGs. These reviews address converter topologies, control methods, and applications, and include a thorough analysis of hybrid storage systems in microgrids and renewable energy systems. [29], [47]–[50].

Microgrids (MGs) and renewable energy systems (RESs) face challenges such as intermittency, poor power quality, stability concerns, frequency control issues, and unbalanced loads. These issues can lead to irregular and frequent discharging/charging patterns in energy storage systems (ESSs), reducing their lifespan and escalating replacement costs[51]. Hybrid Energy Storage Systems (HESS) offer a viable solution to address these challenges, showcasing significant benefits in recent studies[52]–[54]. HESS typically combines high-power storage (HPS) to manage transient and peak power demands, and high-energy storage (HES) to satisfy longer-term energy needs, enhancing overall system efficiency, reducing costs, and extending the lifespan of ESS[55], [56].

Different energy storage technologies, each with unique characteristics, enable a wide range of hybridization possibilities, with combinations like supercapacitors/batteries, SMES/batteries, and FC/batteries commonly applied in RES applications. The selection of HESS configurations depends on various factors, including the goals of hybridization, storage costs, geographical location, and space availability[50].

To mitigate the variability of wind and solar power, researchers have increasingly utilized HESS. By integrating ESS, they aim to smooth out the fluctuations inherent to solar and wind energy sources. Wind power, for instance, consists of various frequency components, and the inclusion of HESS, which can respond at both low and high speeds, allows for more effective smoothing compared to single ESS solutions[57]–[59]. Strategies like capacity configuration based on wavelet transform algorithms for wind power and the use of SMES and batteries for grid-connected wind power generation demonstrate the potential of HESS in improving power quality and grid integration[60], [61].

The lifespan of electrochemical storages, such as batteries and fuel cells (FCs), is a critical concern, often limited by frequent charging and discharging cycles. Strategies to mitigate battery degradation by smoothing power profiles and reducing charge-discharge cycles have shown to extend battery life significantly[62]–[64]. Similarly, the lifespan of FCs can be enhanced by integrating them with high power density storage solutions to manage power fluctuations and fuel consumption more efficiently[65], [66].

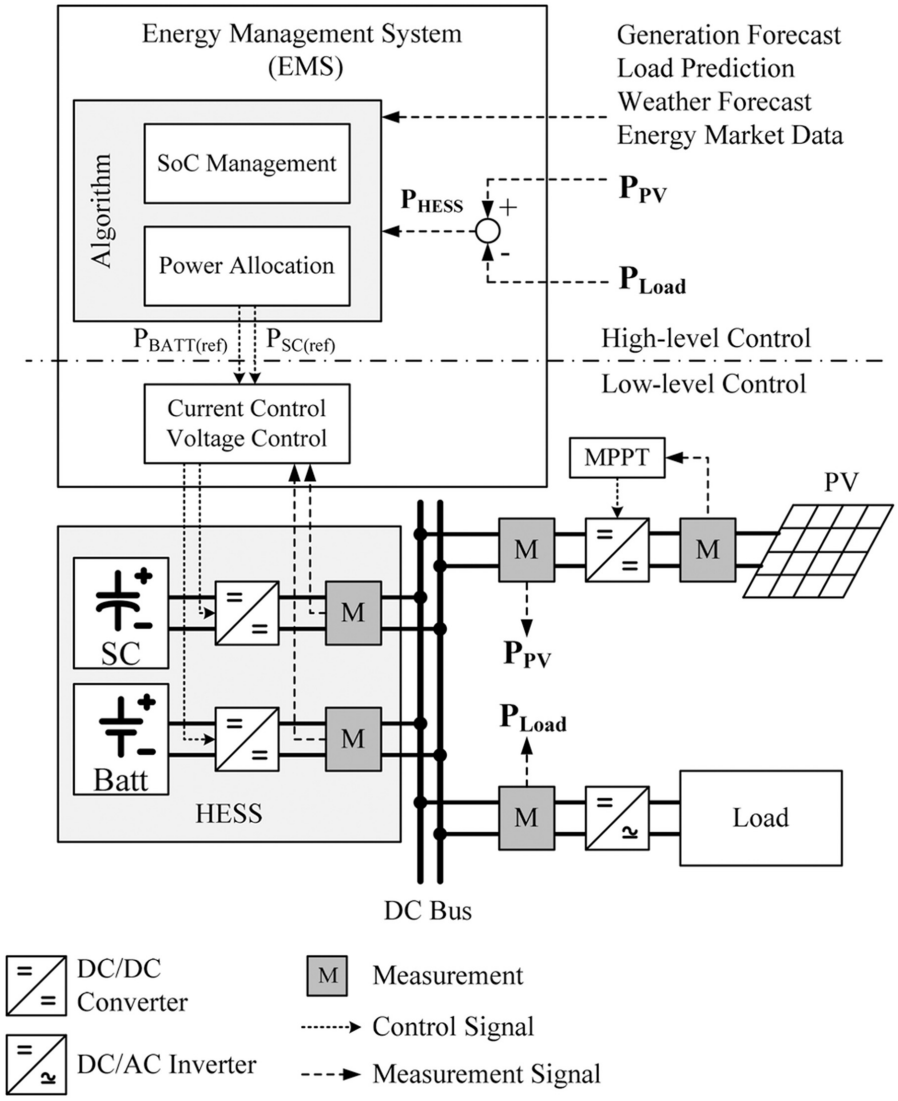

Figure 2.2: Typical EMS structure for standalone PV DC microgrid with parallel active HESS [50].

Hybrid energy storage systems (HESS) significantly enhance power quality by providing solutions for frequency regulation, stability enhancement, harmonic compensation, and voltage regulation in microgrids (MGs). Whether in off-grid or grid-connected systems, HESS helps maintain system frequency and prevent potential blackouts or equipment damage. Novel designs and coordinated operation strategies have been proposed to utilize HESS effectively for these purposes, demonstrating the versatility and necessity of hybrid storage in modern energy systems [67], [68].

For pulsed loads requiring high instantaneous power, integrating high power density storage with HESS can mitigate thermal issues, reduce system volume and weight, and enhance voltage and frequency stability. Control strategies designed for standalone MGs with heavy pulse loads show the benefits of HESS in managing pulsed load impacts and improving overall system performance [69], [70].

In standalone MGs, maintaining a stable and accurate DC bus voltage is paramount. Integrating battery-supercapacitor (SC) storage systems has proven effective for rapid DC bus voltage restoration and

efficient power allocation between the SC and battery. This approach supports isolated systems and enhances DC bus regulation in grid-connected modes, demonstrating the flexibility and effectiveness of HESS in managing voltage levels within MGs [71], [72].

Maintaining high power quality under nonlinear and unbalanced load conditions is essential for MGs. Utilizing HESS can significantly improve voltage regulation and MG performance under these challenging conditions. Coordination control strategies employing HESS have shown promise in enhancing power quality for MGs, effectively addressing unbalanced loads. The application of advanced inverter technology further supports these efforts by reducing harmonic distortion and managing unbalanced AC loads efficiently [73]–[75].

Stability within MGs, encompassing rotor angle stability, voltage stability, and frequency stability, is crucial for reliable operation. HESS can address transient stability issues by providing rapid power support during fault conditions and enhancing the system's ability to maintain synchronization and balance between power production and consumption. Research demonstrates that integrating HESS can significantly improve the transient performance of MGs [76]–[78].

2.2.3. Sizing of HESS capacity

It is necessary to precisely estimate the required storage capacities for the proper implementation of Hybrid Energy Storage Systems (HESS). Different methodologies are utilized for this purpose. Some focus on specific technologies, while others offer more generalized approaches for all storage types. Reviews of these methods have been performed to assist with battery sizing within various renewable energy systems [79]. The process of sizing a HESS must include considerations of total system cost and reliability [80]. Depending on the intended use of the HESS, the methodology for determining capacity may vary. These methodologies are broadly sorted into analytical methods (AM), statistical methods (SM), search-based methods (SBM), which include heuristic methods (HM) and mathematical optimization methods (MOM), Pinch analysis methods (PAM), and Ragone plot methods (RPM).

The analytical method is prevalent in sizing HESS. It entails a systematic examination of power system configurations, tweaking system elements against defined performance criteria to find an optimal solution. Though the essence of these methods is consistent, they may vary depending on the specific HESS technology, the chosen objective function, constraints, and the preferred solution technique. The operation of HESS, as described in a subsequent figure, is contingent upon the disparity between the power output of distributed generations (DGs) and the demand of the load. Should the load exceed the power generated, the HESS discharges energy to meet the deficit. Conversely, surplus generation leads to the charging of the storage systems [29].

In calculating the optimal storage size, various parameters are considered, however ensuring system reliability is the most important. Given the intermittent nature of renewable energy and variable load profiles, the sizing timeframe could range from a single day to an entire year.

The allocation of power is typically such that storages with a high energy density cater to lower frequency demands, while those with high power density address higher frequencies. This allocation can be assessed in either the time or frequency domain. For example, a Fourier transformation-based approach has been proposed for sizing SC-battery HESS in isolated systems, considering the lifecycle cost as the objective function [81]. In another instance, supercapacitors (SCs) and fuel cells (FCs) are paired as HESS, with the power of SCs determined by high-pass filters at varying frequencies [82]. Discrete Fourier transform (DFT) methods are also employed to decompose net power into various time components to inform HESS capacity allocation [83]. Methods considering the life cycle cost, encompassing operation, maintenance, capital costs, efficiency, and estimated lifespan, are also utilized.

A theoretical analytical method has been proposed to provide minimal HESS capacity sizing, independent of topology, technology, application, and control strategy [80]. This approach, while robust, assumes a near-perfect control strategy, simplifying the task to managing an energy balance.

Contrasting with analytical approaches, statistical methods offer enhanced flexibility in sizing energy storage capacities, particularly useful in scenarios with incomplete or varied operational data. One suggested statistical method aims to optimize the combination of storage systems for controlled output power, smoothing out fluctuations in power generated by solar and wind sources [84]. The use of Monte

Carlo simulation is another example where statistical modeling helps ascertain the capacities needed for batteries and supercapacitors within a hybrid setup [85].

Subcategories of SBM like heuristic methods (HM) and mathematical optimization methods (MOM) come into play due to the non-linearity and complexity of the sizing problem. Heuristic optimization methods, such as enhanced simulated annealing and particle swarm optimization, have been deployed to minimize costs effectively [86]. The genetic algorithm has been used for determining the capacity of hybrid storage systems, factoring in the lifecycle cost and replacement expenses of batteries, showing the cost benefits and extended lifespan of batteries when integrated with supercapacitors [87]. Other researchers have used particle swarm optimization (PSO) in combination with DFT analysis to refine HESS sizing, leading to cost reductions [88]. Additionally, methods generating a Pareto-optimal frontier of storage sizes have been proposed to identify the best operational points for various applications [89].

Originating from the heat exchanger network sector, Pinch analysis is a straightforward and adaptable method for determining minimum energy requirements. This computational tool, applicable in renewable microgrids, has been adapted for HESS sizing [90]. It's been used to devise a general HESS sizing strategy for islanded microgrids based on variations in production, load, and storage discharge times [91].

The Ragone plot, typically used to assess the performance of various energy storages, has been incorporated into HESS design strategies [92]. This method contemplates the lifecycle maximization of storage, with Ragone plots serving as constraints to acknowledge the interplay between rate capability and storage capacity. The significance of aligning storage sizing with real-time operation strategies has been recognized, suggesting a more comprehensive understanding and solution when both are considered concurrently [93].

The selection of a suitable capacity sizing method is influenced by several factors, including data availability, the nature of the sizing problem (linear or nonlinear), the dynamics of generation and load, and the inclusion of HESS dynamics and constraints. SBM methods are commonly chosen due to their versatility in handling various objective functions and solving complex, nonlinear problems.

2.2.4. HESS Topologies

The configuration of interconnection topologies for High-Power Storage (HPS) and High-Energy Storage (HES) significantly impacts the control flexibility, dynamic performance, efficiency, and lifespan of Energy Storage Systems (ESS). These can be integrated into the system either directly or through power converters, with direct connections being more straightforward, less costly, and having simpler control complexities. Conversely, using power converters can lead to enhanced power regulation due to the decoupled control of HPS and HES [94], [95]. HESS may be connected to the DC bus directly or interfaced with the AC bus using a separate DC-AC converter. The selection of topology is influenced by system requirements and energy management functions and is categorized into passive, semi-active, or active [96], [97].

Passive Architecture

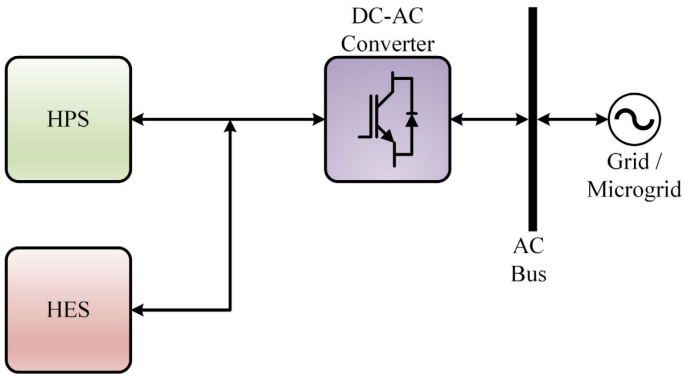

Figure 2.3: Passive Topology Interconnection [97].

The passive architecture is the simplest form of interconnecting HPS and HES to the system. ESS are directly connected together without power converters [98], [99]. The matching of voltage levels of ESS to the DC bus or load voltage is essential [96]. The passive architecture resembles parallel operating synchronous generators, where load sharing is based on impedance ratios. Similarly, in ESS, the load is shared based on the internal resistance and its output characteristics, affected by temperature and the state of charge.

In a battery and SC hybrid, the high-power pulses are absorbed by SC due to its low impedance, functioning like a low pass filter. The charging and discharging characteristics offer poor regulation of voltage and load due to considerable variation. The power balance of the system is governed by [97]:

$$P_{\text{gen}} \pm P_{\text{hess}} = P_{\text{load}} \tag{2.1}$$

with the power exchanged by HESS being the sum of power from HPS and HES:

$$P_{\text{hess}} = P_{\text{hps}} + P_{\text{hes}} \tag{2.2}$$

Semi-Active Configuration

The semi-active configuration enhances the passive topology by introducing a single power converter, specifically a bidirectional DC-DC converter, to manage the power output of the High-Power Storage (HPS). This modification brings an additional layer of control, allowing for refined management of power flow from the HPS, thereby aligning it more closely with system demands. The inclusion of a control algorithm enables precise modulation of the power, ensuring that peak power requirements are reliably met by the HPS, with the High-Energy Storage (HES) accommodating the continuous, less variable demand.

The mathematical relationship governing the power exchanged by the Hybrid Energy Storage System (HESS) in this topology is expressed as [97]:

$$P_{\text{hess}} = \alpha P_{\text{hps}} + P_{\text{hes}} \tag{2.3}$$

where α is a coefficient representing the degree of controllability over the HPS, which directly influences how much power the HPS contributes to the overall system.

This semi-active approach has been scrutinized in various studies, particularly examining scenarios where supercapacitors (SC) are used to absorb large power pulses due to their low impedance, effectively acting as a buffer against sudden power demands. In configurations where the battery is controlled, there is a need to account for voltage variations along the DC link, necessitating higher energy storage capacity to stabilize the DC bus voltage [97], [100].

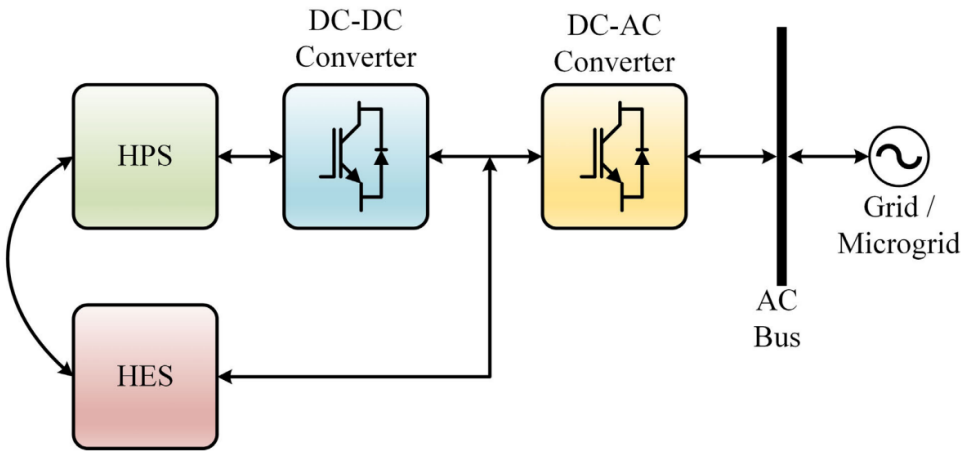

Figure 2.4: Semi-Active Topology Interconnection [97].

A practical application of this topology is observed in isolated microgrids, where a hybrid of battery and Superconducting Magnetic Energy Storage (SMES) supports Wind Energy Systems (WES). In these settings, SMES significantly extends the battery's operational life by absorbing high-frequency power variations, thus reducing the stress on the battery during transient conditions. Similar setups with battery-SC hybrids have been employed to mitigate the fluctuations inherent in small-scale WES, with the SC connected via a bidirectional DC-DC converter and the battery directly connected to the DC bus [101].

However, the semi-active topology is not without its limitations. When HPS is directly connected to the system, it can cause fluctuations in the DC bus voltage, which may lead to stability issues. Additionally, the DC-DC converter must be robust enough to handle significant power spikes, which can be a design and cost consideration [97].

Active Topology

The active topology employs individual bidirectional DC-DC converters for both HPS and HES, offering maximum control flexibility and independent operation of each ESS [102]. This setup supports a broad range of control strategies to optimize the complementary characteristics of HPS and HES. The power exchanged by HESS is expressed as [97]:

$$P_{\text{hess}} = \alpha P_{\text{hps}} + \beta P_{\text{hes}} \tag{2.4}$$

Here, α and β are controllability factors for HPS and HES respectively, dictated by various factors including SOC and battery degradation rate [103].

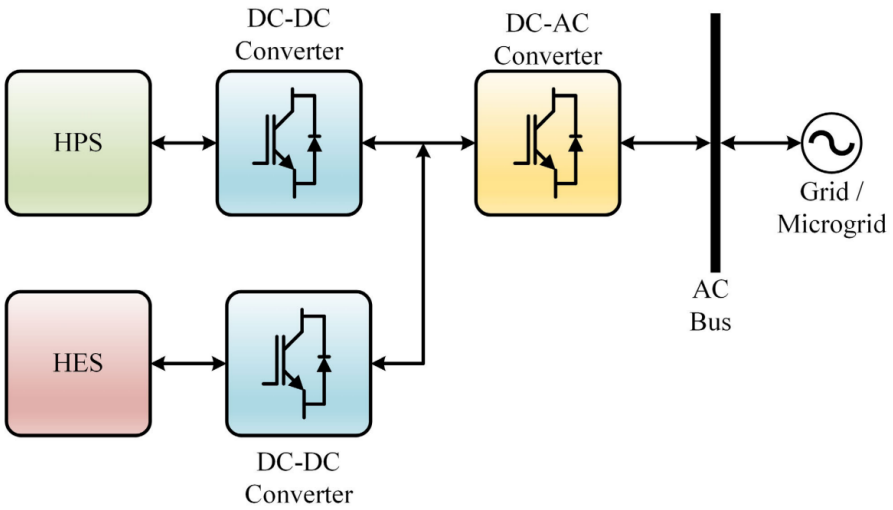

Figure 2.5: Active Topology Interconnection [97].

2.3. Control Strategy

2.3.1. Classical Control

The selection of a suitable control technique for HESS hinges on several factors, such as enhancing storage longevity, minimizing power fluctuations, maintaining power quality, controller response times, cost, and the hybridization architecture. Energy Management Systems (EMS) are implemented on two levels: a lower level that regulates DC bus voltage and current flow, and a higher level that manages power allocation, State of Charge (SOC) monitoring, and other systemic objectives [104], [105].

For off-grid systems, HESS objectives include optimizing microgrid performance, bolstering system stability, and curtailing operational costs. Various techniques have been proposed to meet these objectives, which are categorized in this discussion as either classical or intelligent control strategies.

Filtration Based Control Techniques

In these systems, power transfers between ESS are split into High Frequency (HF) and Low Frequency (LF) components. HF components typically result from sudden load variations or irregular power generation, while LF components occur during the predictable behavior of RES. Fast-responding ESS handle HF components, whereas LF components are suited for ESS with higher energy density[106]. Filtration Based Control (FBC) utilizes filters to segregate the power demand into LF and HF components, smoothing out battery current fluctuations. For example, Kollimalla et al. developed a Low Pass Filter (LPF) based FBC EMS to manage battery charge levels, evaluated to prolong battery lifespan, offering quick dynamic response and reduced computational demands[72].

Rule Based Control Techniques

Rule Based Control (RBC) involves decision-making processes based on a set of predetermined rules, derived from system expertise or mathematical models. Thermostat-based approaches are simple RBC methods, where high energy storage operates within specified SOC limits. An advanced state machine control method, which incorporates multiple rules informed by heuristics or expertise, has also been introduced, focusing on optimizing power flow and system operation across different regions[107]. RBC techniques are favored for their simplicity, low computational requirements, and ease of implementation[108]. However, their practical application can be limited, especially when relying on filtered wind speed and solar irradiation levels, which may not be feasible in real scenarios[109].

Dead Beat Control

Deadbeat control leverages the system model to adjust the duty cycle ratio, minimizing regulation error within one control cycle. This technique effectively manages power sharing between ESS, ensures fast dynamic response, and maintains high control accuracy. It incorporates features of conventional controls, like straightforward implementation and process integration. Wang et al. employed deadbeat control to regulate SC response to transient power demands, thus prolonging battery life[110].

Droop Control

Droop control strategies, such as those based on High Pass Filter (HPF) droop controllers, are used to regulate batteries and SCs. These hybrid controllers provide solutions for effective power sharing, voltage fluctuation mitigation, and SOC limitation for both battery and SC[111]. Another droop control approach, the Voltage Integral Droop (VID), has been developed to handle power management between SC and battery, managing both LF and HF power sharing. Nonetheless, VID may struggle with voltage deviation control, which has been addressed by incorporating a Secondary Voltage Recovery (SVR) controller for batteries to regulate bus voltage[112]. The integration of cache control with adaptive droop has been implemented to synergize PV and wind systems with HESS, focusing on online SOC management and long-term battery operation[113].

Sliding Mode Control

Sliding Mode Control (SMC) is a nonlinear control method that switches between control laws based on the state vector. Abeywardana et al. improved SMC by addressing the issue of variable switching frequency, reducing power dissipation and design complexity[114]. An adaptive SMC with hysteresis control has been proposed to manage multimode HESS, addressing current fluctuations[115].

2.3.2. Intelligent Control

To surmount the constraints inherent in classical control-based Energy Management Systems (EMS), intelligent control techniques such as adaptive predictive maximum power (PMP), meta-heuristics, and Model Predictive Control (MPC) have been developed for HESS energy management. These systems exhibit enhanced control performance but come with the drawbacks of increased computation time and higher costs[116].

Model Predictive Controller (MPC)

MPC is an advanced optimization technique that forecasts future plant states to optimize current controls while considering future constraints. Its primary advantage lies in its anticipatory nature, which allows it to take preemptive action [97]. In a study addressing off-grid wind/PV hybrid energy storage systems (HESS), MPC was employed to monitor the state of charge (SOC), adapt to load fluctuations,

and manage hydrogen storage levels. The outcomes from this simulation suggested that the approach led to a 12.23% and 14.65% boost in battery capacity and overall system efficiency, respectively, compared to traditional state control systems[117]. Additionally, MPC has been integrated with a Mixed Logical Dynamical (MLD) system to manage the intricate dynamics of HESS, presenting a refined control strategy that has the capability to handle multiple control variables across extensive systems[118].

A notable application involved a hybrid setup of fuel cells and supercapacitors (SC), governed by MPC to manage direct parallel connections to the load and a DC-DC converter-linked fuel cell. Nonetheless, the approach demonstrated constraints, including the inability to accommodate gradual changes in current to the power sources, potentially affecting system performance due to swift current variations and the reliance solely on a primary model of the SC for controller design, without considering an actual DC-DC converter. Moreover, the system's efficiency was only gauged through simulations, not real-world application, with a major limitation stemming from the reliance on the system's mathematical model[119].

MPC has also been formulated for a combination of SC and batteries, ensuring the SOC remains within defined thresholds and offering structured guidelines for controller operations. Despite these advancements, the proposed method faced computational challenges due to the dual state-space models for the converters and lacked the capability to regulate DC bus voltage[120]. Progressing the initial concept, a less complex controller was proposed, suited for HESS management, yet its simplification—assuming constant DC bus voltage—posed practicality issues in real-time DC microgrid environments [121].

Neural Network and Fuzzy Logic

In order to balance between complexity and efficiency, innovative real-time Energy Management Systems (EMS) leverage intelligent techniques like fuzzy logic and neural networks, as well as reinforcement learning, to circumvent the constraints of classical controls[122]. Fuzzy Logic Controllers (FLC) and Artificial Neural Networks (ANN) surpass traditional methods by enhancing dynamic system behavior without necessitating an exact system model[123]. They improve system dynamics without the need for precise models but do not assure optimal performance[124].

ANNs, which model complex relationships within data through layers of interconnected 'neurons,' are celebrated for their nonlinear processing, adaptability, and system parameter independence, making them a prime choice for control systems[125]. The downside of ANNs, attributed to their 'black-box' nature, is the lack of transparent rules for their internal structure and the necessity for historical data to train the network effectively[120], [121]. This complexity can pose a barrier, particularly when extensive training datasets are involved[126].

Contrastingly, FLCs are more interpretable and less sensitive to parameter changes. They work based on rule-based algorithms and membership functions (MF), and do not require an exact mathematical model or an extensive training process. However, devising FLC's MF can be a time-consuming trial-and-error ordeal that may not yield optimal outcomes, especially as system complexity increases[127].

Multi-mode fuzzy-based controllers have been proposed to rectify limitations in other methodologies that overlook the effect of SOC[128]. These controllers have been validated across short and long-term situations, with FLCs being assigned to different power-sharing modes to address issues like battery efficiency and aging.

Neuro-Fuzzy Controllers (NFC) harness the rule inference capability of FLCs and the parallel data processing excellence of ANNs. NFCs use neural learning rules to define and fine-tune the MF of FLCs, enhancing the fuzzy model's accuracy over time[129]. In large-scale applications, Adaptive Neuro-Fuzzy Inference Systems (ANFIS) have been employed, where the MF of FLC are adjusted through back-propagation, demonstrating improved battery efficiency and overall system performance when benchmarked against Rule-Based Controls (RBC)[130].

Optimization-Based Methods

Besides controllers using FLC and ANN, recent advances in control techniques have seen the implementation of optimization-based methods for the proficient governance of HESS. Notably, bio-inspired algorithms have shown promise in adeptly managing multi-objective functions and delivering optimal solutions, a testament to their versatility across various application domains[131]. Consequently, the integration of FLC with optimization algorithms has been pursued to establish effective rule frameworks.

Particle Swarm Optimization (PSO) is a method that iteratively converges on a solution by simulating the social behavior of particles. This approach was validated for an off-grid PV/Wind HESS, where PSO fine-tuned the FLC's membership functions, demonstrating substantial operational and maintenance (O&M) and Loss of Power Supply Probability (LPSP) cost reductions compared to unoptimized systems[132]. Inspired by the natural water cycle, the Water Cycle Algorithm (WCA) has been adapted to FLC for off-grid HESS optimization, yielding further cost reductions in LPSP and O&M [133].

Chia et al. put forward a predictive energy management system utilizing Support Vector Machine (SVM) for a battery/supercapacitor HESS. This system anticipates load demands with notable accuracy, mitigating battery strain and thus prolonging battery life by preemptively engaging the supercapacitor before peak demands[55]. However, the control over the supercapacitor's power output remains a challenge.

Additionally, predictive management for a battery HESS tailored to off-grid wind power systems has been developed. This method dynamically adjusts the operation of batteries and fuel cells based on wind forecasts and load profiles, thereby averting potential blackouts due to insufficient wind or energy reserves[134]. Despite its innovativeness, this approach's application is curtailed by its reliance on predefined thresholds.

A hybrid on-grid HESS featuring predictive control has been devised, which uses forecasts of various parameters, including photovoltaic output and electricity prices, to optimize daily and weekly FLC settings through SFL and PSO[135]. This system shows improvements in both SOC maintenance and operational costs over regular periods.

Moreover, an optimization-based EMS utilizing Multi-Input Adaptive Droop (MIAD) has demonstrated fewer iterations to meet objectives, focusing on curbing battery current fluctuations and minimizing energy loss from supercapacitors[136].

Unified Controller

Tummuru et al. have pioneered a unified Energy Management System (EMS) tailored for DC microgrids equipped with Hybrid Energy Storage Systems (HESS), demonstrating its efficiency in prolonging the life expectancy of supercapacitors (SC) and batteries under a variety of operational conditions [137]. This unified approach has been shown to outperform previous EMS models, particularly in terms of voltage control, and the rates of charging and discharging batteries, not to mention the reduction in processing time [138]. Similarly, the unified controller model proposed in another study emphasizes rapid dynamic voltage regulation, effective power distribution despite disturbances, minimization of battery charge/discharge rate fluctuations, and overall improvement of power quality [139].

Further research in the field has led to the development of supervisory power management systems for HESS within hybrid microgrids, focusing on the interplay between the grid and the microgrid [140], [141]. These studies evaluate the capacity of HESS to navigate varying conditions presented by photovoltaic systems and the grid.

2.4. DC vs AC microgrids

The modernization of energy systems is driven by the need for higher efficiency, reliability, and integration of renewable energy sources. Microgrids (MGs) are becoming increasingly important, offering flexible and configurable solutions for energy distribution.

In terms of operating current, there are three main types of microgrids: direct current, alternating current and hybrid microgrids. In Figure 2.6 you can observe a hybrid microgrid, which consists of DC and AC sub-microgrids.

DC microgrids are gaining prominence due to their higher efficiency and reduced energy losses from eliminating multiple power conversion stages. For example, DC microgrids can achieve efficiency improvements of up to 10-15% compared to traditional AC systems [13]. They are widely applied in industries such as avionics, automotive, marine, and manufacturing, supporting modern electronics and renewable energy systems [13]. The Residential DC Innovation Hub at TalTech exemplifies these benefits by demonstrating up to 20% energy savings, 30% reduction in raw material use, and 20% reduction in lifecycle costs for buildings fully converted to DC [142].

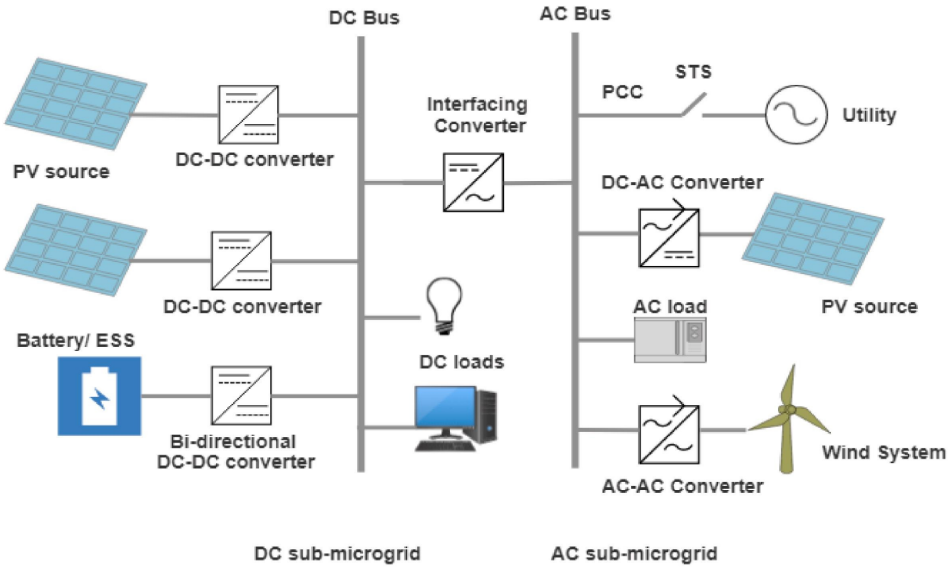

Figure 2.6: Schematic of DC and AC sub-microgrids [143].

AC microgrids, extensively researched and implemented globally, integrate renewable-based distributed generation (DG) units like wind turbines, solar PV arrays, and fuel cells. These systems maximize energy generation through advanced control techniques and require AC/DC power converters for DC-based DG units and loads [13].

DC microgrids simplify the connection of DC-based DG units and loads, offering higher efficiency, reduced system size, and lower costs compared to AC microgrids. They eliminate issues related to frequency synchronization and reactive power, making them advantageous for future energy systems dominated by DC loads and renewable energy sources [13].

In conclusion, DC microgrids are increasingly preferred for modern applications with high DC load demands and renewable energy integration, while AC microgrids remain valuable for leveraging existing infrastructure and standards. The choice between AC and DC microgrids depends on specific application requirements and the need for efficiency and reliability in energy distribution [13].

2.5. Reversible Solid Oxide Cell

2.5.1. Solid Oxide Fuel Cell

The increasing global energy demand alongside the urgent need to reduce carbon emissions has accelerated the search for efficient and sustainable energy solutions. Among various technologies, fuel cells, particularly solid oxide fuel cells (SOFCs), have emerged as a significant contender due to their high efficiency and fuel flexibility. SOFCs directly convert the chemical energy of a fuel into electrical energy via electrochemical reactions, bypassing the inefficiencies of the Carnot cycle typical in traditional combustion processes [144].

Solid oxide fuel cells (SOFCs) are characterized by their use of a solid ceramic material as the electrolyte that conducts oxygen ions from the cathode to the anode. They operate at high temperatures, typically between 600°C and 1000°C, which facilitates internal reforming of hydrocarbons and broadens the range of usable fuels, including hydrogen, natural gas, and biogas [145]. This high operating temperature provides SOFCs with several advantages, including high electrochemical efficiency and the ability to utilize heat released during electricity generation for cogeneration, potentially increasing the overall energy efficiency to 85-90% [146].

Despite their advantages, the deployment of SOFCs faces technological challenges primarily related to durability, cost, and operational issues at high temperatures. These challenges include thermal management, material degradation, and the complexity of maintaining stable operation over extended

periods. Research in this field has focused on enhancing the materials used in SOFCs to improve their longevity and reduce costs. Innovations such as the development of anode-supported designs have allowed for lower operating temperatures and thinner electrolytes, which significantly mitigate these challenges [147].

SOFCs can be configured in various forms, including tubular and planar designs, each offering distinct benefits in terms of scalability, manufacturing, and integration into existing energy systems. The choice of configuration affects the cell's performance, with planar SOFCs generally providing higher power densities than tubular versions due to their larger electrode/electrolyte interface areas [148].

Recent developments have also introduced advanced concepts like electrolyte-free SOFCs and single-chamber SOFCs, which represent innovative approaches to simplify SOFC technology and reduce its cost. Electrolyte-free designs, for example, eliminate the need for a dense ionic conductor by using mixed ionic-electronic conductors, which can simplify manufacturing processes and enhance operational flexibility [149].

Integrating SOFCs into the broader energy system presents challenges, particularly concerning the infrastructure required for fuel supply and the integration with other renewable energy sources. The ability of SOFCs to provide stable, dispatchable power makes them an excellent complement to intermittent renewable sources like wind and solar power [150].

Various types of SOFCs are presented in Figure 2.7 and described in more detail by Kuterbekov et al. [150].

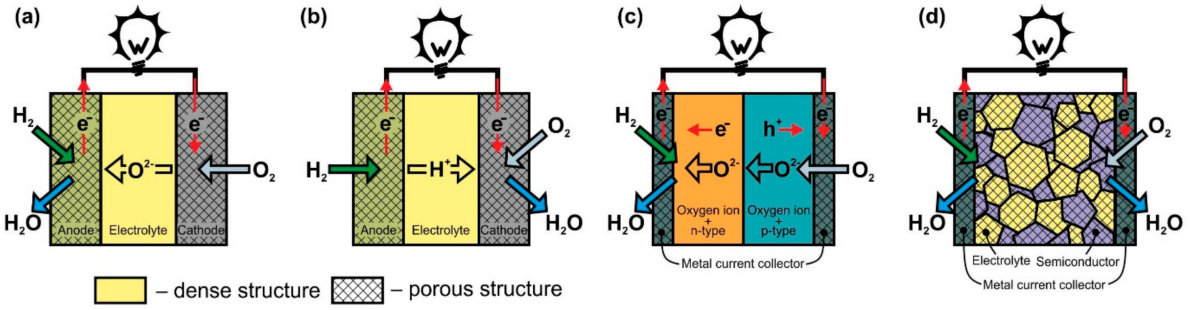

Figure 2.7: Scheme of operation of (a) oxygen-ion conducting electrolyte SOFC (O-SOFC), (b) proton-conducting electrolyte SOFC (H-SOFC), (c) double-layer fuel cells (DLFC), and (d) single-layer fuel cells (SLFC) [150].

Looking forward, the SOFC technology landscape is poised for significant advancements with ongoing research focused on lowering the operating temperatures to reduce stress on materials and enhance system longevity. The development of novel materials and innovative cell designs continues to be at the forefront of research, aiming to make SOFCs a more viable option for a wide range of applications, from residential to industrial scales [150].

2.5.2. Solid oxide electrolysis cells

Solid oxide electrolysis cells (SOEC) are increasingly recognized as a viable technology for the large-scale production of renewable hydrogen. This method has been widely analyzed and endorsed by various scholars [151]–[153]. In comparison to other technologies such as proton exchange membrane electrolysis cells (PEMEC) and alkaline electrolysis cells (AEC), SOECs stand out due to their superior efficiency. These benefits arise from their operation at higher temperatures and lower voltages [154]. The energy required for water and carbon dioxide electrolysis in SOECs is about 3.1 kWh/Nm³ for hydrogen and 3.4 kWh/Nm³ for carbon monoxide [155]. Operating within a temperature range of 750°C to 850°C, SOECs can achieve electrical efficiencies up to 95%, which exceeds those of lower-temperature electrolysis processes by 25% to 30% due to the enhanced ionic conductivity of the solid materials used and lower electrode polarization [156], [157].

Moreover, SOECs have the unique ability to directly generate syngas (a mixture of hydrogen and carbon monoxide), which is used in large-scale synthesis of chemicals like ethylene and ethanol. This syngas can also be converted into various hydrocarbon-based fuels through processes such as the

Fischer-Tropsch synthesis [158]. Additionally, SOECs produce a significant amount of waste heat during operation, which can be harnessed to enhance the overall energy efficiency of the system.

In Figure 2.8 both proton-conducting and oxide ion-conducting solid oxide electrolysis cells are demonstrated for producing hydrogen and syngas respectively.

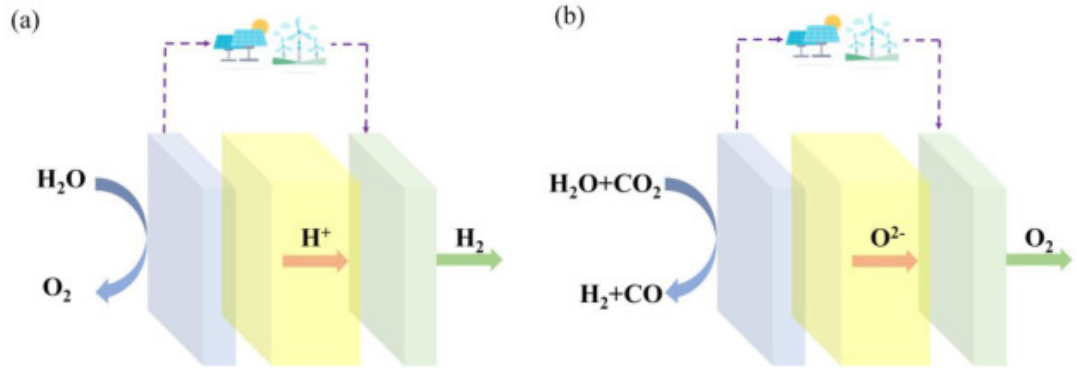

Figure 2.8: Schematic of proton-conducting and oxide ion-conducting solid oxide electrolysis cells [157].

Despite these promising attributes, the widespread adoption of SOEC technology faces obstacles such as high production and maintenance costs [159]. Currently, the cost to produce hydrogen using SOECs ranges from $2.99 to $7.02 per kilogram, which is higher than the costs associated with PEMEC and AEC technologies [160], [161]. Moreover, the components of SOEC systems are prone to oxidation and corrosion during prolonged exposure to high temperatures, presenting challenges in maintaining the integrity of the seals within the stack. These seals must resist both oxidative and reductive reactions across different regions of the cell. Managing thermal stress and maintaining even heat distribution within the cell are also critical for long-term operation.

Solid oxide electrolysis cells (SOEC) are categorized based on the type of ions they transport—either oxygen ions in oxygen ion-conducting SOECs (O-SOEC) or protons in proton-conducting SOECs (H-SOEC). These variations affect the cell's architecture and operational efficiency. O-SOECs, favored for high-temperature operations, facilitate efficient co-electrolysis of water and carbon dioxide, enabling the production of syngas—a mix of hydrogen and carbon monoxide. Conversely, H-SOECs, operating at lower temperatures, produce high-purity hydrogen without dilution by water vapor, which is especially beneficial for applications requiring pure hydrogen [157], [162]–[167].

Despite their high efficiency, SOECs face significant challenges concerning material durability and operational stability. The high operating temperatures lead to faster degradation of the components, particularly affecting the electrolyte and electrodes. The durability of these components is critical as they are susceptible to thermal stress, corrosion, and material deformation over time. Key issues include the sealing of interfaces to prevent leaks and maintaining material integrity under cyclic temperature variations and prolonged exposure to harsh conditions [157], [159]–[161].

Research continues to evolve around developing materials that can withstand the rigorous conditions of SOEC operation. Efforts are concentrated on enhancing the thermal stability and ionic conductivity of the materials used, thereby improving the overall efficiency and lifespan of the cells. For instance, advancements in ceramic technology and the development of composites have shown potential in reducing the degradation rate of SOEC components [157], [162].

Ongoing and future research aims to address the operational challenges and material limitations currently hindering the widespread adoption of SOEC technology. This includes improving the dynamic response of the cells to changes in operational conditions, such as fluctuations in input power from renewable sources, and optimizing the material compositions to enhance performance and durability. Research is particularly focused on the integration of SOECs with renewable energy systems to ensure stable and efficient performance under varying energy supply conditions [157], [163]–[165].

2.5.3. Reversible Solid Oxide Cell (RSOC): A Hybrid Approach in Energy Systems

The Reversible Solid Oxide Cell (RSOC) integrates the technologies of both Solid Oxide Fuel Cells (SOFC) and Solid Oxide Electrolysis Cells (SOEC) into a single versatile system capable of both power generation and electrolysis [157], [168], [169]. This dual-functionality allows RSOCs to alternate between producing hydrogen via electrolysis and generating electricity from hydrogen or other fuels, conducting these bidirectional processes simultaneously. Such flexibility makes the RSOC particularly valuable for diverse applications ranging from distributed power generation and energy storage to isolated operations.

While RSOCs are promising for their flexibility and efficiency, they are still in the developmental stages with numerous technical challenges yet to be overcome. Recent studies have focused on enhancing aspects such as the RSOC's output performance, durability, dynamic response, and control strategies, as well as its practical applications in various settings [157], [170]–[176].

Transitioning between modes—from fuel cell to electrolyzer and back—poses additional challenges, particularly regarding the thermal and mechanical stresses involved. Such shifts can dramatically affect system stability and efficiency, necessitating advanced thermal management strategies to mitigate these impacts [177], [178].

RSOCs also present significant potential for integration into broader energy systems, such as in polygeneration applications where they can dynamically switch between roles to balance energy demand and supply efficiently. For example, studies have applied RSOC technology in settings ranging from steel mills to paper mills, demonstrating substantial improvements in energy efficiency and cost-effectiveness compared to more traditional energy systems [157], [179], [180].

Despite the promising advancements, the high costs associated with RSOC development and operation pose significant barriers to widespread adoption. Efforts to streamline the manufacturing process and enhance the economic feasibility of RSOCs are ongoing, with research directed towards simplifying system design and scaling up production to lower costs and improve accessibility [157], [181], [182].

In summary, the RSOC exemplifies a significant innovation in fuel cell technology, offering a versatile and efficient solution for energy conversion and storage. However, it does not have very fast dynamics, which can be compensated by combining it with other energy storage solutions such as lithium-ion batteries, flywheels, or supercapacitors. This combination can provide rapid response capabilities and enhance overall system stability. As research progresses, the integration of RSOCs with these technologies holds promise for managing renewable resources more dynamically and improving grid stability for long-term operation.

2.6. Battery, Flywheel, and Supercapacitor for Integration with RSOC

Integrating Reversible Solid Oxide Fuel Cells (RSOCs) with other high power energy storage devices can significantly enhance the performance and reliability of microgrids. This section explores the potential of different types of batteries, flywheels, and supercapacitors to complement RSOCs, focusing on their compatibility and combined benefits in energy systems.

2.6.1. Lithium-Ion Batteries

Lithium-ion batteries (Li-ion BES) are widely known for their high energy density, power density, and efficiency. These attributes make them particularly effective for applications requiring frequent cycling and fast response, such as load balancing and peak shaving in microgrids. The specific energy and power densities of lithium-ion batteries allow them to store a significant amount of energy and deliver it quickly, which is essential for maintaining grid stability and reliability.

When combined with RSOCs, lithium-ion batteries can provide the necessary rapid response to fluctuating energy demands, compensating for the slower dynamic response of RSOCs. This synergy ensures a stable and reliable energy supply, optimizing overall system efficiency and performance. Additionally, lithium-ion batteries are relatively cost-effective compared to other high power energy storage solutions and can store energy for several hours, which allows for a smaller and more cost-optimized RSOC size [183].

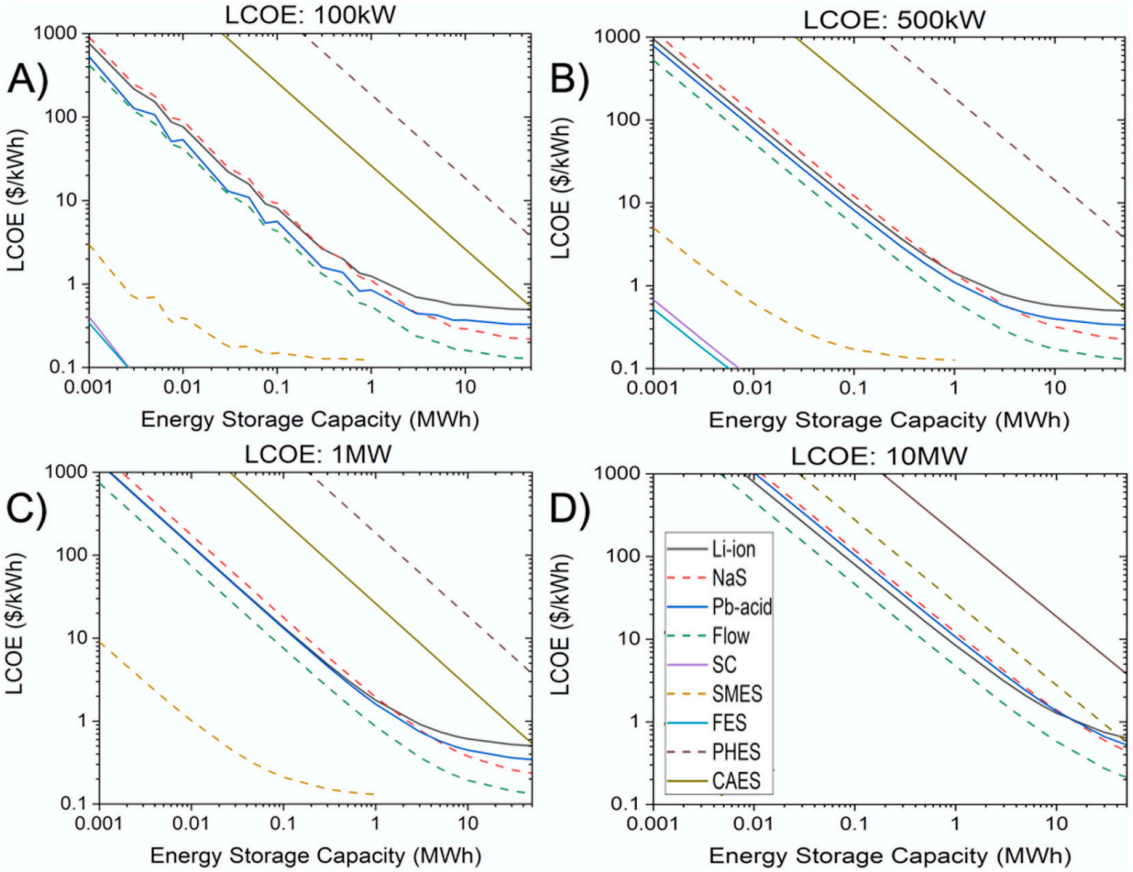

Figure 2.9: Levelized Cost of Energy (LCOE) of various energy storage devices as functions of power and energy storage capacity [183].

Lithium-ion batteries also exhibit high cycle efficiency and long cycle life, making them suitable for frequent charge-discharge cycles. Figure 2.9 illustrates the Levelized Cost of Energy (LCOE) for various energy storage devices as a function of power and energy storage capacity. It is evident that lithium-ion batteries offer a competitive cost profile across different power and storage capacities, making them a versatile choice for a wide range of applications.

2.6.2. Other Types of Batteries

Apart from lithium-ion batteries, other types of batteries such as nickel-cadmium, lead-acid, sodium-sulfur (NaS), and flow batteries are also used in energy storage systems. Lead-acid batteries are cost-effective and widely used but have lower energy density and shorter cycle life in comparison to lithium-ion batteries. Nickel-cadmium batteries offer good performance over a wide range of temperatures but suffer from higher costs and environmental concerns due to cadmium toxicity. NaS batteries provide high energy density and efficiency but require high operating temperatures, making them suitable for large-scale storage applications.

Flow batteries, such as vanadium redox flow batteries, provide scalability and long cycle life but are generally less efficient and more expensive. These battery types can complement RSOCs in specific scenarios, but their limitations often make lithium-ion batteries a more suitable choice for high power energy storage in microgrids [183].

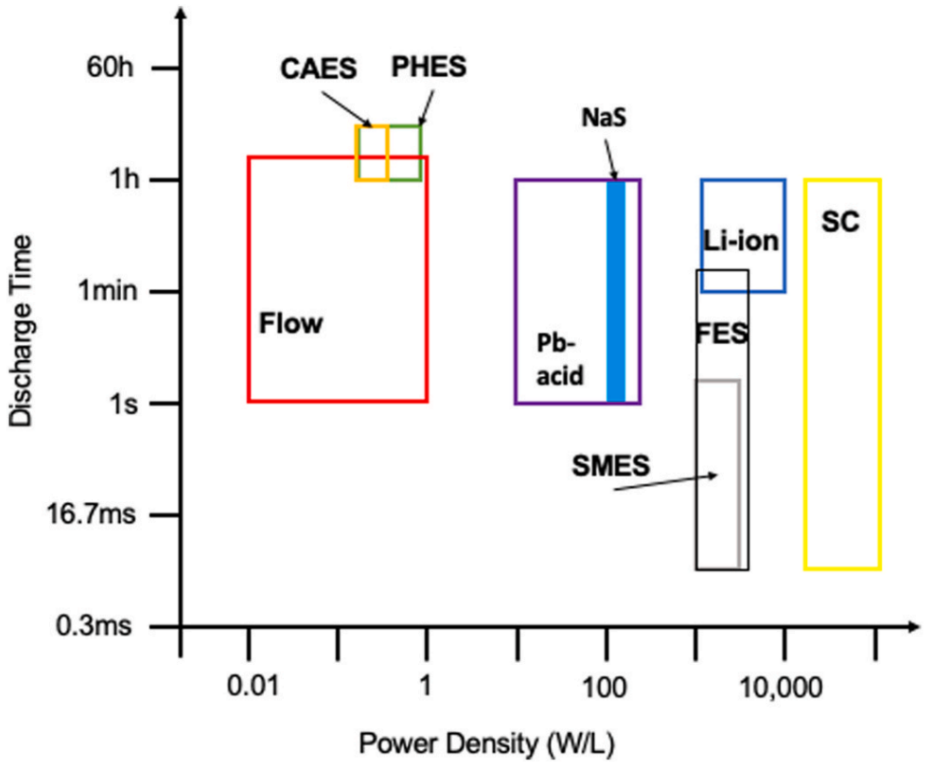

Figure 2.10: Discharge Time vs. Power Density of various energy storage devices [183].

Figure 2.10 illustrates the discharge time versus power density for various energy storage devices. It highlights the capabilities of different battery technologies in terms of power delivery and energy storage duration. For instance, NaS and lithium-ion batteries offer a good balance between discharge time and power density, making them suitable for applications requiring both high power and substantial energy storage.

2.6.3. Flywheels

Flywheel energy storage systems (FES) offer excellent cycle life and power density, making them suitable for applications requiring rapid energy discharge and high power output. Flywheels are highly efficient and have long operational lifetimes, although their energy density is lower compared to batteries. They operate by storing kinetic energy in a rotating mass and releasing it quickly when needed, providing a fast response to power demands.

In combination with RSOCs, flywheels can handle high power demands and provide instantaneous energy, thus mitigating the thermal and mechanical stresses associated with the transition modes of RSOCs. However, flywheels are typically more expensive than lithium-ion batteries and are less capable of mid-term energy storage. Figure 2.11 shows the efficiency versus power density of various energy storage devices, indicating the high efficiency of flywheels [183].

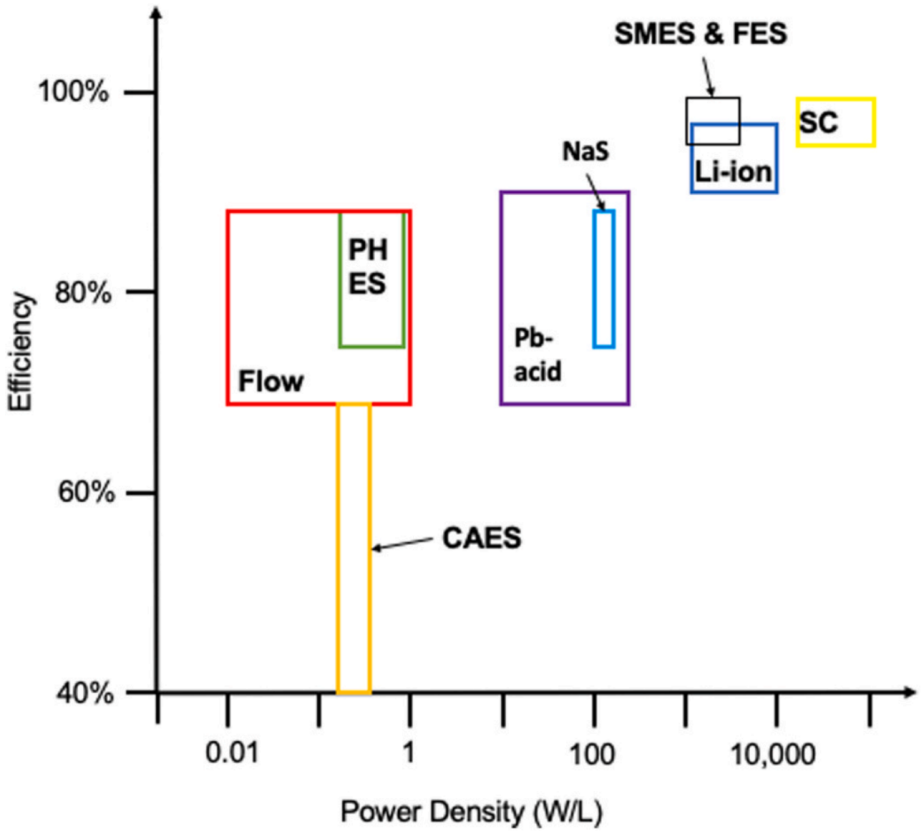

Figure 2.11: Efficiency vs. Power Density of various energy storage devices [183].

Flywheels are particularly effective in applications that require frequent cycling and rapid response, such as stabilizing voltage fluctuations and providing short-term power support. However, their high costs and lower energy density compared to batteries make them less suitable for applications requiring long-term energy storage. The efficiency of flywheels, as seen in Figure 2.11, is among the highest, but this comes at the expense of higher capital costs and limited energy capacity.

2.6.4. Supercapacitors

Supercapacitors (SC) are characterized by their high power density, efficiency, and fast response times. They are ideal for applications needing quick energy bursts, such as power quality management and grid stability enhancement. Supercapacitors store energy electrostatically and can discharge it very quickly, making them suitable for applications that require rapid power delivery.

When integrated with RSOCs, supercapacitors can provide rapid energy delivery during peak loads and enhance the overall power quality of the microgrid. This combination leverages the high energy density of RSOCs with the fast dynamic response of supercapacitors. However, their high cost and limited energy storage capacity make them less suitable for applications requiring mid- and long-term energy storage [183].

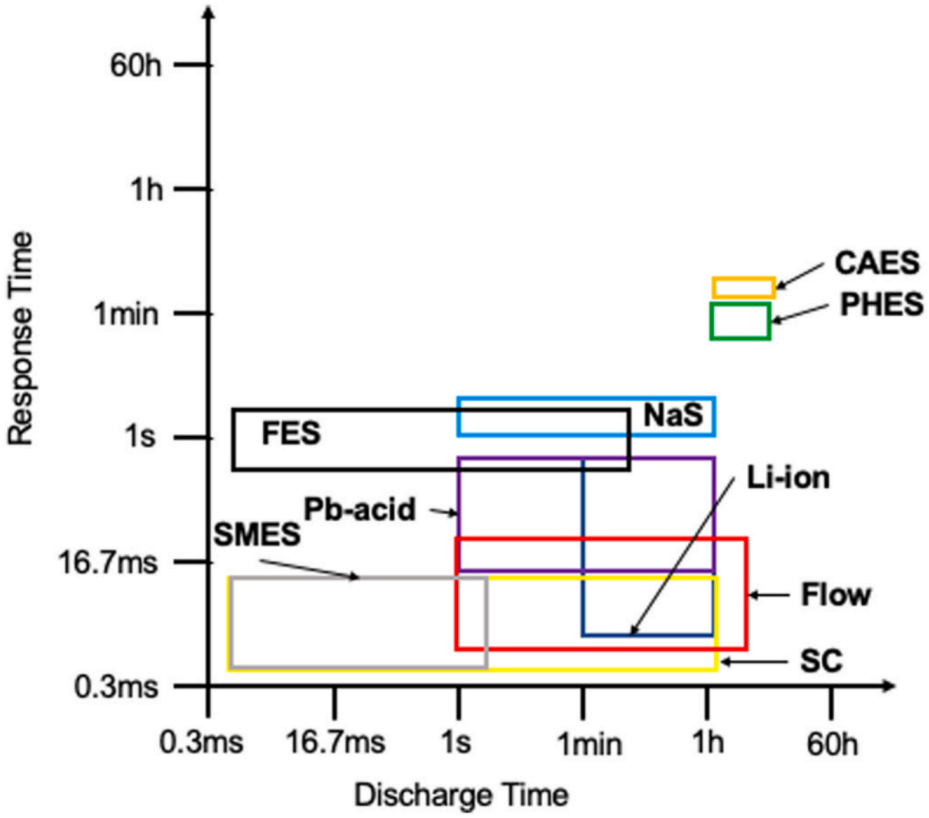

Figure 2.12: Response Time vs. Discharge Time of various energy storage devices [183].

Figure 2.12 shows the response time versus discharge time for various energy storage devices, highlighting the rapid response capabilities of supercapacitors. Supercapacitors provide excellent performance in terms of quick energy discharge and fast response, but their limited energy storage capacity and high costs make them less ideal for sustained energy delivery.

2.6.5. Comparison

In comparing the different energy storage technologies, lithium-ion batteries, flywheels, and supercapacitors each have distinct advantages and limitations. Lithium-ion batteries offer a balanced combination of high energy density, fast response times, and cost-effectiveness, making them ideal for microgrid applications that require both short-, mid- and long-term energy storage. Those are particularly effective when combined with RSOCs, as they can handle power spikes and provide energy storage for several hours, which allows for a smaller and more cost-optimized RSOC configuration.

Flywheels and supercapacitors, while offering high power density and quick response, are generally more expensive and less suitable for mid-term energy storage. Flywheels are effective for applications requiring rapid energy discharge and high power output, but their high costs and lower energy density compared to batteries limit their use. Supercapacitors provide rapid energy delivery and enhance power quality but have high costs and very limited energy storage capacity.

Figures 2.9 through 2.11 collectively illustrate these points by comparing various energy storage devices across metrics such as cost, efficiency, power density, and discharge time. The combination of RSOCs and lithium-ion batteries provides a reliable, efficient, and economically viable solution for modern microgrid systems. This integration should ensure a stable and responsive energy supply, optimizing overall system performance and reducing costs [183].

2.7. Microgrid configuration decisions

Based on the reviewed material, several key decisions have been made for the design of the microgrid. It was decided to build the microgrid as a DC system rather than an AC system. This choice is driven by the higher efficiency and reduced energy losses associated with DC microgrids, particularly in applications with high DC load demands and renewable energy integration. DC microgrids also eliminate issues related to frequency synchronization and reactive power, making them more suitable for future energy systems dominated by DC loads and renewable energy sources.

For energy storage, a combination of Reversible Solid Oxide Fuel Cells (RSOCs) and lithium-ion batteries will be used. This hybrid approach leverages the high energy density and long-term storage capabilities of RSOCs with the rapid response and high power density of lithium-ion batteries. This combination ensures a stable and reliable energy supply, optimizes overall system efficiency, and reduces costs by allowing a smaller and more cost-effective RSOC configuration.

As for the control strategy, a classical rule-based hierarchical control has been chosen. This approach provides a structured and straightforward method for managing the microgrid's operations, ensuring system stability and efficiency. Rule-based control techniques are favored for their simplicity, low computational requirements, and ease of implementation. The hierarchical control strategy will enable effective coordination between different energy sources and storage devices, ensuring optimal performance under varying conditions.

2.8. Summary

In conclusion, this chapter has thoroughly examined the literature on microgrids and modern energy systems, providing a solid foundation for understanding their advantages and challenges. Microgrids are increasingly recognized for their ability to enhance energy efficiency, resilience, and sustainability, especially when integrated with renewable energy sources. The review highlights the critical role of various energy storage systems, including lithium-ion batteries, flywheels, and supercapacitors, in maintaining the stability and efficiency of microgrids. Informed by this extensive review, decisions were made regarding the configuration of the microgrid to ensure it is efficient, reliable, and capable of meeting the energy demands of modern applications. The chosen DC configuration, energy storage combination, and control strategy are designed to contribute to a robust and future-proof microgrid design, which will be designed, tested, and validated in the following chapters.

3

Simulation of Electrical Load Profile for Kaya Imani Resort

This chapter presents a detailed simulation of the electrical load profile for Kaya Imani Resort in Msambweni, Kenya. It delves into the energy requirements of the resort by examining the operational characteristics and power needs of various electrical appliances and systems. The resort consists of multiple facilities including a private house, staff quarters, Rafiki house, Tumaini house, a kitchen and storage complex, a reception area, dance hall, workshop, and spaces designated for potential future cottages. Recently, the resort's management decided to transition fully or partially to renewable energy sources, prompting the need to estimate the required number of solar panels, batteries, and the associated capital investment. The initial step involved creating a representative load profile for the resort. It was assumed that high peak power devices would remain connected to the distribution grid, while devices with a more constant power demand would be powered by renewable sources. Consequently, three load profiles were simulated: one for the entire resort, one for the components connected to the distribution grid, and one for those linked to renewable energy. Subsequent sections of this thesis will explore the feasibility of a microgrid that powers the entire resort exclusively with renewable energy. The simulation is performed using an open-source Python library RAMP.

Figure 3.1: Aerial view of Kaya Imani Resort.

Figure 3.2: Satellite view of Kaya Imani Resort.

3.1. RAMP

RAMP, or the RAMP project, is a versatile, open-source software in a form of a Python library designed for stochastic simulation of energy demand time series, useful in generating synthetic multi-energy load profiles, particularly in areas with limited data [184]. It is applicable across various operating systems and can be installed via pip, conda, or from the source. The software supports building energy demand models using different types of input files, including Python scripts and spreadsheets, and allows users to simulate diverse scenarios with adjustable command line options.

RAMP allows for intricate modeling of different user types such as households, schools, and more, each with their specific appliances. Users can specify numerous parameters for each appliance, including power consumption, usage windows, and duty cycles, which enhances the accuracy and relevance of the simulations.

RAMP is equipped to handle a wide range of simulation complexities. It can perform simple daily profiles to extensive year-long simulations with parameters that can be adjusted monthly. The software allows specifying whether appliances are used on weekdays, weekends, or continuously, providing flexibility to accommodate various user requirements and scenarios.

Users can contribute to its development by engaging with its community on GitHub. The software's licensing is under the EUPL, ensuring it remains freely available and maintainable by the community. For detailed simulation instructions and advanced features, the RAMP documentation provides comprehensive guides and examples.

3.2. Electrical Load Profile Simulation of Kaya Imani Resort

The simulation covers a broad spectrum of the resort's operational areas, including accommodations, communal spaces, and service areas. In the simulation, appliance counts, power ratings, operational windows, and usage patterns are taken into account. This simulation is crucial for understanding the load duration curve of the resort along with identifying average consumption and peak consumption

periods.

3.2.1. Private House

The table 3.1 summarizes the appliances configured for the load profile simulation within the Private House setting, including their operational characteristics and constraints.

Table 3.1: Private house appliances used in load profile simulation

Appliance	Number	Power (W)	Operational Window (hrs)	Functional Time (min)	Occasional Use
Indoor LED lights	40	10	18:00-22:00	240	N/A
Floor fans	2	45	00:00-08:00, 21:00-24:00	660	N/A
Floor fans for guests	4	45	00:00-08:00, 21:00-24:00	660	0.25
Computers	2	80	07:00-22:00	60	N/A
Computers for guests	4	80	07:00-22:00	60	0.25
Phone charging	2	5	24hrs	60	N/A
Phone charging for guests	4	5	24hrs	60	0.25
Filter coffee machine	1	1400	06:00-08:00	20	N/A
Washing machine	1	2100	06:00-17:00	60	0.5
Fridge (big)	2	85	24hrs	1440	N/A
Fridge (small)	1	50	24hrs	1440	0.2
Blender	1	400	07:00-19:00	5	N/A
Toaster	1	400	07:00-08:00	5	N/A
Kitchen oven	1	1100	06:00-20:00	130	N/A
Vacuum cleaner	1	1200	08:00-18:00	20	0.29
Dehumidifier	1	400	08:00-20:00	360	N/A
Instant water heater	1	5500	07:00-22:00	5	N/A

Column Descriptions

- **Appliance**: The name of the appliance, used to identify the type (e.g., ”Indoor LED lights”, ”Washing machine”).
- **Number**: The number of units of each appliance present in the simulation. Default is 1 if not specified.
- **Power (W)**: The average power consumption of the appliance in watts. If the appliance has variable daily power, a series can be represented.
- **Operational Window (hrs)**: The hours during which the appliance can potentially operate, formatted as start time-end time. For appliances with multiple windows, the times are separated by commas.
- **Functional Time (min)**: The total time in minutes the appliance is on during the day. This time is independent of the operational windows.
- **Occasional Use**: Defines how often the appliance is used, represented as a percentage. For example, 0.5 indicates the appliance is used every second day. N/A in this case means that the appliance is used every day.

3.2.2. Staff Quarters

The table 3.2 summarizes the appliances configured for the load profile simulation within the Staff Quarters, including their operational characteristics and constraints.

Table 3.2: Staff quarter appliances used in load profile simulation

Appliance	Number	Power (W)	Operational Window (hrs)	Functional Time (min)	Occasional Use
Indoor LED lights	10	10	18:00-22:00	240	N/A
Floor fans	2	45	21:00-06:00	540	N/A
Phone charging	6	5	24hrs	180	N/A
Fridge	1	85	24hrs	1440	N/A
Iron	1	1000	10:00-18:00	60	N/A
Washing machine	1	2100	24hrs	60	0.25

3.2.3. Rafiki House

The table 3.3 summarizes the appliances configured for the load profile simulation within the Rafiki House, including their operational characteristics and constraints.

Table 3.3: Rafiki house appliances used in load profile simulation

Appliance	Number	Power (W)	Operational Window (hrs)	Functional Time (min)	Occasional Use
Indoor LED lights	$22 \times$ ROL	10	18:00-22:00	240	N/A
Floor fans	$3 \times$ ROL	45	21:00-09:00, 13:00-16:00	900	N/A
Computers	$4 \times$ ROL	80	07:00-22:00	120	N/A
Phone charging	$6 \times$ ROL	5	24hrs	60	N/A
Heating element	1	1500	07:00-22:00	$4.65 \times 4 \times$ ROL	0.3

Note: ROL (Resort Occupancy Level) varies between 0 and 1.

3.2.4. Kitchen and Storage

The table 3.4 summarizes the appliances configured for the load profile simulation within the Kitchen and Storage, including their operational characteristics and constraints.

Table 3.4: Kitchen and storage appliances used in load profile simulation

Appliance	Number	Power (W)	Operational Window (hrs)	Functional Time (min)	Occasional Use
Indoor LED lights	10	12	18:00-22:00	240 $\times$ ROL	N/A
Kettle	1	1500	06:00-19:00	2+13$\times$ROL	N/A
Bread machine	1	1000	13:00-15:00	$40 \times$ ROL	N/A
Toaster	1	400	07:00-09:00	$40 \times$ ROL	N/A
Soup blender	1	800	10:00-19:00	$20 \times$ ROL	N/A
Blender	1	400	07:00-09:00	$30 \times$ ROL	N/A
Fridge small	1	50	24hrs	1440	N/A
Fridge medium	1	85	24hrs	1440	N/A
Fridge big	1	150	24hrs	1440	N/A
Freezer	1	180	24hrs	1440	N/A
Music speaker	1	40	16:00-21:00	300 $\times$ ROL	N/A
Filter coffee machine	1	1400	07:00-09:00	30$\times$ROL	N/A
Wall fans	2	60	13:00-16:00	180	0.3

Note: ROL (Resort Occupancy Level) varies between 0 and 1. For appliances with a variable functional time, it is calculated as the product of the specified time and ROL. The ”Occasional Use” column indicates the probability of use, where applicable, such as with the Wall fans, which are used only on hot days, assumed at a 30% probability.

Reception

The table 3.5 summarizes the appliances configured for the load profile simulation within the Reception, including their operational characteristics and constraints.

Table 3.5: Reception appliances used in load profile simulation

Appliance	Number	Power (W)	Operational Window (hrs)	Functional Time (min)
Indoor LED lights	10	5	18:00-21:00	180
Phone charging	3	5	08:00-20:00	150
Computer	1	80	09:00-21:00	60
Printer	1	250	09:00-21:00	$10 \times$ ROL

Note: ROL (Resort Occupancy Level) varies between 0 and 1. For the Printer, the functional time is calculated as $10 \times$ ROL minutes, adjusting dynamically with the occupancy level.

3.2.5. Tumaini House

The table 3.6 summarizes the appliances configured for the load profile simulation within Tumaini House, including their operational characteristics and constraints.

Table 3.6: Tumaini house appliances used in load profile simulation

Appliance	Number	Power (W)	Operational Window (hrs)	Functional Time (min)	Occasional Use
Indoor LED lights	$30 \times$ ROL	10	18:00-22:00	240	N/A
Floor fans	$3 \times$ ROL	45	21:00-09:00, 13:00-16:00	900	N/A
Computers	$3 \times$ ROL	80	07:00-22:00	120	N/A
Phone charging	$6 \times$ ROL	5	24hrs	60	N/A
Heating element	1	1500	07:00-22:00	$4.65 \times 6 \times$ ROL	0.3

Note: ROL (Resort Occupancy Level) varies between 0 and 1.

3.2.6. Security Lights

The table 3.7 summarizes the security light configurations for the load profile simulation across different areas, including their operational characteristics and constraints.

Table 3.7: Security lights used in load profile simulation

Location	Number	Power (W)	Operational Window (hrs)	Functional Time (min)
Private House Security Lights	5	10	19:00-06:00	660
Staff House Security Lights	5	10	19:00-06:00	660
Entrance/Parking Security Lights	10	10	19:00-06:00	660
Stairs Security Lights	6	10	19:00-06:00	660
Lower Area Between Stairs and Ocean	15	10	19:00-06:00	660
Ferry Lights in Mango Tree	20	10	19:00-06:00	660
Open Space Security Lights	6	10	19:00-06:00	660

3.2.7. Dance Hall

The table 3.8 summarizes the appliances configured for the load profile simulation within the Dance Hall, including their operational characteristics and constraints.

Table 3.8: Dance hall appliances used in load profile simulation

Appliance	Number	Power (W)	Operational Window (hrs)	Functional Time (min)	Occasional Use
Indoor LED lights	$10 \times$ ROL	10	18:00-22:00	240	N/A
Floor fans	$6 \times$ ROL	45	13:00-16:00	180	0.3
Phone charging	$6 \times$ ROL	5	24hrs	60	N/A

Note: ROL (Resort Occupancy Level) varies between 0 and 1.

3.2.8. Workshop

The table 3.9 summarizes the appliances configured for the load profile simulation within the Workshop, including their operational characteristics and constraints.

Table 3.9: Workshop appliances used in load profile simulation

Appliance	Number	Power (W)	Operational Window (hrs)	Functional Time (min)	Occasional Use
Drill	1	600	10:00-18:00	60	0.25
Sanding Machine	1	1200	10:00-18:00	60	0.25
Circular Saw	2	1400	10:00-18:00	60	0.25

3.2.9. Other Category

The table 3.10 summarizes the appliances configured for the load profile simulation within the ”Other” category, including their operational characteristics and constraints.

Table 3.10: Other category appliances used in load profile simulation

Appliance	Number	Power (W)	Operational Window (hrs)	Functional Time (min)	Occasional Use
Pool Pump	1	1225	06:00-08:00	120	N/A
Water Pump	1	750	24hrs	60	N/A
Projector	1	85	19:00-23:00	240	Once a week

3.2.10. Future Cottages

The table 3.11 summarizes the appliances configured for the load profile simulation within Future Cottages, including their operational characteristics and constraints, directly incorporating formulas related to the resort occupancy level (ROL).

Table 3.11: Future cottages appliances used in load profile simulation

Appliance	Number	Power (W)	Operational Window (hrs)	Functional Time (min)	Occasional Use
Indoor LED lights	$30 \times$ ROL	10	18:00-22:00	240	N/A
Floor fans	$3 \times$ ROL	45	21:00-09:00, 13:00-16:00	900	N/A
Computers	$4 \times$ ROL	80	07:00-22:00	120	N/A
Phone charging	$6 \times$ ROL	5	24hrs	60	N/A

Heating element	1	1500	07:00-22:00	4.65×4×ROL	0.3

Note: ROL (Resort Occupancy Level) varies between 0 and 1.

3.2.11. Heating element energy consumption estimation

The heating element for water heating is going to be simulated as an electrical load, and it is hence necessary to understand how to simulate it accurately. Therefore, the following approach was taken to determine the energy required, calculate the operational time, and define the appliance characteristics for the simulation.

Energy Required to Heat Water for One Shower

To determine the energy required to heat water for one person's shower from 30 degrees Celsius to 40 degrees Celsius, the following data and formula were used:

- Initial water temperature: $30°\mathrm{C}$
- Final water temperature: $40°\mathrm{C}$
- Mass of water used in one shower: 10 liters ($10,000$ grams)
- Specific heat capacity of water: $4.186\,\mathrm{J/g°C}$

The formula for calculating the energy required (Q) is:

$$Q = m \cdot c \cdot \Delta T \tag{3.1}$$

where:

- Q is the heat energy in joules,
- m is the mass of water in grams, $m = 10000$ grams,
- c is the specific heat capacity of water in $\mathrm{J/g°C}$, $c = 4.186\,\mathrm{J/g°C}$,
- ΔT is the change in temperature in degrees Celsius, $\Delta T = 10\,°\mathrm{C}$.

The calculation was as follows:

$$Q = m \cdot c \cdot \Delta T = 10000 \cdot 4.186 \cdot 10 \; = 418600\,\text{joules} = 0.116\,\text{kWh}$$

Operational Time for the Heating Element

Given the energy required and the power rating of the heating element, the operational time was calculated.

- Adjusted Power Rating: $1500\mathrm{W}$ ($1.5\,\mathrm{kW}$)
- Energy Required: Approximately $0.116\,\mathrm{kWh}$

The operational time in minutes was calculated as follows:

$$\text{Functional time (minutes)} = \frac{\text{Energy Required (kWh)}}{\text{Power (kW)}} \times 60 = 4.65\,\mathrm{min} \tag{3.2}$$

Defining the Heating Element Appliance

With the operational time calculated, the heating element appliance was defined as follows:

```
Heating_element = a_House.Appliance(
    number=1,
    power=1500,  # Power in watts
    num_windows=1,
    func_time=4.65*n,  # Actual time the device is used during the day, in minutes,
                # n is the number of people in a house
    occasional_use=0.3, # Used only on cold days
```

```
)
Heating_element.windows(
    window_1=[420, 1320],  # Operational window: 07:00-22:00 in minutes from midnight
)
```

3.3. Load Duration Curves of One Year

All the following simulations were performed to simulate 364 days with 1 minute resolution. Hence, comprising 524,160 data points. The data is demonstrated in figures 3.3, 3.4, 3.5, and 3.6 in a form of load duration curves. It is possible to observe, that different resort occupancy levels are presented in the plots for qualitative comparison. However, for the sizing of the electrical system the resort is considered being full. For this reason, the following parameters in this chapter will be describing the full occupancy curve only.

3.3.1. Entire System

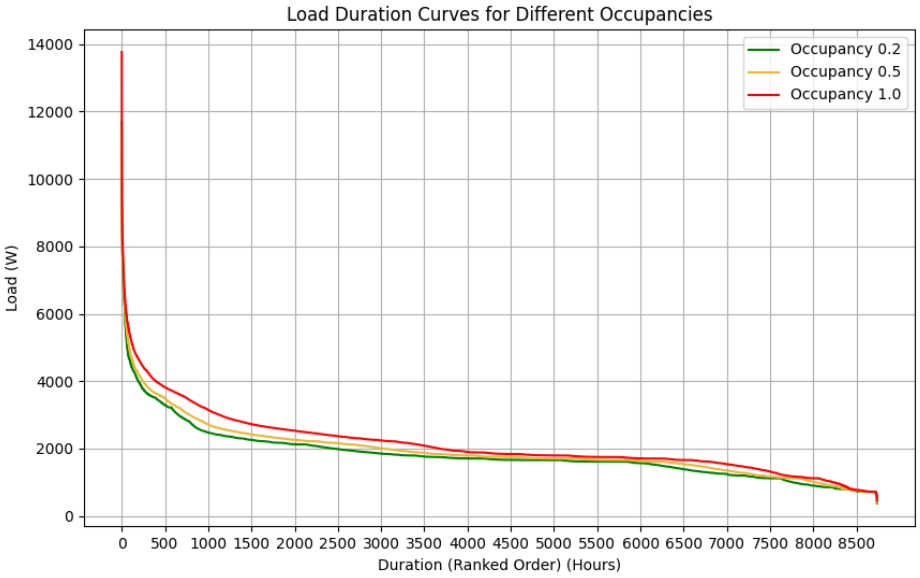

Figure 3.3: Load duration curves for different occupancy levels for the entire resort system.

The load duration curve for in figure 3.3 marked in red color has a mean power consumption of 2124.98 W. The standard deviation is 942.26 W, indicating variability around the mean. The minimum and maximum power consumptions recorded are 455.03 W and 13770.02 W, respectively, with quartiles at 1660.01 W (25%), 1845.01 W (50%), and 2468.01 W (75%).

$$\begin{aligned}\text{Annual Energy Consumption} &= 2124.978074\ \text{W} \times 8,736\ \text{hours}/1,000 \\ &= 18,563.81\ \text{kWh}\end{aligned}$$

$$\text{Daily Energy Consumption} = 2124.978074\ \text{W} \times 24\ \text{hours/day}/1,000 = 51.00\ \text{kWh/day}$$

3.3.2. Loads Connected to the Renewable Grid

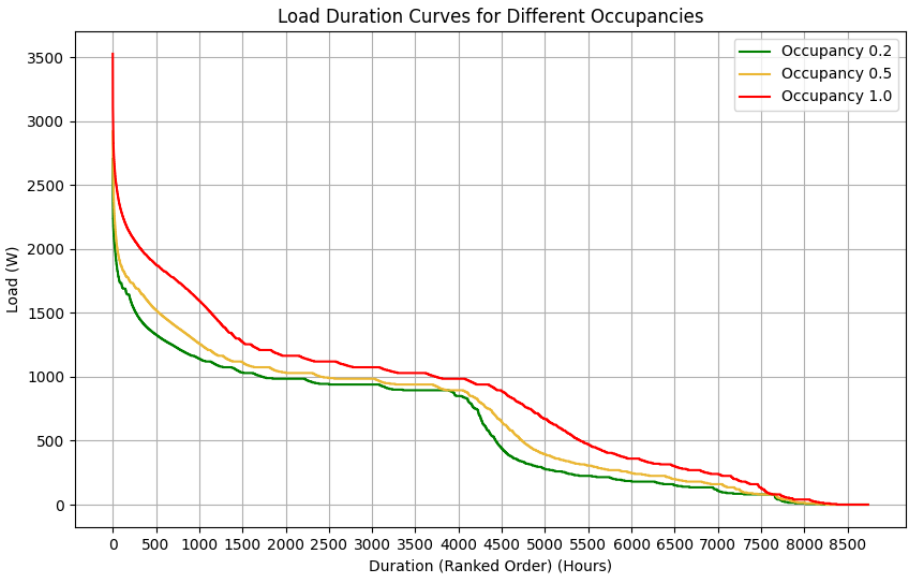

Figure 3.4: Load duration curves for different occupancy levels for the renewable part of the system.

The load duration curve in figure 3.4, marked in red color has the mean power consumption of 821.85 W, with a standard deviation of 594.12 W. Power consumption varies from a minimum of 0.014 W to a maximum of 3528.01 W. Quartile values are located at 290.01 W (25%), 930.01 W (50%), and 1155.01 W (75%).

$$\begin{aligned}\text{Annual Energy Consumption} &= 821.852202 \text{ W} \times 8,736 \text{ hours}/1,000 \\ &= 7,179.70 \text{ kWh}\end{aligned}$$

$$\text{Daily Energy Consumption} = 821.852202 \text{ W} \times 24 \text{ hours/day}/1,000 = 19.72 \text{ kWh/day}$$

3.3.3. Loads Connected to the Kenyan Grid

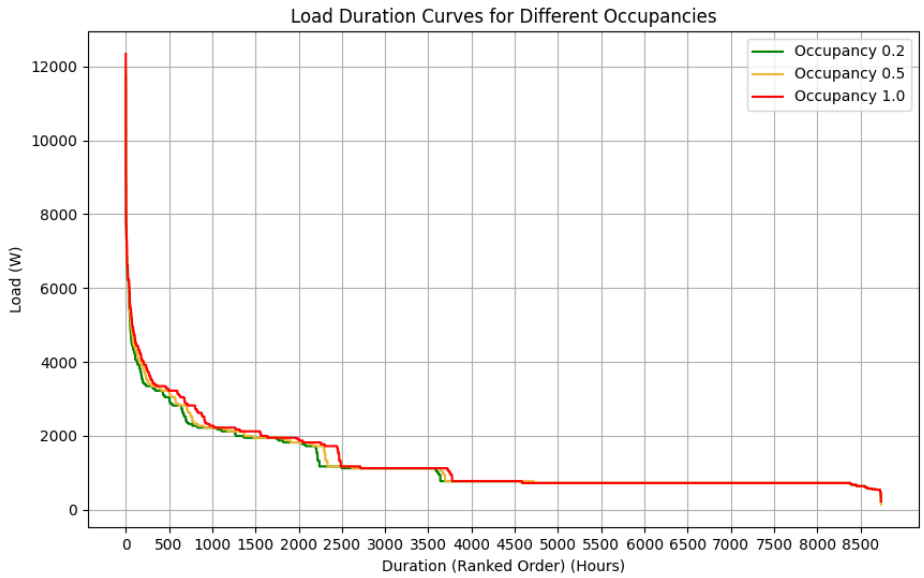

Figure 3.5: Load duration curves for different occupancy levels for loads connected to the Kenyan grid.

The load duration curve in figure 3.5, marked in red color has an average power consumption of 1307.54 W. The standard deviation here is 969.79 W. The recorded power consumption ranges from 220.00 W to 12345.01 W, with quartile marks at 720.00 W (25%), 770.00 W (50%), and 1820.01 W (75%).

$$\begin{aligned}\text{Annual Energy Consumption} &= 1307.538630 \text{ W} \times 8,736 \text{ hours}/1,000 \\ &= 11,422.66 \text{ kWh}\end{aligned}$$

$$\text{Daily Energy Consumption} = 1307.538630 \text{ W} \times 24 \text{ hours/day}/1,000 = 31.38 \text{ kWh/day}$$

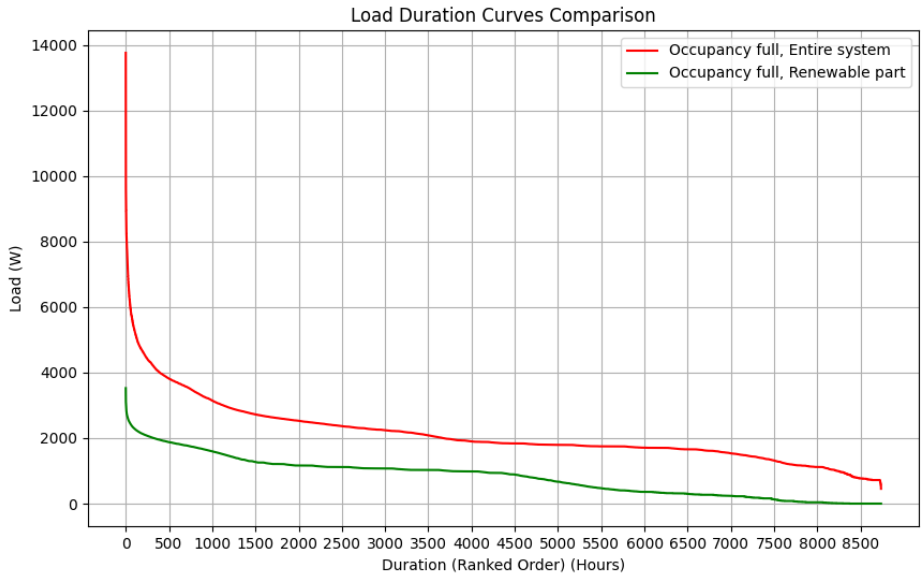

Figure 3.6: Comparison of load duration curves for full occupancy between the loads in the entire system and the connected to renewable sources.

From Figure 3.6 it is evident that the loads, which are planned to be connected to the renewable sources, exhibit significantly more stable and consistent power profiles. Unlike loads connected to the grid, these do not experience large power fluctuations, ensuring a smoother and more predictable energy consumption pattern. Hence, smaller requirements for energy storage.

3.4. Load Profiles of One Week

Understanding the load profiles and their implications for grid management and energy storage requirements is essential for effective energy planning. The series of figures depicting simulated load profiles informs us about the anticipated behavior of various loads when connected to different power sources.

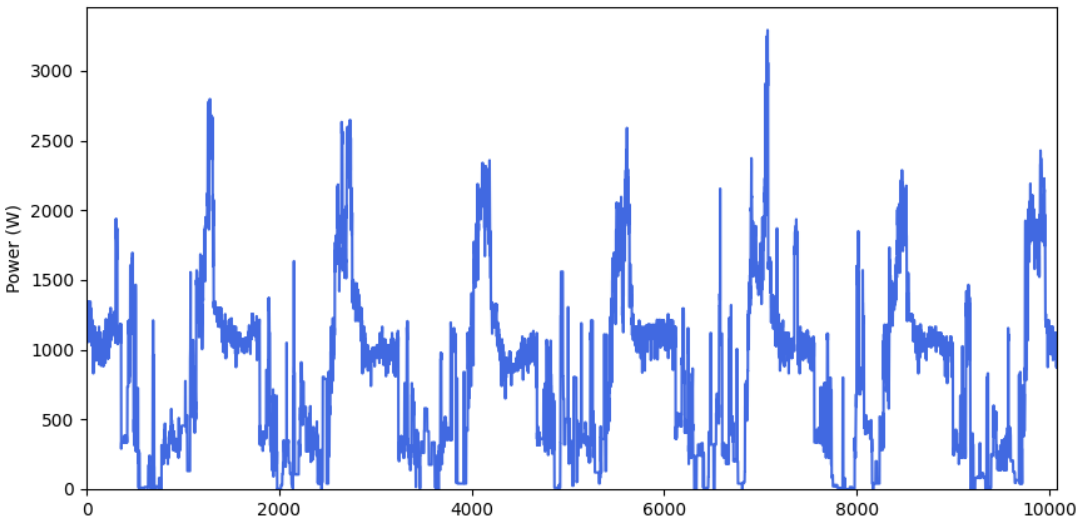

Figure 3.7: Power consumption pattern for the loads connected to the renewable grid during one week.

Figure 3.7 displays the simulated load profile for the selected loads that are planned to be connected to the renewable energy grid. The displayed profile is smoother than in Figure 3.9, with modest fluctuations, which indicates that the loads chosen for renewable energy connection are those with more predictable and even consumption patterns. This selection is strategic, as it aligns with the inherently variable nature of renewable generation; by connecting loads with stable demands, the system may require smaller battery storage capacities and can better accommodate the intermittency of renewables.

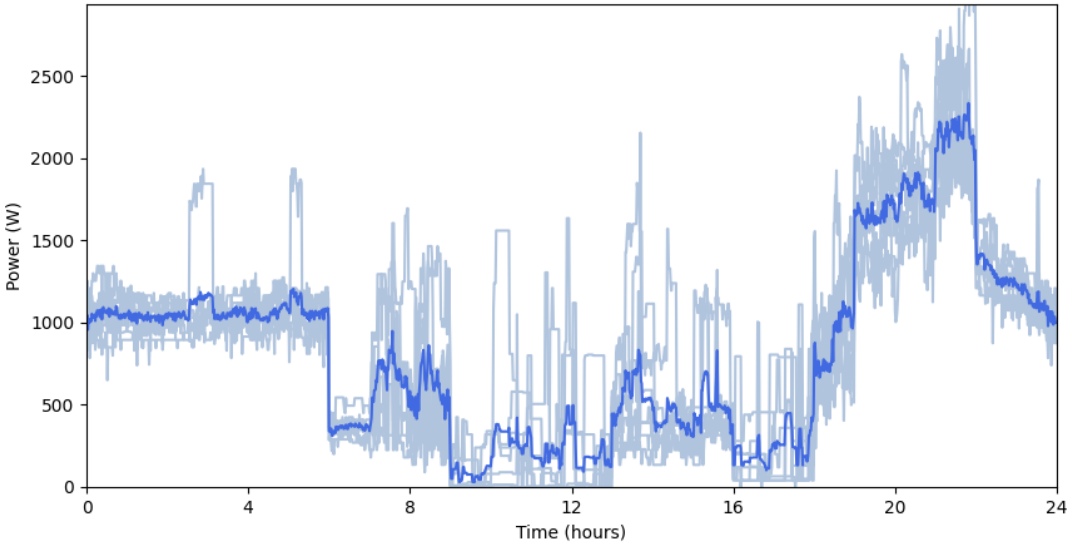

Figure 3.8: Average daily power consumption pattern for the loads connected to the renewable grid over the course of one week, with the dark blue curve being the average and the pale blue curves denoting individual days.

Figure 3.8 shows the average daily power consumption pattern for these selected renewable-connected loads, with the average represented by the dark blue line against the backdrop of daily variations in pale blue. The closer clustering of the daily profiles around the average suggests that the chosen loads for renewable energy are indeed characterized by their consistent demand, which is beneficial for grid stability and efficient battery utilization.

Figure 3.9 illustrates the simulated load profile for those loads planned to be connected to the Kenyan grid. These profiles are more varied with higher peaks, which is indicative of loads that have less predictable consumption patterns and higher peak demands. Such characteristics make these loads more suitable for connection to a grid that is not as susceptible to the fluctuations of renewable generation and has the infrastructure to handle more significant and sporadic demands.

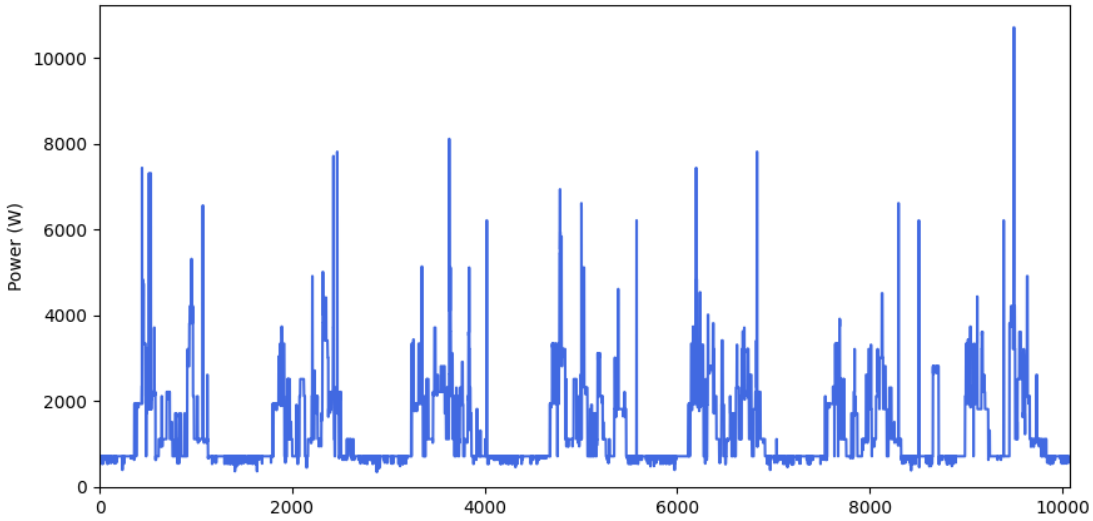

Figure 3.9: Power consumption pattern for the loads connected to the Kenyan grid during one week.

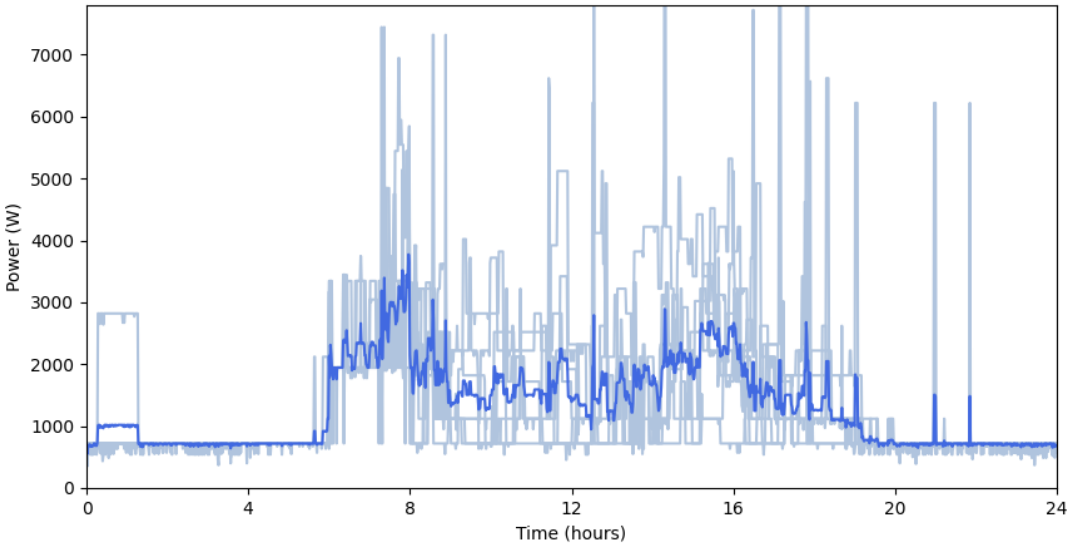

Figure 3.10: Average daily power consumption pattern for the loads connected to the Kenyan grid over the course of one week, with the dark blue curve being the average and the pale blue curves denoting individual days.

In Figure 3.10, the average daily power consumption for the Kenyan grid-connected loads is plotted. The variability between the average and individual days' consumption is more pronounced, showing the higher demand variability of these loads.

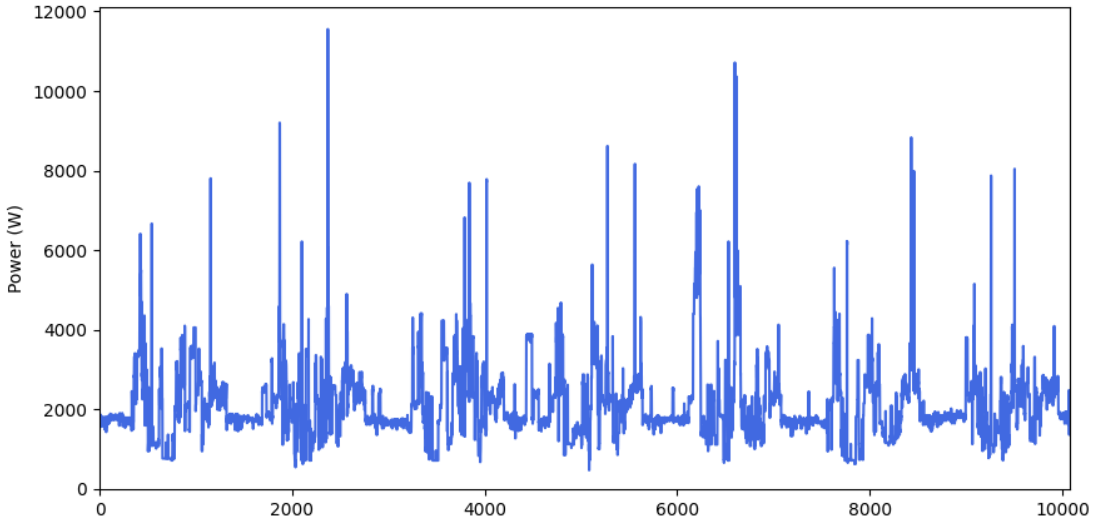

Figure 3.11: The total power consumption pattern across all the loads during one week.

Figure 3.11 combines the load profiles of both the renewable and Kenyan grid-connected loads, offering an aggregate view of the total power consumption pattern.

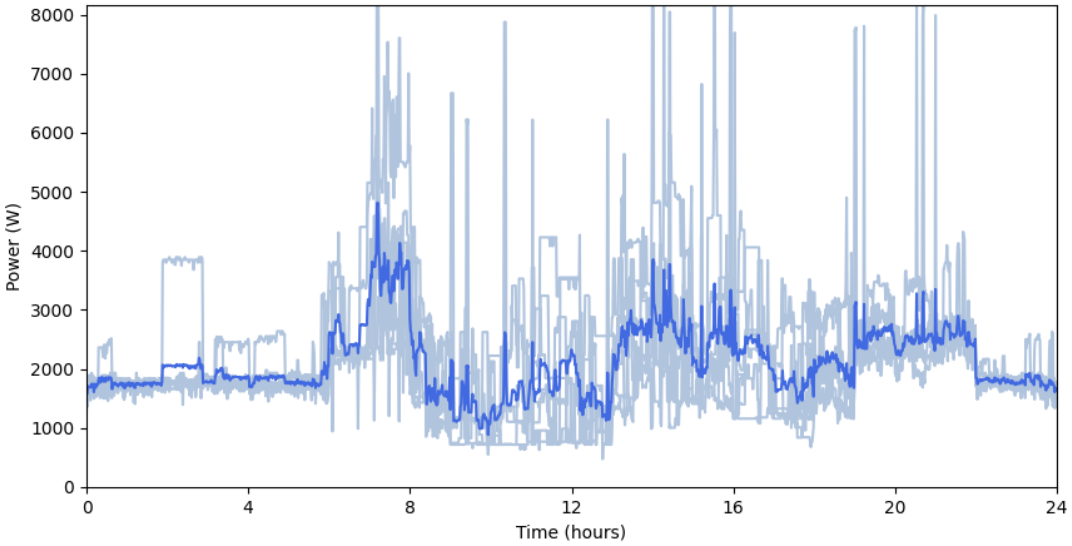

Figure 3.12: Average daily power consumption pattern for the entire facility loads over the course of one week, with the dark blue curve being the average and the pale blue curves denoting individual days.

Figure 3.12 provides the synthesized average daily power consumption pattern for all loads combined.

3.5. Load Profile for the Most Hectic Day of the Year

The load profile for the most hectic day of the year provides crucial insights into the peak and average power consumption patterns within a single day. This day represents the most challenging scenario for the resort's electrical system to manage, making it an ideal test case for evaluating energy storage

and generation systems in the proposed microgrid. The graph in Figure 3.13 illustrates the load power consumption measured in one-minute intervals throughout the day. Notable observations include a relatively stable power consumption of around 1600 W from midnight to 6 AM, indicating minimal activity during these hours. A significant and short-duration peak occurs at around 8 PM, reaching over 7400 W. This peak is likely due to the unplanned connection of a high-power device, as its brevity suggests it is not related to typical dining or entertainment activities. Throughout the day, the power usage exhibits periods of increased demand, particularly around midday and early evening, with peaks reaching up to 4, 5 and 6 kW. These periods correspond to operational tasks and guest activities such as meal preparation, housekeeping, and guest services. This dynamic load profile, characterized by significant fluctuations and high peaks, underscores the need for a robust and flexible energy management system capable of handling such demand variations. The data for this most hectic day will be interpolated to second resolution and used as a load time series for testing a microgrid model in Matlab/Simulink, providing a comprehensive scenario for system evaluation.

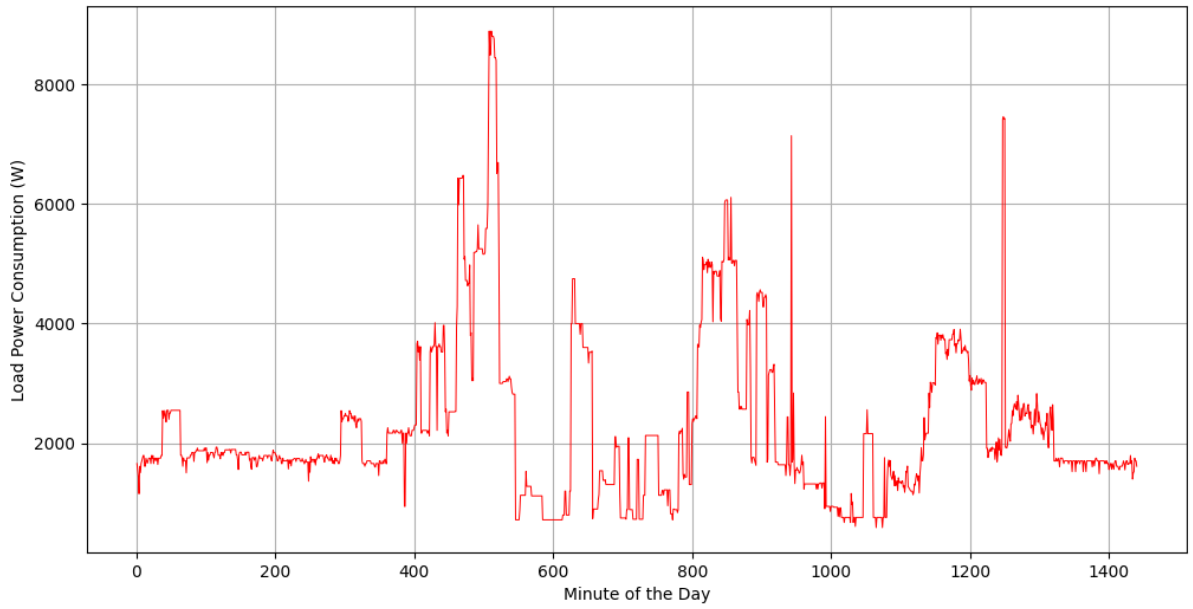

Figure 3.13: Load Profile for the Most Hectic Day of a Year

3.6. Summary and Analysis

This chapter presented a case study conducted at Kaya Imani Resort in Msambweni, Kenya, with the objective of developing and simulating a load profile of the resorts' potential microgrid. The electrical appliances for Kaya Imani Resort were simulated in Python using RAMP library, a robust open-source tool designed to construct multi-energy load profiles. Data for these simulations, including appliance power ratings, counts, and visitor consumption trends, was collected from thorough interviews with the resort's owner. These interviews provided the essential information needed to ensure that the simulation accurately reflected the resort's actual energy use, which is critical for the precise sizing of the energy storage and production systems. This detailed load analysis was not only used for academic purposes, but it had a direct practical application. The obtained specific energy requirements and consumption patterns were utilized by a local company for the precise sizing of the microgrid components.

Based on the simulations, strategic decisions were made regarding the allocation of loads to different energy sources. The choice to power stable, predictable loads with renewable energy aims to minimize the need for extensive energy storage, thus optimizing cost and efficiency. The loads with higher variability remain connected to the Kenyan grid, capitalizing on its ability to manage fluctuating demands.

The analysis of load duration curves and daily power consumption patterns plays an important role in understanding the energy demands throughout the resort. The resort's energy consumption under

various occupancy levels was analyzed and it was concluded that the occupancy levels of the resort do not contribute to the load profile significantly. The reason for that is the fact that numerous microgrid loads are not dependent on the number of visitors of the resort. Also, it was observed that the average increases in consumption are related to dining schedules and can be observed at around 8 A.M, 3 P.M, and 8 P.M.

With the simulation insights, the thesis will transition to exploring alternative microgrid topologies and storage strategies, suitable for broader application and not restricted to the case study's initial implementation. The goal is to design a system capable of providing the entire resort with reliable energy sourced entirely from renewables. The resort's full load profile serves as the basis for this, ensuring that the sustainability goals align with operational requirements.

4

Microgrid Components

This chapter presents the design, sizing, and control of the microgrid components for Kaya Imani Resort. It focuses on the solar PV array, lithium-ion battery system, reversible solid oxide cell (RSOC), and DC load. The solar PV array is sized based on solar irradiance data, with Jinko Solar JKM245P-60 panels selected for the installation. A configuration of 60 panels in 6 parallel strings of 10 panels each is determined. The array is connected to a 400V DC bus via a boost DC-DC converter, utilizing Maximum Power Point Tracking (MPPT) and constant voltage control modes. The lithium-ion battery system includes two parallel-connected battery packs, each with a total energy capacity of 9.8 kWh and a usable capacity of 8.8 kWh. The bidirectional DC-DC converter manages energy flow between the batteries and the DC bus, maintaining a constant DC bus voltage through an efficient control system. The RSOC functions in both solid oxide fuel cell (SOFC) and solid oxide electrolyzer cell (SOEC) modes, switching based on operational needs and hydrogen storage levels. The SOFC mode generates electricity from hydrogen, while the SOEC mode produces hydrogen using electrical energy. Transition times and control algorithms ensure smooth and stable operation. The DC load model dynamically adjusts according to Kaya Imani Resort's power consumption patterns, based on simulation data. A circuit breaker is included to protect the load from voltage deviations.

The planned microgrid is depicted in Figure 4.1 and consists of a solar PV array, lithium-ion battery system, reversible solid oxide cell (RSOC), and DC load, all connected to a 400 V DC bus bar.

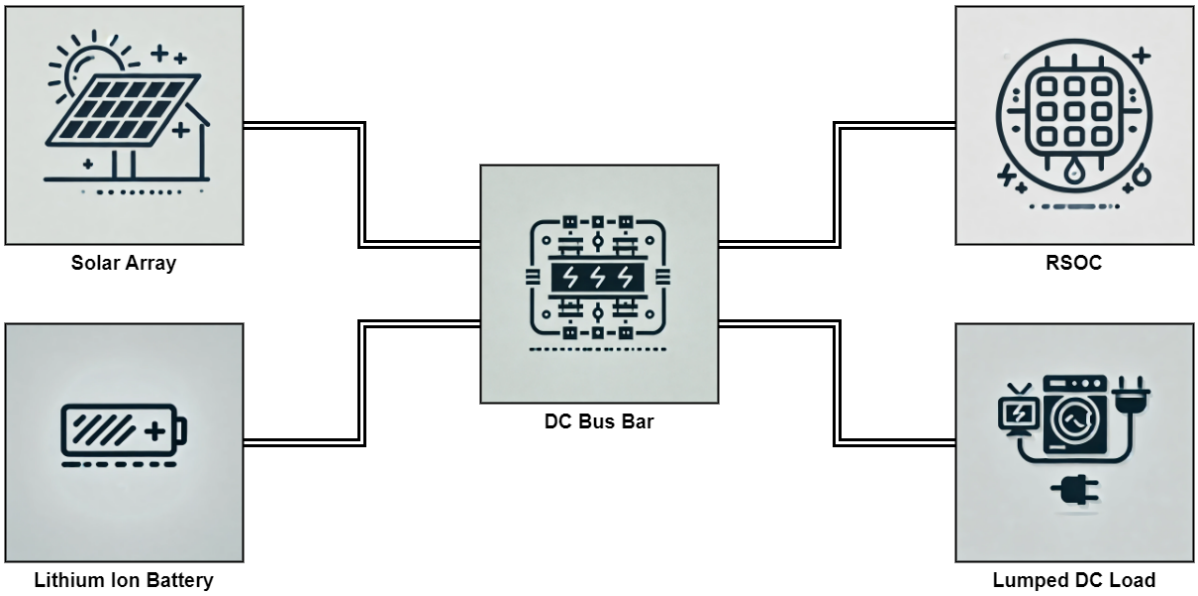

Figure 4.1: Simpliefied Microgrid Scheme

4.1. Solar PV Array

Kaya Imani Resort is ideally situated to harness solar energy due to its favorable climatic conditions and geographical location. To meet the average power consumption of the resort, an approximation for the size of a solar PV array is calculated based on various solar irradiance data. Key parameters such as Direct Normal Irradiation (DNI), Global Horizontal Irradiation (GHI), and Global Tilted Irradiation at Optimum Angle (GTI_opta) indicate substantial solar power potential in this region (see Figure 4.2b).

DNI is the average yearly, monthly, or daily sum of direct sunlight received per unit area that is perpendicular to the incoming sunlight. GHI measures the total amount of radiation received from above by a horizontal surface. It includes both direct sunlight and diffuse sky radiation. GTI_opta, on the other hand, represents the total solar radiation received by a surface tilted at the optimum angle, combining both direct and diffuse components for fixed-mounted PV modules [185].

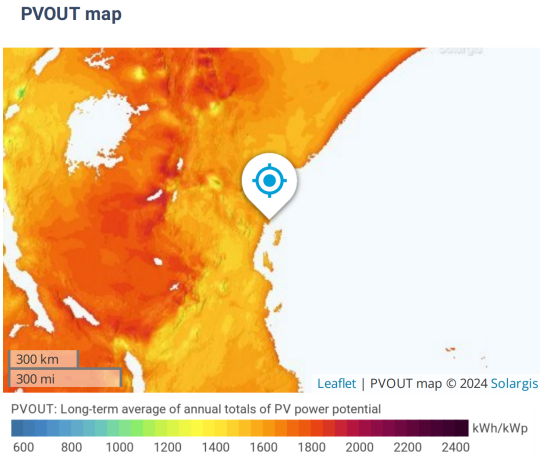

(a) PVOUT Map indicating PV power potential at Kaya Imani

Key Parameters	
PVOUT_specific:	1634 kWh/kWp
DNI:	1669.8 kWh/m²
GHI:	2060.1 kWh/m²
DIF:	830.9 kWh/m²
GTI_opta:	2064.2 kWh/m²
Average Temperature:	26.3 °C
Optimal Tilt Angle:	4°
ELE:	18 m

(b) Kaya Imani Resort location parameters

Figure 4.2: PV power potential and location parameters for Kaya Imani Resort [185].

The specific photovoltaic output (PVOUT_specific) denotes the yearly and monthly average values of photovoltaic electricity (AC) delivered by a PV system normalized to 1 kWp of installed capacity, where 'p' stands for working at peak power. The elevation (ELE) of the location above sea level also contributes to these calculations [185].

The average annual DNI of 1669.8 kWh/m² and GHI of 2060.1 kWh/m² provide a solid foundation for efficient solar energy conversion. Although higher temperatures, such as the average temperature of 26.3 °C, can reduce the efficiency of solar panels, the region's optimal tilt angle of 4° helps maximize solar input.

Figure 4.3 presents the average hourly profiles for direct normal irradiation at Kaya Imani. It is possible to notice that the maximal values do not exceed $700\,\mathrm{Wh/m^2}$.

Average hourly profiles

Direct normal irradiation [Wh/m^2]

	Jan	Feb	Mar	Apr	May	Jun	Jul	Aug	Sep	Oct	Nov	Dec
0 - 1												
1 - 2												
2 - 3												
3 - 4												
4 - 5												
5 - 6												
6 - 7	7	1		5	7	6	1	4	6	45	60	32
7 - 8	157	140	198	189	131	104	83	125	184	262	305	260
8 - 9	294	270	344	317	224	192	174	232	304	343	375	387
9 - 10	334	320	376	374	296	269	247	308	396	452	438	433
10 - 11	384	396	476	463	371	348	331	417	532	566	534	485
11 - 12	463	520	607	523	412	408	403	486	583	634	617	542
12 - 13	557	619	681	546	428	447	445	491	556	629	656	596
13 - 14	627	676	703	558	425	443	443	470	534	613	657	636
14 - 15	652	688	684	533	409	419	433	454	494	567	623	637
15 - 16	597	620	622	485	365	360	378	403	442	494	547	571
16 - 17	478	499	486	390	290	273	296	325	339	379	424	450
17 - 18	289	314	294	231	143	136	164	182	180	192	210	250
18 - 19	31	52	24	9		1	6	6	1	1	1	8
19 - 20												
20 - 21												
21 - 22												
22 - 23												
23 - 24												
Sum	4,871	5,116	5,495	4,622	3,502	3,406	3,402	3,903	4,550	5,178	5,448	5,287

Figure 4.3: Average Hourly Profiles of Direct Normal Irradiation

The average power per square meter can be calculated in the following way:

$$\text{Average Power per Square Meter} = \frac{1669.8\ \text{kWh/m}^2}{8760\ \text{h}} = 0.19\ \text{kW/m}^2 \tag{4.1}$$

4.1.1. Solar Array Sizing

The Jinko Solar JKM245P-60 [186] solar panel module was selected based on its widespread availability for purchase across various Kenyan websites. To ensure the adequacy of the design for its intended purpose, the current-voltage (IV) and power-voltage (PV) characteristics of the parameterized solar panel model were plotted and verified against the data-sheet [186]. The characteristics are presented in Figures 4.4b and 4.4a.

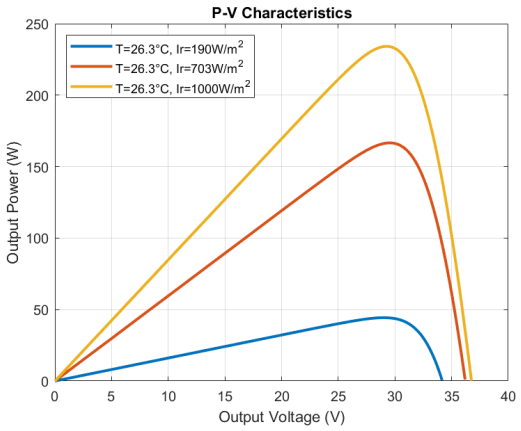

(a) Power-voltage (PV) characteristics of the solar panel.

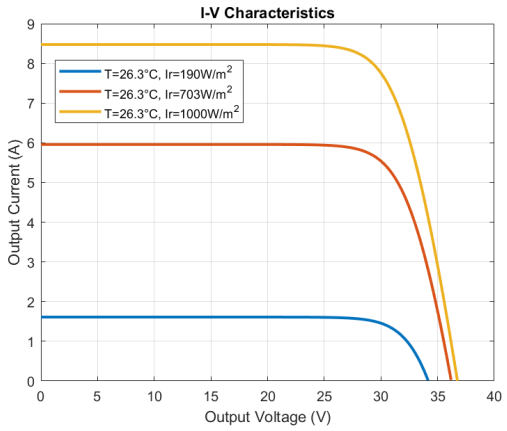

(b) Current-voltage (IV) characteristics of the solar panel.

Figure 4.4: IV and PV characteristics of the solar panel.

From Table 4.2, it is possible to see the characteristics of the Maximum Power Point (MPP) of the PV panel at different irradiances and at 26.3 °C. The average consumption of the resort is 2125 W. Taking into account the inefficiencies in the system are about 25%, the required power of the solar panel array can be calculated:

$$\text{Required power of solar array} = 2125 \cdot \frac{125\%}{100\%} = 2656.3\,\text{W} \tag{4.2}$$

The maximum power at the average irradiance of 190 W/m^2 is 44.3 W. Hence, the number of panels required in the array is:

$$\text{Number of panels} = \frac{2656.3}{44.3} \approx 60 \tag{4.3}$$

It was decided to connect panels in 6 parallel strings, with 10 panels in series comprising one string. This configuration ensures that the output voltage never exceeds 400V. Consequently, a boost DC-DC converter can be used to connect the array to a 400V DC bus. Additionally, in the model, a Voltage-Controlled Voltage Source is used to account for the 10 series panels, and a Current-Controlled Current Source is used to account for the 6 parallel strings. You can see the model of the solar array in Figure 4.5. A diode is incorporated to protect the array from potential current leaks from the DC bus. From Table 4.2, it is possible to see the parameters of solar panel specified in the model.

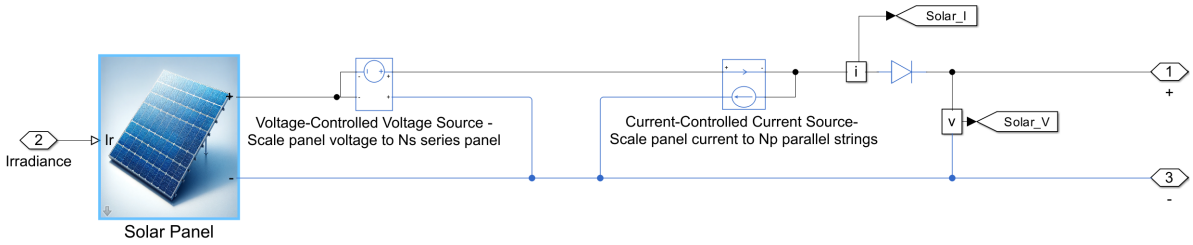

Figure 4.5: Solar array model configuration for Kaya Imani Resort

Table 4.1: Characteristics of the Solar Panel

Name	Value
Short-circuit current, Isc	8.47/1 A
Open-circuit voltage, Voc	36.9/60 V
Irradiance used for measurements, Ir0	1000 W/m^2
Quality factor, N	1
Series resistance, Rs	0.0063 Ohm
Number of series-connected cells per string	60
Number of parallel-connected strings	1

Table 4.2: Characteristics of Maximum Power Point (MPP) of the Solar Panel JKM245P-60 at 26.3 °C.

Irradiance (W/m^2)	Current at MPP (A)	Voltage at MPP (V)	Maximum Power (W)
190	1.5276	29.006	44.311
703	5.6402	29.537	166.59
1000	8.0031	29.256	234.14

4.1.2. DC-DC Converter for Solar Array

The solar array is connected to the DC bus via an average-value DC-DC converter block. This converter ensures efficient energy transfer from the solar panels to the DC bus, optimizing the power flow and maintaining system stability.

The average-value DC-DC converter operates as a boost converter with the following characteristics:

- **Control input**: Duty cycle
- **Converter type**: Boost converter
- **Converter efficiency**: Constant
- **Efficiency (%)**: 95

This converter steps up the voltage from the solar array to match the DC bus voltage, ensuring efficient power transfer with a constant efficiency of 95%. The duty cycle control input allows for precise regulation of the output voltage, optimizing the performance of the solar array in varying irradiance conditions.

4.1.3. Solar Array Control

The control of the solar array involves two main modes: Maximum Power Point Tracking (MPPT) and constant voltage control of the DC bus. This section describes the logic behind these control mechanisms, the parameters used, and the specific algorithm implemented for MPPT.

Control Modes

The system can switch between MPPT and constant voltage control modes based on the operational requirements. This is illustrated in Figure 4.6. In this figure, the `PV_Mode` signal determines whether the system operates in MPPT mode or constant voltage mode. When `PV_Mode` is active, the system uses the MPPT controller; otherwise, it maintains a constant DC bus voltage.

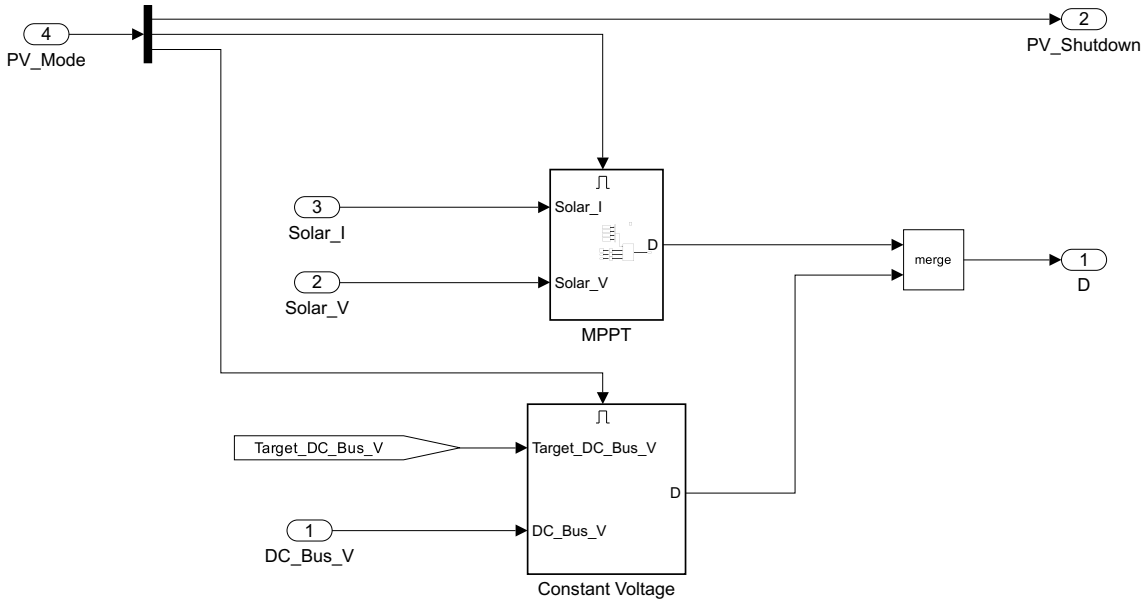

Figure 4.6: Control Mode Switching Between MPPT and Constant Voltage

MPPT Control

Maximum Power Point Tracking (MPPT) is a technique used to ensure that a solar panel operates at its maximum power point, regardless of changes in environmental conditions. The Perturb and Observe (P&O) algorithm is one of the most widely used methods for MPPT. The function for this algorithm is provided below:

```
function DutyCycle = PandO(params, isEnabled, voltage, current)
    % MPPT controller using the Perturb & Observe method.
    % DutyCycle output is Duty cycle of the boost converter (range: 0 to 1)
```

```
    % isEnabled input is 1 to enable the MPPT controller
    % voltage input is PV array terminal voltage (V)
    % current input is PV array current (A)
    % params input:
    %   params(1): Initial duty cycle value
    %   params(2): Maximum duty cycle
    %   params(3): Minimum duty cycle
    %   params(4): Step size for adjusting the duty cycle

    % Extract parameters
    initDutyCycle = params(1);
    maxDutyCycle = params(2);
    minDutyCycle = params(3);
    stepSize = params(4);

    % Persistent variables to hold previous values
    persistent prevVoltage prevPower prevDutyCycle;

    if isempty(prevVoltage)
        prevVoltage = 0;
        prevPower = 0;
        prevDutyCycle = initDutyCycle;
    end

    % Calculate power and differences
    power = voltage * current;
    voltageChange = voltage - prevVoltage;
    powerChange = power - prevPower;

    % Perturb and Observe logic
    if isEnabled
        if powerChange ~= 0
            if (powerChange < 0 && voltageChange < 0) || (powerChange > 0 && voltageChange >
                0)
                newDutyCycle = prevDutyCycle + stepSize;
            else
                newDutyCycle = prevDutyCycle - stepSize;
            end
        else
            newDutyCycle = prevDutyCycle;
        end
    else
        newDutyCycle = prevDutyCycle;
    end

    % Ensure duty cycle stays within bounds
    if newDutyCycle > maxDutyCycle
        newDutyCycle = maxDutyCycle;
    elseif newDutyCycle < minDutyCycle
        newDutyCycle = minDutyCycle;
    end

    % Update persistent variables
    prevDutyCycle = newDutyCycle;
    prevVoltage = voltage;
    prevPower = power;

    % Output the new duty cycle
    DutyCycle = newDutyCycle;
end
```

The MPPT control logic is shown in Figure 4.7.

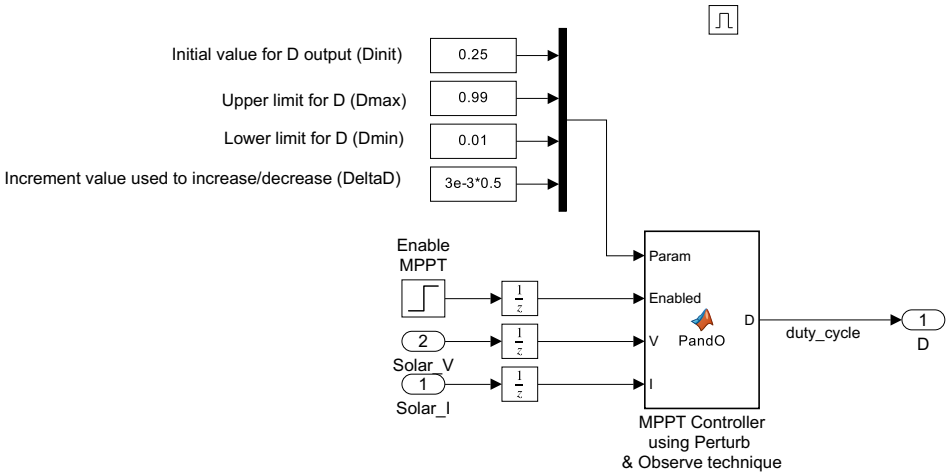

Figure 4.7: MPPT Controller using Perturb & Observe technique

Constant Voltage Control

The constant voltage control mode ensures that the DC bus voltage is maintained at a target level, irrespective of the solar panel output. This control mode is useful when the priority is to stabilize the DC bus voltage rather than maximizing the power output from the solar panels. The control logic for this mode is shown in Figure 4.8.

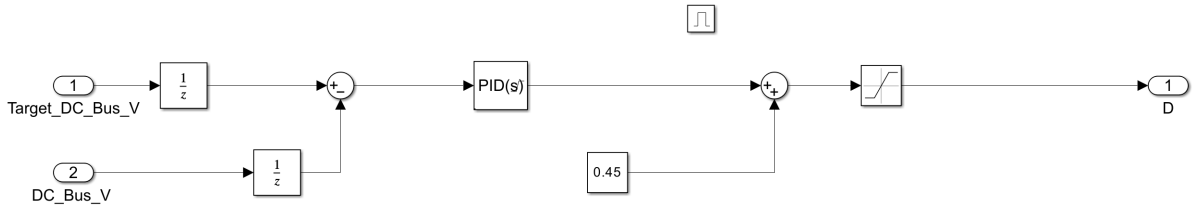

Figure 4.8: Constant Voltage Control for the DC Bus

PID Controller Parameters

The PID controller is used for maintaining the DC bus voltage at the desired level in the constant voltage mode. The parameters for the PID controller and the saturation limits are shown in Table 4.3.

Table 4.3: PID Controller Parameters and Saturation Limits

Parameter	Value
Proportional (P)	0.00085
Integral (I)	1.1
Derivative (D)	0
Upper limit	0.54
Lower limit	-0.45

Summary

The Jinko Solar JKM245P-60 solar panels were selected. The required average power was calculated to be approximately 2656.3 W. To meet this requirement, 60 panels were configured in 6 parallel strings of 10 panels each, ensuring the output voltage does not exceed 400V. This configuration allows for efficient integration with a boost DC-DC converter connected to a 400V DC bus. A diode is incorporated to protect the array from potential current leaks from the DC bus.

The solar array control system can operate in two modes: MPPT mode and constant voltage mode. The MPPT mode uses the Perturb & Observe algorithm to ensure maximum power output from the solar panels. The constant voltage mode, on the other hand, maintains the DC bus voltage at a set target, which is crucial for the stability of the power system. The system can dynamically switch between these modes based on the operational needs, ensuring both efficiency and stability.

4.2. Lithium-ion battery

4.2.1. Battery System in Microgrid

The battery system used in the microgrid consists of two battery packs connected in parallel. This section describes the battery specifications, how it is modeled, and the control system used to manage the battery operations.

Battery Specifications

The battery packs used in the system have the following specifications [187]:

- **Total Energy Capacity**: 9.8 kWh
- **Usable Energy Capacity**: 8.8 kWh
- **Battery Capacity**: 189 Ah
- **Voltage Range**: 42.0 to 58.8 V DC
- **Nominal Voltage**: 51.8 V DC
- **Max. Charge/Discharge Current**: 119A
- **Peak Current**: 166.7A for 3 seconds
- **Short Circuit Current**: 2.853kA
- **Max. Charge/Discharge Power**: 5.0 kW
- **Peak Power**: 7.0 kW for 3 seconds
- **Round-Trip Efficiency**: >95
- **Communication Interface**: CAN 2.0B
- **DC Disconnect**: Circuit Breaker, Contactor, Fuse
- **Battery Chemistry**: Lithium-Ion
- **Operating Temperature Range**: -10 to 50°C
- **Recommended Operating Temperature**: 15 to 30°C
- **Storage Temperature Range**: -30 to 60°C for 7 days, -20 to 45°C for 6 months
- **Humidity**: 5
- **Altitude**: Max. 2,000m

- **Cooling Strategy**: Natural Convection
- **Ingress Rating**: IP55
- **Certification**: Safety Cell UL1642, Battery Pack CE / RCM / FCC / TUV (IEC 62619) / UL1973
- **Mechanical Dimensions**: Width 452 mm, Height 484 mm, Depth 227 mm
- **Weight**: 75 kg

Two such battery packs are connected in parallel to provide adequate storage capacity and power management for the microgrid system.

Battery Modeling

The battery is modeled as shown in Figure 4.9. This model includes key parameters such as voltage, current, and state of charge (SoC) measurements.

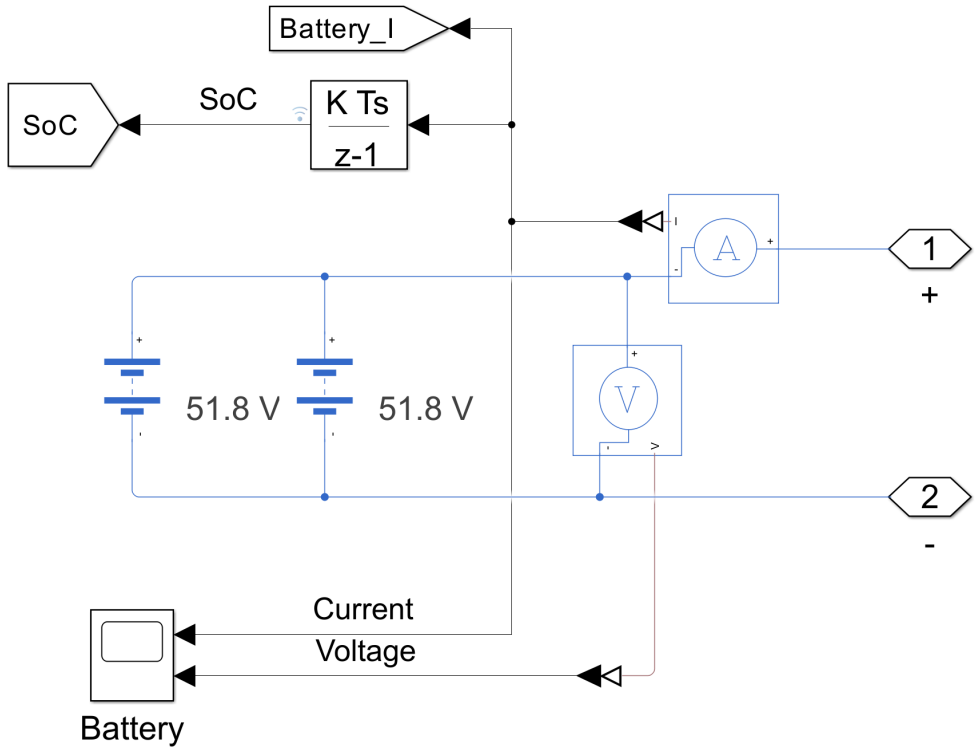

Figure 4.9: Battery Model

The state of charge (SoC) of the battery is tracked using a discrete integrator block. The parameters for this block are detailed in Table 4.4.

Table 4.4: State of Charge (SoC) Integrator Parameters

Parameter	Value
Gain value	$\frac{100}{(189*2)/3600}$
Initial condition	$\frac{(63*2)*100}{(189*2)}$

4.2.2. Bidirectional DC-DC Converter

The Bidirectional DC-DC Converter is a critical component in the battery control system, facilitating the flow of energy between the battery and the DC bus. This converter is controlled by a gate signal produced by the control system. The detailed parameters of the converter are provided in Table 4.5.

Table 4.5: Parameters of the Bidirectional DC-DC Converter

Name	Value	Unit
Modeling option	Nonisolated converter	
Fidelity level	Detailed model - switching devices	
Switching Devices		
Switching device	Averaged Switch	
On-state resistance	0.001	Ohm
Protection Diode		
Forward voltage	0.8	V
On resistance	0.001	Ohm
Off conductance	1×10^{-5}	1/Ohm
LC Parameters		
Inductance, L	1×10^{-5}	H
Capacitance, C1	0.005	F
Capacitance, C2	0.001	F
C1 effective series resistance	0.005	Ohm
C2 effective series resistance	0.005	Ohm

The Bidirectional DC-DC Converter is modeled as a nonisolated converter with a detailed model for switching devices. The switching device model used is an averaged switch with an on-state resistance of 0.001 Ohms. A protection diode with a forward voltage of 0.8 V, an on resistance of 0.001 Ohms, and an off conductance of 1×10^{-5} 1/Ohm is included. The LC parameters include an inductance of 1×10^{-5} H, capacitances of 0.005 F and 0.001 F for C1 and C2 respectively, and effective series resistances of 0.005 Ohms for both capacitors.

4.2.3. Battery Control System

The battery control system is designed to manage the charging and discharging of the battery packs to maintain the stability and efficiency of the power system. The control system can operate in two main modes: control for constant DC bus voltage and battery off mode. Within the control for constant DC bus voltage, there is a current control block that manages the current flow. The overall battery control system, which includes switching between the different control modes, is shown in Figure 4.10.

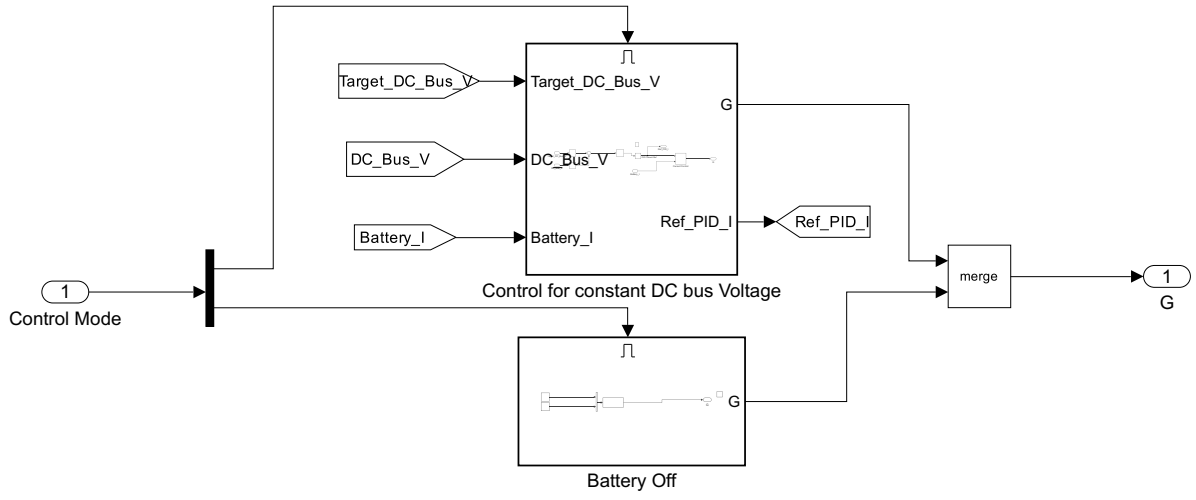

Figure 4.10: Battery Control System

Battery Off Mode

In this mode, the battery is disconnected from the system, and no charging or discharging occurs. This mode can be used for maintenance or safety purposes.

Control for Constant DC Bus Voltage

In this mode, the control system maintains the DC bus voltage at a specified target level. This is crucial for ensuring that the power supplied to the load is stable and within the desired voltage range. The control logic for maintaining constant DC bus voltage is shown in Figure 4.11. The control is implemented using a PI controller with saturation. The Proportional (P) and Integral (I) parameters are detailed in Table 4.7.

Parameter	Value
Proportional (P)	0.00085
Integral (I)	1.1
Saturation Limits	±119 A

Table 4.6: PID Parameters for the Voltage Control Logic with Saturation

The Proportional parameter (P) is set to 0.00085, which helps in reducing the overall error, and the Integral parameter (I) is set to 1.1, which helps in eliminating the residual steady-state error in the voltage control logic. The saturation limits are put to ±119 amps to ensure the current does not exceed the specified maximum charge/discharge current of the battery.

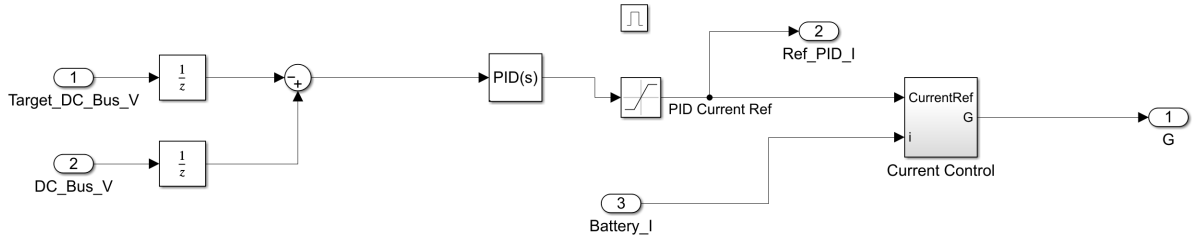

Figure 4.11: Control for Constant DC Bus Voltage

Current Control

Within the control for constant DC bus voltage block there is a current control block, which regulates the current flow to and from the battery to ensure optimal charging and discharging rates. This helps in maximizing the battery life and maintaining the efficiency of the power system. The current control logic is depicted in Figure 4.12. The control is implemented using a PID controller with saturation. The Proportional (P), Integral (I), and Derivative (D) parameters, along with the filter coefficient (N), are detailed in Table 4.7. The saturation limits are set to 0 and 0.9. The current reference is dictated by the outer voltage control loop.

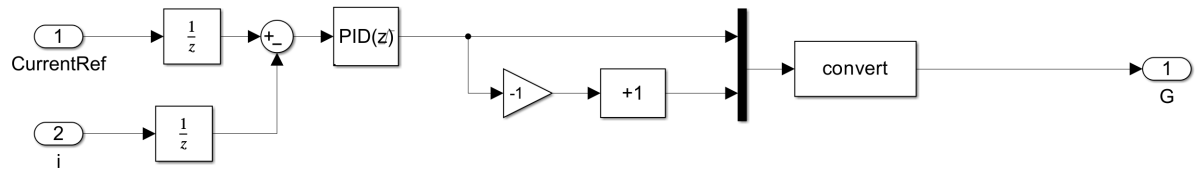

Figure 4.12: Current Control Logic

The Proportional parameter (P) is set to 0.00015, which helps in reducing the overall error. The Integral parameter (I) is set to 0.0035, which helps in eliminating the residual steady-state error in the voltage control logic. The Derivative parameter (D) is set to 0.00000028, and the filter coefficient (N) is set to 100. The saturation limits are set to 0 and 0.9 to ensure the control action remains within the specified range.

Parameter	Value
Proportional (P)	0.00015
Integral (I)	0.0035
Derivative (D)	0.00000028
Filter coefficient (N)	100
Saturation Limits	0 to 0.9

Table 4.7: PID Parameters for the Voltage Control Logic with Saturation

Summary
The battery system in the microgrid consists of two parallel-connected lithium-ion battery packs, each with a total energy capacity of 9.8 kWh and a usable energy capacity of 8.8 kWh. These batteries have a nominal voltage of 51.8 V DC, a maximum charge/discharge current of 119A, and a peak power of 7.0 kW for 3 seconds. The battery model includes key parameters such as voltage, current, and state of charge (SoC) measurements. The SoC is tracked using a discrete integrator block. A Bidirectional DC-DC Converter, controlled by a gate signal from the control system, manages the energy flow between the battery and the DC bus. It features detailed switching devices and LC parameters. The battery control system operates in two main modes: control for constant DC bus voltage and battery off mode. In constant DC bus voltage mode, a PI controller with saturation limits of ±119 amps is used. The current control block within this mode regulates the current flow using a PID controller.

4.3. Reversible Solid Oxide Cell

4.3.1. Modeling and Analysis of Solid Oxide Fuel Cell (SOFC) and Solid Oxide Electrolyzer Cell (SOEC)

This section describes the modeling of a Solid Oxide Fuel Cell (SOFC) and a Solid Oxide Electrolyzer Cell (SOEC) based on experimental data. The models include calculations of internal resistance, hydrogen consumption, power output, and efficiency. The data for both SOFC and SOEC were provided as voltage-current characteristics, and additional calculations were performed to derive necessary parameters for the models.

The voltage-current characteristics for the SOFC and SOEC are presented in Figures 4.13 and 4.14 and are based on a commercially available Solid Oxide Cells produced by Elcogen [188].

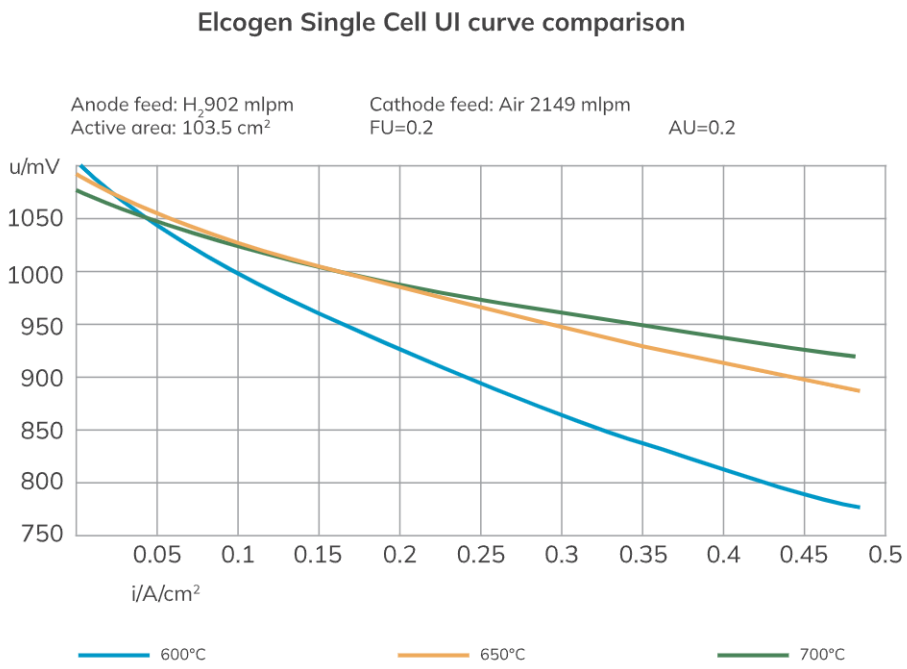

Figure 4.13: Voltage vs Current Density for SOFC

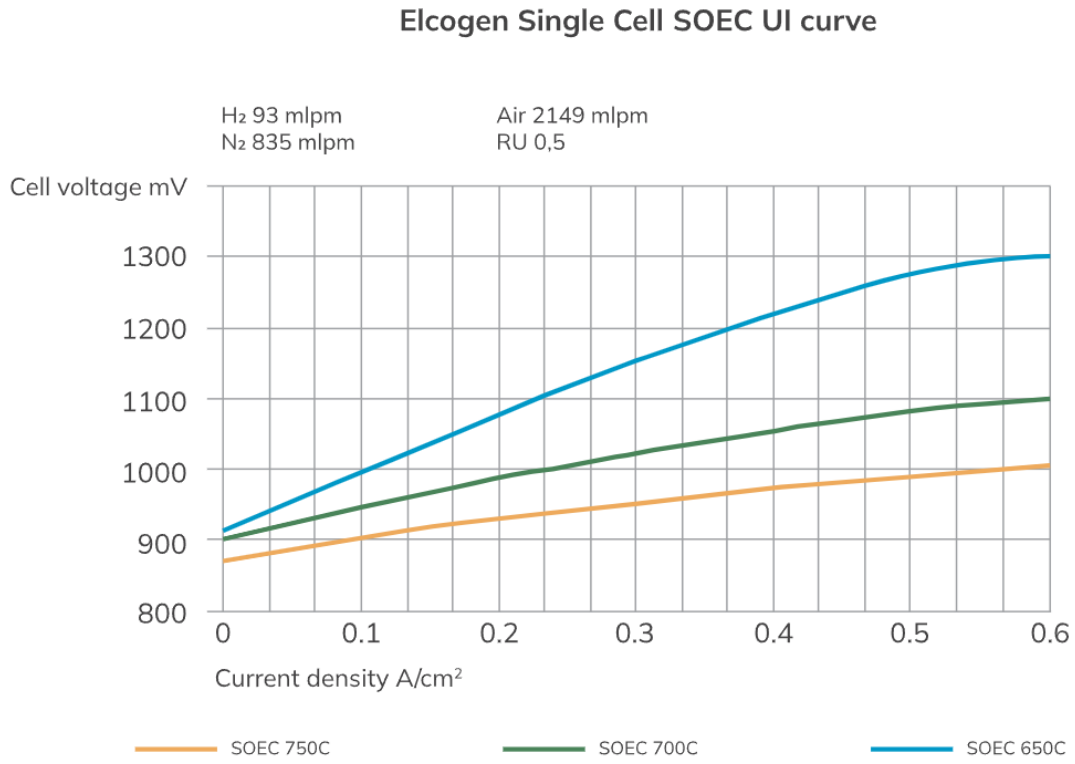

Figure 4.14: Voltage vs Current Density for SOEC

The active area of the cells is 103.5 cm^2. Thus, to convert current density (A/cm^2) to current (A), it is multiplied by the surface area: $I =$ Current density $\times$ Active area.

This conversion is applied to all current density values to obtain the current values used in the plots 4.16 and 4.17.

The power output for both SOFC and SOEC is calculated and plotted against the current. Power (P) is calculated as: $P = V \times I$, where V is the voltage and I is the current. From the graph it is possible to observe that the maximal power correlates with maximal current and has an almost linear relationship.

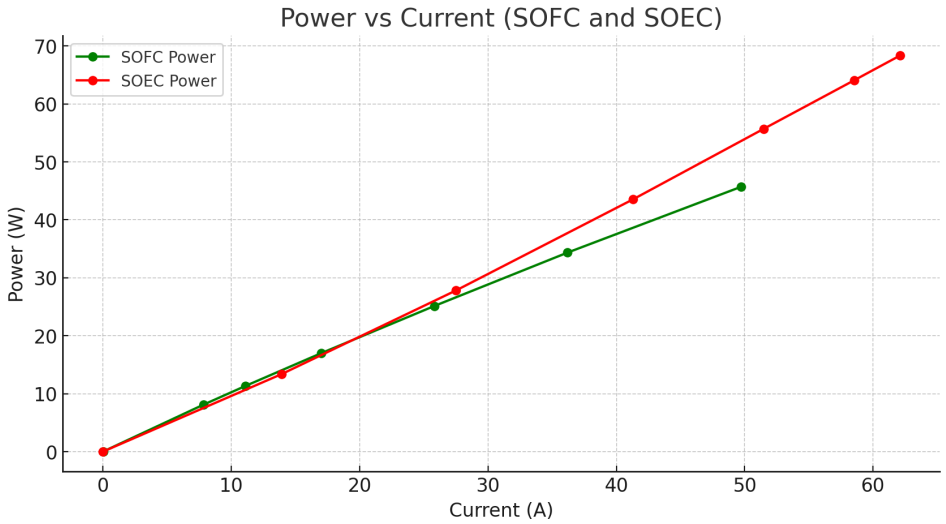

Figure 4.15: Power vs Current for SOFC and SOEC

4.3.2. Modeling SOFC

The SOFC can be represented as an ideal voltage source with an open-circuit voltage (V_{oc}) and a series resistance (R_{int}). By fitting the experimental data, it is possible to obtain the linear relationship:

$$V = V_{oc} - I \cdot R_{int} \tag{4.4}$$

Using linear regression on the provided data:

$$V_{oc} = 1.0756\,\text{V}, \quad R_{int} = 0.0030\,\Omega \tag{4.5}$$

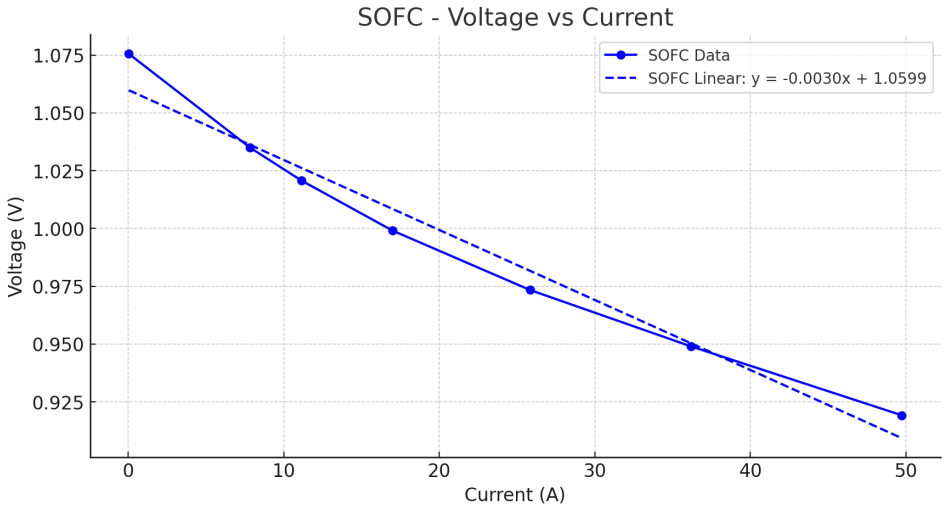

Figure 4.16: Linear fit for SOFC Voltage-Current Data

Given a hydrogen feed of 902 mL/min at 1 atm and 20°C, it is possible to convert this to SI units. The flow rate in m³/s is:

$$\dot{V} = \frac{902 \times 10^{-6}}{60}\,\text{m}^3/\text{s} = 1.5033 \times 10^{-5}\,\text{m}^3/\text{s} \tag{4.6}$$

Using the Ideal Gas Law ($PV = nRT$), the moles of hydrogen fed per second are calculated:

$$\dot{n}_{\text{feed}} = \frac{P \cdot \dot{V}}{R \cdot T} = \frac{101325 \times 1.5033 \times 10^{-5}}{8.314 \times 293.15} = 0.000625\,\text{mol/s} \tag{4.7}$$

With a utilization of 41.24%, the moles of hydrogen consumed per second are:

$$\dot{n}_{\text{consumed}} = 0.4124 \times 0.000625 = 0.00025775\,\text{mol/s} \tag{4.8}$$

At 700°C, the enthalpy of combustion for hydrogen is 241.8 kJ/mol:

$$\text{Energy input per second} = 0.00025775 \times 241800 = 62.32\,\text{J/s} \tag{4.9}$$

The maximum power output observed from the data is 45.71 W, thus the efficiency is:

$$\eta = \frac{45.71}{62.32} \times 100\% = 73.35\% \tag{4.10}$$

4.3.3. Modeling SOEC

Similar to the SOFC, the SOEC can be represented as an ideal voltage source with a series resistance. By fitting the experimental data, the linear relationship is obtained:

$$V = V_{oc} - I \cdot R_{int} \tag{4.11}$$

Using linear regression on the provided data:

$$V_{oc} = 0.901\,\text{V}, \quad R_{int} = 0.0032\,\Omega \tag{4.12}$$

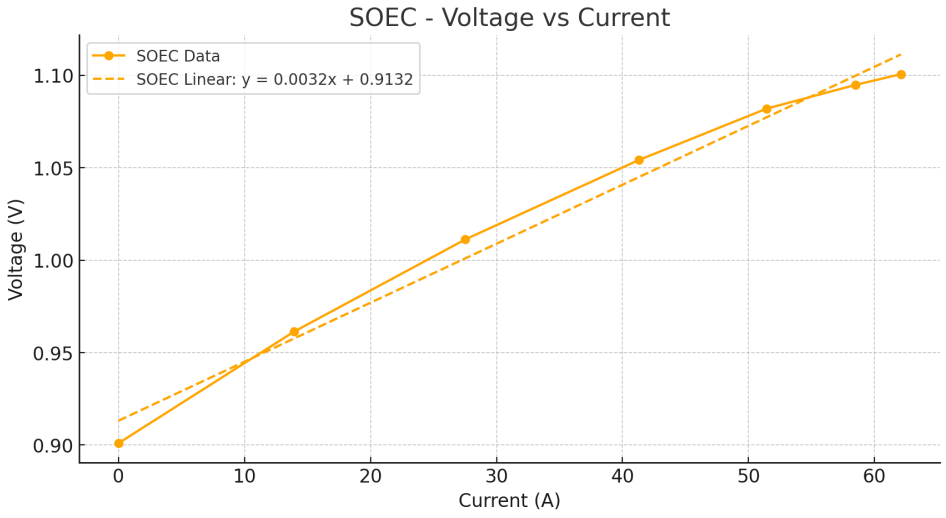

Figure 4.17: Linear fit for SOEC Voltage-Current Data

For SOEC, using the maximum current of 62.1 A, the hydrogen production rate using Faraday's law can be calculated:

$$\dot{n}_{\mathrm{H_2}} = \frac{I}{z \cdot F} = \frac{62.1}{2 \times 96485} = 0.000321 \,\text{mol/s} \tag{4.13}$$

At 700°C, the Gibbs free energy for water electrolysis is approximately 197 kJ/mol:

$$\text{Gibbs energy input per second} = 0.000321 \times 197000 = 63.237 \,\text{J/s} \tag{4.14}$$

With a maximum power input of 68.35 W the efficiency of electrolysis:

$$\eta = \frac{63.237}{68.35} \times 100\% = 92.52\% \tag{4.15}$$

4.3.4. Calculation of State of Hydrogen (SoH)

In order to ensure the desired energy security for a duration of 10 days, the required size of the hydrogen storage needs to be calculated. Additionally, it has been decided that at the beginning of the simulation, there would be enough hydrogen stored to meet the energy demand for 3 days. Hence, calculations for both the 10-day storage requirement and the initial 3-day storage starting point for the State of Hydrogen (SoH) are necessary.

To determine the amount of hydrogen needed for 10 days of energy consumption, the average consumption of 2125 W is obtained from the results of Kaya Imani resort load profile simulation. Over 10 days, the total energy required in watt-hours (Wh) is:

$$\text{Total Energy} = 2125 \,\text{W} \times 24 \,\text{hours/day} \times 10 \,\text{days} = 510000 \,\text{Wh} \tag{4.16}$$

Converting watt-hours to joules (J):

$$\text{Total Energy} = 510000 \,\text{Wh} \times 3600 \,\text{J/Wh} = 1836000000 \,\text{J} \tag{4.17}$$

Considering all the inneficiencies in the microgrid it can be assumed that a system efficiency is 65%. Then the actual energy needed is:

$$\text{Energy Needed} = \frac{1836000000 \,\text{J}}{0.65} = 2824615385 \,\text{J} \tag{4.18}$$

Considering the energy content of hydrogen (combustion enthalpy) is 241800 J/mol, the total moles of hydrogen required are:

$$\text{Total moles of hydrogen} = \frac{2824615385 \,\text{J}}{241800 \,\text{J/mol}} = 11682 \,\text{moles} \tag{4.19}$$

With a molar mass of 2.016 g/mol, the mass of hydrogen needed for 10 days is:

$$\text{Mass of hydrogen} = 11682 \,\text{moles} \times 2.016 \,\text{g/mol} = 23550.1 \,\text{g} \tag{4.20}$$

For a 3-day period, scaling down the 10-day requirement by a factor of 0.3:

$$\text{Mass of hydrogen (3 days)} = 23550.1 \,\text{g} \times 0.3 = 7065 \,\text{g} \tag{4.21}$$

The mass of hydrogen needed for 10 days is 23550 grams, and for 3 days it is 7065 grams.

4.3.5. RSOC Physics Model Description

The Reversible Solid Oxide Cell (RSOC) physics model integrates the functionalities of both Solid Oxide Fuel Cells (SOFC) and Solid Oxide Electrolyzer Cells (SOEC), allowing for efficient energy conversion and storage. The model dynamically switches between the SOFC and SOEC modes based on the operational requirements and hydrogen storage levels.

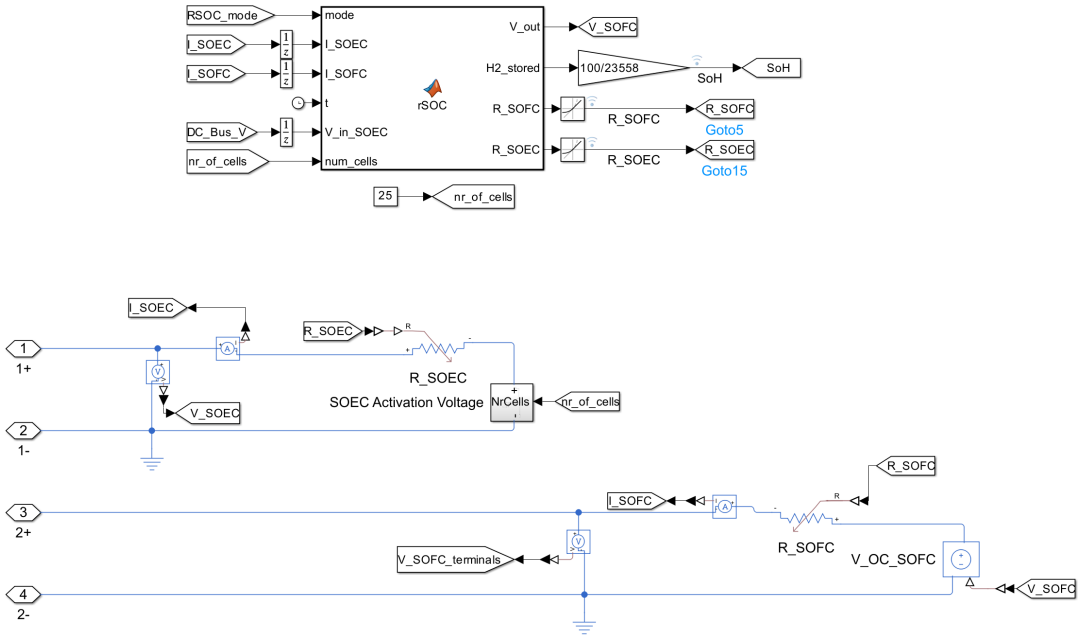

Figure 4.18: RSOC Model

Overview of the Model

The Reversible Solid Oxide Cell (RSOC) model is designed to capture the intricate interactions between the Solid Oxide Fuel Cell (SOFC) and Solid Oxide Electrolyzer Cell (SOEC) modes. This model incorporates essential components such as open-circuit voltages, internal resistances, and dynamic calculations for hydrogen consumption or production. The overall architecture of the RSOC model is depicted in Figure 4.18.

Key Components and Parameters

The RSOC model integrates multiple components and parameters to simulate the system's physical and operational characteristics accurately enough, while maintaining good speed of computations. It distinguishes between the SOFC and SOEC modes, each characterized by specific parameters. The model is scaled by the number of cells in the stack and electrically connected in series, which in this simulation is 25 cells.

The open-circuit voltage (V_{oc}) is a fundamental parameter for both modes. In SOFC mode, the V_{oc} is defined as the voltage on the contacts of the RSOC when it operates with a hydrogen flow rate of 902 ml per minute and an air flow rate of 2149 ml per minute, with no load attached (i.e., no current flowing). In this configuration, the V_{oc} is set at 1.0756 V per cell. For SOEC mode, the V_{oc} is lower, at 0.9132 V per cell, reflecting the voltage required for water electrolysis to produce hydrogen. Its scaling with the number of cells is depicted in Figure 4.19 and in the model it can be observer as SOEC Activation Voltage block, which exactly means that in order to start electrolysis process at least according voltage has to be applied to the cell. Similar scaling is applied to all the other components in the RSOC model.

Internal resistance (R_{int}) is crucial in determining the RSOC's efficiency and performance. The internal resistance for SOFC mode is 0.003 Ohms per cell, while for SOEC mode, it is slightly higher at 0.0032 Ohms per cell. These resistances are modeled by variable resistors configured to have the value of the internal resistance when the mode is active and a very large value when the mode is inactive to stop the current in that branch of the model.

The efficiency of each mode is also a key parameter. The SOFC mode operates at an efficiency of 73.35%, converting hydrogen into electrical energy. Conversely, the SOEC mode has a higher efficiency of 92.52%, corresponding to the conversion of electrical energy into hydrogen.

Additionally, the model dynamically calculates hydrogen storage, starting with an initial amount and adjusting based on the hydrogen consumed or produced during operation.

The maximum power capabilities of the RSOC stack in SOFC and SOEC modes are calculated based on the maximum power of a single cell and the number of cells in the stack.

Given the maximum power for one cell in SOFC mode is 45.71 W, and the stack consists of 25 cells, the maximum power capability of the stack in SOFC mode is calculated as follows:

$$P_{\text{max\_SOFC}} = 45.71\,\text{W} \times 25 = 1142.75\,\text{W} \tag{4.22}$$

Given the maximum power for one cell in SOEC mode is 68.35 W, and the stack consists of 25 cells, the maximum power capability of the stack in SOEC mode is calculated as follows:

$$P_{\text{max\_SOEC}} = 68.35\,\text{W} \times 25 = 1708.75\,\text{W} \tag{4.23}$$

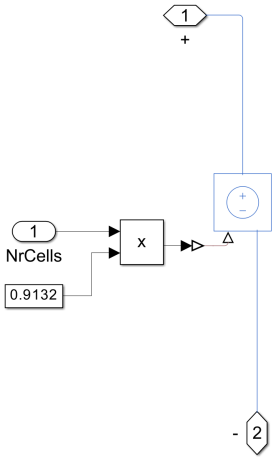

Figure 4.19: RSOEC Activation Voltage block

Operational Modes

The RSOC model operates in distinct modes, each with specific functionalities and calculations.

In SOFC mode, the RSOC functions as a fuel cell, consuming hydrogen to generate electricity. The output voltage (V_{out}) is determined by the open-circuit voltage (V_{oc}) adjusted by the voltage drop due to internal resistance (R_{int}). The hydrogen consumption is computed based on the electrical current (I_{SOFC}) and the efficiency of the SOFC, decrementing the hydrogen storage to reflect the updated state of the system. The voltage output in SOFC mode is modeled as follows:

$$V_{out} = V_{oc_{SOFC}} - I_{SOFC} \cdot R_{int_{SOFC}} \tag{4.24}$$

In SOEC mode, the RSOC acts as an electrolyzer, using electrical energy to produce hydrogen. Electrolysis begins when the input voltage (V_{in_SOEC}) exceeds the open-circuit voltage (V_{oc}). Hydrogen production is calculated based on the current flow (I_{SOEC}) and the efficiency of the SOEC, incrementing the hydrogen storage to reflect the accumulation of hydrogen.

The model includes logic for transitioning between SOFC and SOEC modes to ensure smooth and efficient switching as it is not physically possible to instantly transition from one mode to another. During

transitions, the system adjusts parameters to prevent abrupt operational changes. The transition time from SOFC to SOEC is set to 180 seconds, while the transition time from SOEC to SOFC is set to 150 seconds. If hydrogen storage depletes or the system is instructed to turn off, the RSOC enters a turned-off mode. In this state, both the SOFC and SOEC are effectively disconnected by setting their internal resistances to a very high value, halting any energy conversion processes.

Detailed Algorithm

The RSOC model initializes several persistent variables, such as hydrogen storage, current mode, and timers for mode transitions, to maintain the system's state across different simulation steps.

The model calculates the elapsed time since the last update to update dynamic variables such as hydrogen storage. The mode transition logic checks if the current mode differs from the input mode and initiates a transition if necessary. The transition completes after a predefined period, ensuring a smooth switch between modes.

Hydrogen storage management is crucial. In SOFC mode,the calculation for hydrogen is based on the electrical current and efficiency:

$$H_2\ consumed = \left(\frac{I_{SOFC} \cdot \text{num\_cells}}{2 \cdot 96485}\right) \cdot \text{dt} \cdot \text{efficiency}_{SOFC} \tag{4.25}$$

In SOEC mode, hydrogen is produced if the input voltage is sufficient, again based on current and efficiency:

$$H_2\ produced = \left(\frac{I_{SOEC} \cdot \text{num\_cells}}{2 \cdot 96485}\right) \cdot \text{dt} \cdot \text{efficiency}_{SOEC} \tag{4.26}$$

Voltage and resistance calculations are performed for both modes. For SOFC, the output voltage is:

$$V_{out} = V_{oc_{SOFC}} - I_{SOFC} \cdot R_{int_{SOFC}} \tag{4.27}$$

For SOEC, only if the input voltage is sufficient, the resistance is set to the internal resistance value to enable electrolysis.

During transitions or when the system is turned off, both SOFC and SOEC are effectively turned off by setting their resistances to a very high value. If the hydrogen storage depletes, the system automatically transitions to the turned-off mode, ensuring no energy conversion processes occur.

The RSOC physics model is governed by the following MATLAB function, which simulates the operational dynamics based on the input mode, currents, voltage, and time:

```
function [V_out, H2_stored, R_SOFC, R_SOEC] = rSOC(mode, I_SOEC, I_SOFC, t, V_in_SOEC,
    num_cells)
    % Parameters
    persistent H2_storage mode_transition_start current_mode transition_active last_time
        mode_off_time previous_mode

    % Initialize persistent variables if they are empty
    if isempty(H2_storage)
        H2_storage = 7065; % Initial hydrogen storage in grams
        mode_transition_start = -inf; % Timer start for mode transitions
        current_mode = mode; % Initial mode (0 = SOFC, 1 = SOEC, -1 = turned_off)
        transition_active = false; % Flag for transition state
        last_time = t; % Initialize last_time
        mode_off_time = -inf; % Timer for mode off state
        previous_mode = mode; % Initialize previous mode to track mode before turning off
    end

    % Constants
    V_oc_SOFC = 1.0756 * num_cells; % Open-circuit voltage for SOFC in volts
    R_int_SOFC = 0.003 * num_cells; % Internal resistance for SOFC in ohms
    V_oc_SOEC = 0.9132 * num_cells; % Open-circuit voltage for SOEC in volts
```

```
R_int_SOEC = 0.0032 * num_cells; % Internal resistance for SOEC in ohms
efficiency_SOFC = 0.7335; % Efficiency of SOFC
efficiency_SOEC = 0.9252; % Efficiency of SOEC
transition_time_SOFC_to_SOEC = 180; % 3 minutes in seconds
transition_time_SOEC_to_SOFC = 150; % 2.5 minutes in seconds
molar_mass_H2 = 2.016; % Molar mass of H2 in grams/mol
high_resistance = 1e6; % High resistance value for disconnected state

% Calculate elapsed time since the last update
dt = t - last_time;
last_time = t; % Update last_time for the next iteration

% Check hydrogen storage and set mode to turned_off if necessary
if H2_storage <= 0 && current_mode ~= -1
    previous_mode = current_mode; % Store the current mode before turning off
    current_mode = -1; % Set mode to turned_off
    mode_off_time = t; % Record the time when the mode is turned off
    H2_storage = 0;
end

% Check that SOEC or SOFC can kick in when in turned_off state
if current_mode == -1 && mode ~= -1
    if mode == previous_mode
        current_mode = mode; % Instant transition if mode is same as previous_mode
        transition_active = false; % Ensure no transition is active
    elseif (previous_mode == 0 && mode == 1 && (t - mode_off_time) >=
        transition_time_SOFC_to_SOEC) || ...
           (previous_mode == 1 && mode == 0 && (t - mode_off_time) >=
               transition_time_SOEC_to_SOFC)
        current_mode = mode; % Switch to the new mode if transition time has elapsed
        transition_active = false; % Ensure no transition is active
    end
end

% Mode transition logic
if mode ~= current_mode && current_mode ~= -1
    if !transition_active
        transition_active = true; % Flag indicating a transition is active
        mode_transition_start = t; % Record the start time of the transition
    elseif transition_active && ...
          ((current_mode == 0 && mode == 1 && (t - mode_transition_start) >=
              transition_time_SOFC_to_SOEC) || ...
           (current_mode == 1 && mode == 0 && (t - mode_transition_start) >=
               transition_time_SOEC_to_SOFC))
        current_mode = mode; % Complete the transition
        transition_active = false; % End the transition
    end
elseif mode == -1
    current_mode = -1; % Turned off by input signal
    transition_active = false; % Ensure no transition is active
end

% Compute outputs based on the current mode
if current_mode == 0
    % SOFC mode
    V_out = V_oc_SOFC;
    R_SOFC = R_int_SOFC;
    R_SOEC = high_resistance;
    H2_consumed_mol = (I_SOFC * num_cells / (2 * 96485)) * dt * efficiency_SOFC; %
        Calculate hydrogen consumption (moles)
    H2_consumed_g = H2_consumed_mol * molar_mass_H2; % Convert to grams
    H2_stored = H2_storage - H2_consumed_g; % Update hydrogen storage ensuring it is non-
        negative
elseif current_mode == 1
    % SOEC mode
    if V_in_SOEC >= V_oc_SOEC
        % Input voltage is large enough to start electrolysis
        V_out = 0; % Output voltage for SOEC is zero
        R_SOEC = R_int_SOEC; % Set SOEC resistor value
        R_SOFC = high_resistance; % Set SOFC resistor to a high value (disconnected)
        H2_produced_mol = (I_SOEC * num_cells / (2 * 96485)) * dt * efficiency_SOEC; %
```

```
                % Calculate hydrogen production (moles)
                H2_produced_g = H2_produced_mol * molar_mass_H2; % Convert to grams
                H2_stored = H2_storage + H2_produced_g; % Update hydrogen storage
            else
                % Input voltage is too low
                V_out = 0;
                H2_stored = H2_storage; % Hydrogen storage remains unchanged
                R_SOFC = high_resistance;
                R_SOEC = high_resistance;
            end
        else
            // Transitioning or turned_off mode
            V_out = 0; % No output voltage during transition or when turned_off
            H2_stored = H2_storage;
            R_SOFC = high_resistance;
            R_SOEC = high_resistance;
        end

        // Ensure that if transition is happening, neither regime can produce any power
        if transition_active == true
            R_SOFC = high_resistance;
            R_SOEC = high_resistance;
        end

        // Update hydrogen storage for the next iteration
        H2_storage = H2_stored;
    end
```

4.3.6. RSOC Converter

The RSOC converter depicted in Figure 4.20 employs separate buck and boost converters to manage the bidirectional power flow between the RSOC and the DC bus. This approach has been chosen after considering various factors, including control strategy, flexibility, scalability, and reliability.

One of the advantages of using separate buck and boost converters lies in the simplification of the control strategy. By having independent converters for each direction of power flow, the system can more precisely manage the distinct requirements of the SOFC and SOEC modes. The buck converter handles the step-down conversion during the SOEC mode, while the boost converter takes care of the step-up conversion during the SOFC mode. This separation allows for straightforward control of each converter, which reduces the overall complexity of the control system and enhances reliability and ease of implementation.

Flexibility and scalability is another notable benefit of this configuration. Using distinct converters allows the system design to be more easily tailored to meet the specific power requirements of the RSOC modes, as the maximal power of SOEC and SOFC modes are different, even though the same Solid Oxide Cell is used.

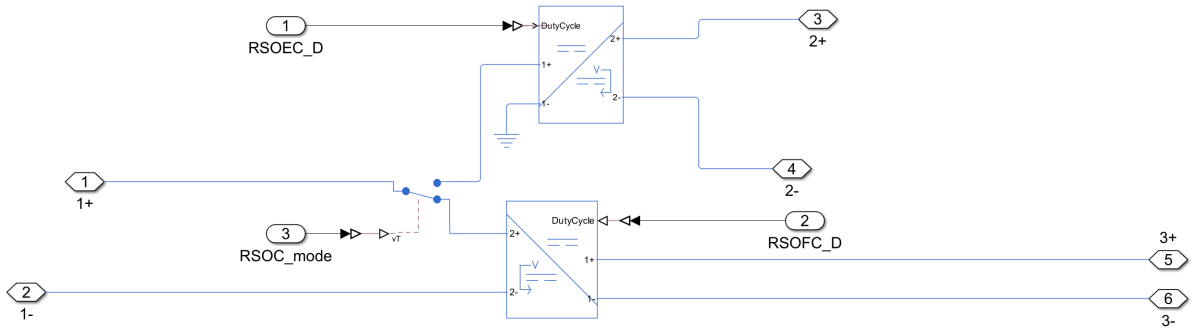

Figure 4.20: RSOC Converter

Besides, the use of separate converters can enhance the overall reliability of the system. In the event of a failure in one converter, the other can continue to function, ensuring that partial functionality is

maintained. This redundancy reduces the risk of total system failure.

However, the decision to use separate buck and boost converters also introduces some challenges. One disadvantage is the increased component count, which can lead to a more complex system design. This complexity requires additional space and potentially higher costs for components and assembly. The increased number of components also necessitates careful coordination to ensure seamless operation between the converters. Maintenance can also become more challenging, as troubleshooting and repair may require more specialized knowledge and effort.

Additionally, while each converter can be optimized for its specific function, managing two separate conversion processes may introduce inefficiencies, particularly during transitions between modes. These transitions can cause additional power losses, affecting the overall performance of the system.

In summary, the use of separate buck and boost converters in the RSOC converter design offers benefits such as simplified control, flexibility, scalability, and slightly improved reliability. However, it also presents challenges, including increased component count, design and maintenance complexity, and potential for higher losses. The choice of this approach reflects a strategic decision to balance these factors to achieve a robust and efficient system suitable for the specific requirements of RSOC applications.

4.3.7. RSOC Control System

The control system for the RSOC, depicted in Figure 4.21, manages the transition between SOFC and SOEC modes to maintain optimal performance and efficiency. It consist of SOEC and SOFC control blocks, which are activated by an external control signal from the microgrid supervision control unit, in the figure the signal is marked as RSOC_mode.

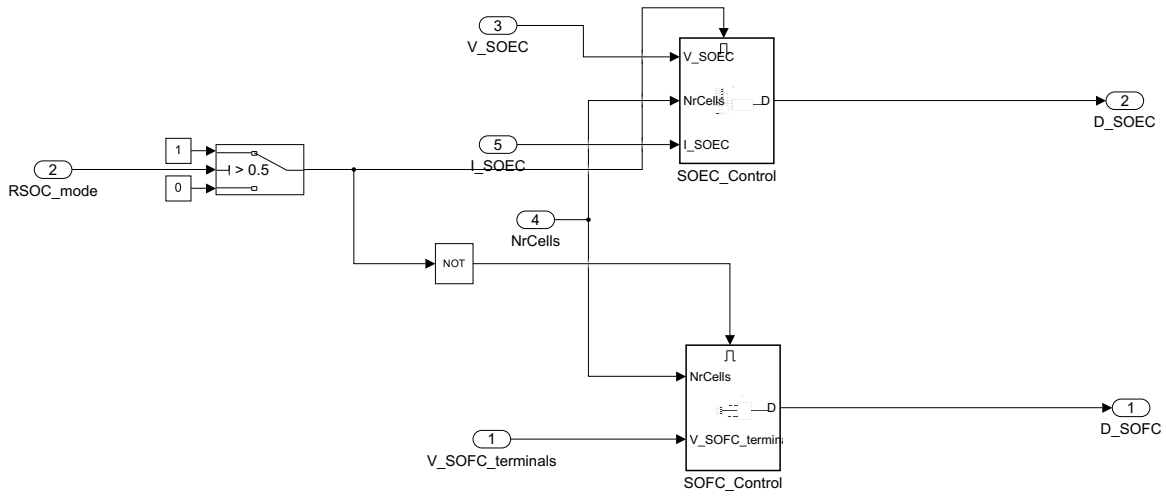

Figure 4.21: RSOC Control Diagram

SOEC Control

The SOEC control block is designed to regulate the duty cycle of the converter to achieve the desired power output. The control algorithm adjusts the duty cycle based on the difference between the current power and the goal power, ensuring that the system operates efficiently and within safe limits. The function `SOEC_Control` implements this logic as follows:

The function starts by extracting the initial values from the input vector, which include the initial duty cycle (D), the upper and lower limits of the duty cycle (D_max and D_min), and the base increment value (base_delta_D). These parameters provide the necessary constraints and initial settings for the control algorithm.

The goal power (P_goal) is calculated based on the number of cells (NrCells) in the stack. In this case, P_goal is set to 69 times the number of cells. This value represents the target power output that the control system aims to achieve.

Next, the function calculates the current power (P_current) by multiplying the voltage and current. This step provides the real-time power output of the system, which is essential for determining the necessary adjustments to the duty cycle.

The difference between the goal power and the current power (delta_P) is then calculated. This difference indicates how much the current power deviates from the target, guiding the subsequent adjustments to the duty cycle.

To ensure a responsive control system, the function calculates an adaptive increment value (delta_D). This value is derived by multiplying the base increment value (base_delta_D) by the absolute value of delta_P divided by P_goal. The adaptive nature of delta_D allows the control system to make larger adjustments when the deviation is significant and finer adjustments when the system is close to the target.

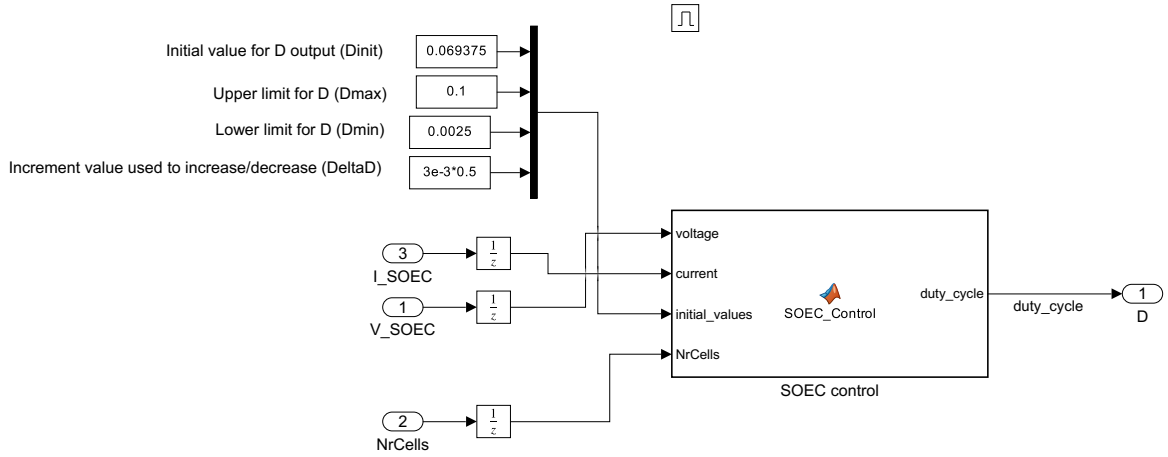

Figure 4.22: SOEC Control Diagram

The core of the control algorithm adjusts the duty cycle (D) based on the current power relative to the goal power. If P_current is less than P_goal, the duty cycle is increased by delta_D to boost the power output. Conversely, if P_current exceeds P_goal, the duty cycle is decreased by delta_D to reduce the power output. These adjustments help maintain the system's power output close to the desired level.

Finally, the function ensures that the duty cycle remains within the specified limits. If the adjusted duty cycle exceeds the upper limit (D_max), it is set to D_max. If it falls below the lower limit (D_min), it is set to D_min. This step prevents the duty cycle from going beyond safe operational boundaries.

The function returns the adjusted duty cycle, which is then used to control the converter, ensuring that the SOEC operates efficiently and meets the power requirements of the system. The code for the SOEC control algorithm is provided below:

```
function duty_cycle = SOEC_Control(voltage, current, initial_values, NrCells)
    % initial_values is a vector containing:
    % initial_values(1): initial value of D
    % initial_values(2): upper limit of D
    % initial_values(3): lower limit of D
    % initial_values(4): base increment value

    % Extract initial values from the input vector
    D = initial_values(1);
    D_max = initial_values(2);
    D_min = initial_values(3);
    base_delta_D = initial_values(4);

    % Goal power
    P_goal = 69 * NrCells;
```

```
    % Calculate the current power
    P_current = voltage * current;

    % Calculate the difference between the current power and the goal power
    delta_P = P_goal - P_current;

    % Calculate the adaptive increment value
    delta_D = base_delta_D * abs(delta_P) / P_goal;

    % Power control algorithm
    if P_current < P_goal
        D = D + delta_D;
    elseif P_current > P_goal
        D = D - delta_D;
    end

    % Limit the duty cycle to the specified range
    if D > D_max
        D = D_max;
    elseif D < D_min
        D = D_min;
    end

    % Return the adjusted duty cycle
    duty_cycle = D;
end
```

SOFC Control

The SOFC control block is designed to regulate the duty cycle of the converter to maintain the desired voltage output. The control algorithm adjusts the duty cycle based on the difference between the current voltage and the goal voltage, ensuring that the system operates efficiently and within safe limits. The function `SOFC_Control` implements this logic as follows:

The function begins by extracting the initial values from the input vector, which include the initial duty cycle (D), the upper and lower limits of the duty cycle (D_max and D_min), and the base increment value (base_delta_D). These parameters establish the necessary constraints and initial settings for the control algorithm.

The goal voltage (V_goal) is calculated based on the number of cells (NrCells) in the stack. In this instance, V_goal is set to 0.91 times the number of cells. This value represents the target voltage output that the control system aims to achieve.

Next, the function calculates the difference between the current voltage and the goal voltage (delta_V). This difference indicates how much the current voltage deviates from the target, guiding the subsequent adjustments to the duty cycle.

To ensure a responsive control system, the function calculates an adaptive increment value (delta_D). This value is derived by multiplying the base increment value (base_delta_D) by the absolute value of delta_V divided by V_goal. The adaptive nature of delta_D allows the control system to make larger adjustments when the deviation is significant and finer adjustments when the system is close to the target.

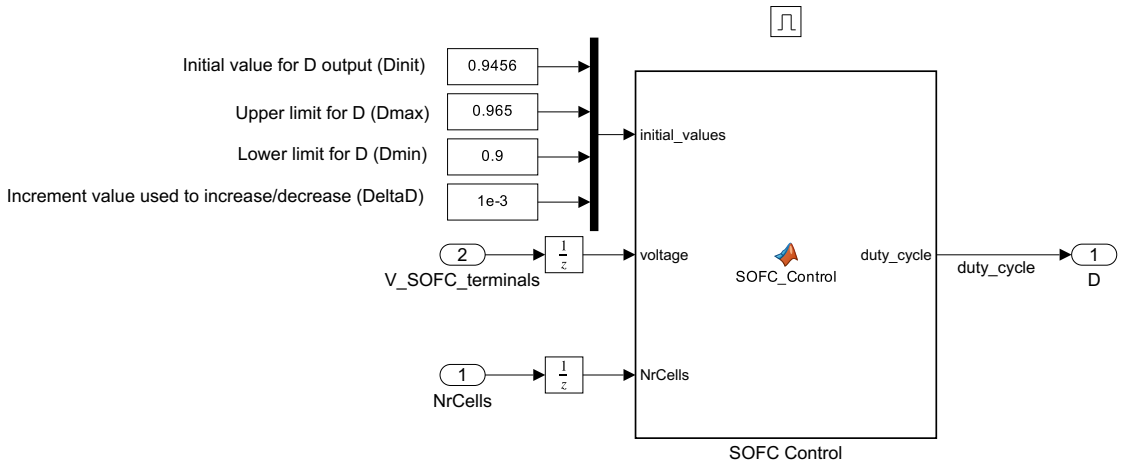

Figure 4.23: SOFC Control

The core of the control algorithm adjusts the duty cycle (D) based on the current voltage relative to the goal voltage. If the current voltage is less than the goal voltage, the duty cycle is increased by delta_D to boost the voltage output. Conversely, if the current voltage exceeds the goal voltage, the duty cycle is decreased by delta_D to reduce the voltage output. These adjustments help maintain the system's voltage output close to the desired level.

Finally, the function ensures that the duty cycle remains within the specified limits. If the adjusted duty cycle exceeds the upper limit (D_max), it is set to D_max. If it falls below the lower limit (D_min), it is set to D_min. This step prevents the duty cycle from going beyond safe operational boundaries.

The function returns the adjusted duty cycle, which is then used to control the converter, ensuring that the SOFC operates efficiently and meets the voltage requirements of the system.

It is important to note that the SOFC control block does not manage the DC bus voltage directly. Instead, it focuses on maximizing the output power of RSOFC whenever possible. The SOFC aims to deliver its maximum power output, subject to the constraints of the control algorithm and the operational conditions. This approach ensures that the fuel cell operates at its peak capacity, contributing to the overall energy output of the system.

The control algorith of the RSOFC can be seen below:

```
function duty_cycle = SOFC_Control(voltage, initial_values, NrCells)
    % initial_values is a vector containing:
    % initial_values(1): initial value of D
    % initial_values(2): upper limit of D
    % initial_values(3): lower limit of D
    % initial_values(4): base increment value
```

```
    % Extract initial values from the input vector
    D = initial_values(1);
    D_max = initial_values(2);
    D_min = initial_values(3);
    base_delta_D = initial_values(4);

    % Goal voltage
    V_goal = 0.91 * NrCells;

    % Calculate the difference between the voltage and the goal
    delta_V = V_goal - voltage;

    % Calculate the adaptive increment value
    delta_D = base_delta_D * abs(delta_V) / V_goal;

    % Incremental conductance algorithm
    if voltage < V_goal
        D = D + delta_D;
    elseif voltage > V_goal
        D = D - delta_D;
    end

    % Limit the duty cycle to the specified range
    if D > D_max
        D = D_max;
    elseif D < D_min
        D = D_min;
    end

    % Return the adjusted duty cycle
    duty_cycle = D;
end
```

Summary

The RSOC model effectively integrates both SOFC and SOEC functionalities, allowing for efficient energy conversion and storage. The model includes detailed parameters such as open-circuit voltages, internal resistances, and efficiencies, tailored for each mode. The SOFC mode operates with a V_{oc} of 1.0756 V per cell and an internal resistance of 0.003 Ohms per cell, while the SOEC mode operates with a V_{oc} of 0.9132 V per cell and an internal resistance of 0.0032 Ohms per cell. The system dynamically adjusts hydrogen storage, which starts with an initial amount and changes based on consumption or production.

The operational modes are carefully managed to ensure smooth transitions and efficient performance. The SOFC mode generates electricity by consuming hydrogen, while the SOEC mode produces hydrogen using electrical energy. Transition times between modes are set to 180 seconds from SOFC to SOEC and 150 seconds from SOEC to SOFC to ensure stability and prevent abrupt changes.

The control system for the RSOC, depicted in Figure 4.21, utilizes separate control algorithms for SOFC and SOEC modes. The SOEC control algorithm adjusts the duty cycle to maintain the desired power output, while the SOFC control algorithm regulates the duty cycle to maintain the desired voltage output. It is important to note that the SOFC control block does not manage the DC bus voltage directly but focuses on maximizing the output power of the RSOC whenever possible.

The RSOC converter employs separate buck and boost converters to handle the bidirectional power flow, offering advantages in control precision, flexibility, and reliability. However, this approach also introduces challenges such as increased component count and design complexity.

Overall, the RSOC model and its control system provide a robust framework for simulating and managing the dual functionalities of energy conversion and hydrogen production, ensuring good performance and efficiency in varying operational conditions.

4.4. DC load

In this section, the DC load connected to the microgrid is described. The load is directly connected to the DC bus and is modeled as a simplified aggregated load. In a real-world scenario, this load would

consist of multiple step-down converters powering various household appliances.

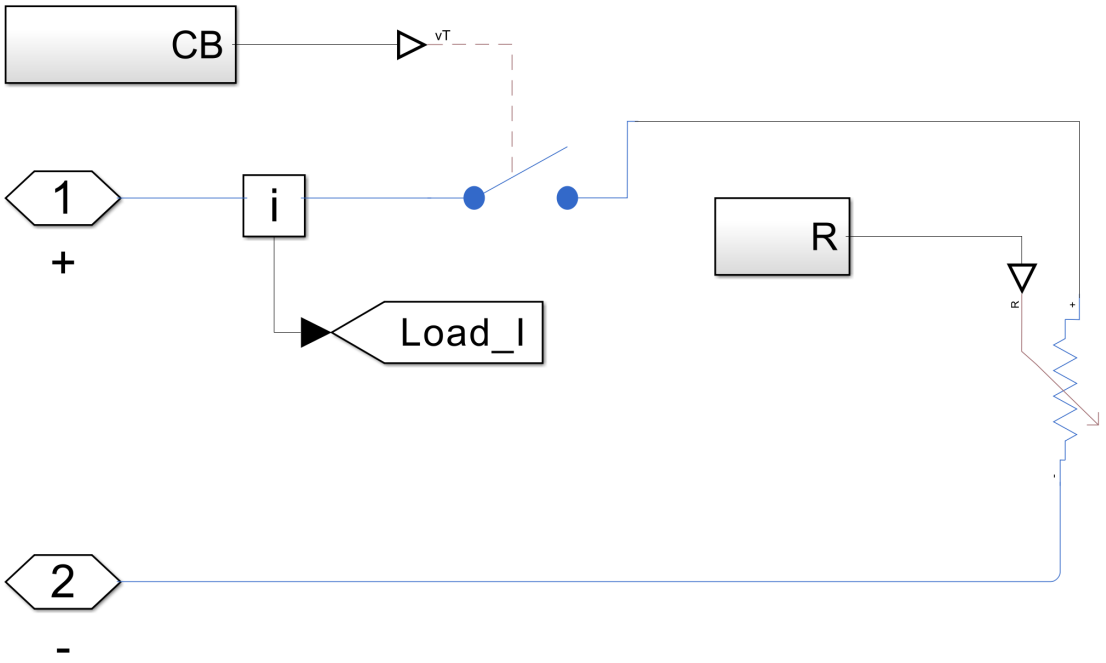

Figure 4.24: DC Load Configuration

The DC load is modeled to dynamically adjust according to the power requirements. Figure 4.24 shows the overall configuration of the load model, where the load power requirement is specified in terms of power consumption.

The load power is dictated from a CSV file, which is the output of the load profile simulation of Kaya Imani Resort. This data provides the power demand at each time step, ensuring that the load model accurately reflects the actual power consumption patterns observed in the resort. Besides the load, the diagram also includes a circuit breaker (CB). This circuit breaker is designed to activate if the DC bus voltage remains outside the operational range for a period exceeding the maximum allowed duration.

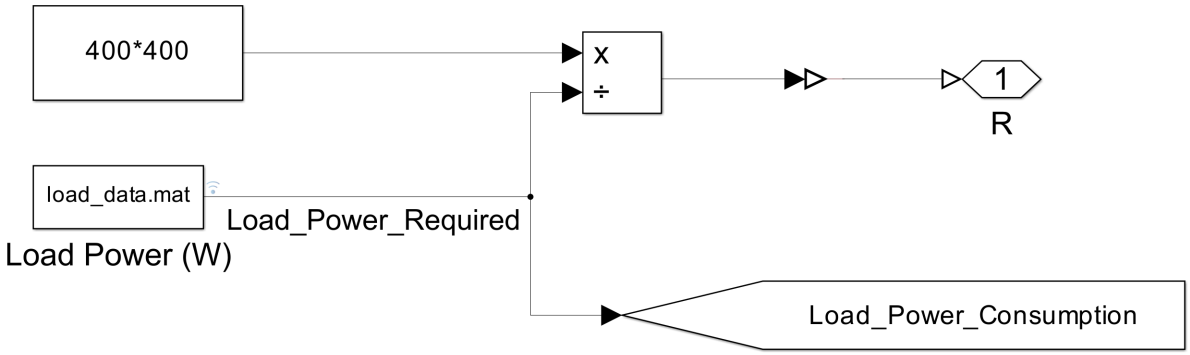

Figure 4.25: DC Load Resistor Configuration

The load is represented as a resistor whose value is calculated based on the desired power consumption, which is illustrated in Figure 4.25.

The power required by the load is provided from the CSV file and is used to calculate the required

resistance. This is achieved by dividing the square of the normal DC bus voltage by the specified load power, as shown in the following relationship:

$$R = \frac{V^2}{P} \tag{4.28}$$

where V is the voltage across the load and P is the load power requirement.

This simplified model streamlines the simulation by accurately representing aggregate power consumption based on the load profile, while in a real application, multiple step-down converters would manage household appliances.

4.5. Summary

This chapter detailed the design, sizing, and control mechanisms of the microgrid components. The components include the solar PV array, lithium-ion battery system, reversible solid oxide cell (RSOC), and DC load.

The solar PV array was designed based on solar irradiance data, selecting Jinko Solar JKM245P-60 panels. A configuration of 60 panels in 6 parallel strings of 10 panels each was established, connected to a 400V DC bus through a boost DC-DC converter. The converter operates with Maximum Power Point Tracking (MPPT) and constant voltage control modes, ensuring optimal energy conversion and system stability.

For energy storage, two lithium-ion battery packs were implemented, each offering a total energy capacity of 9.8 kWh and a usable capacity of 8.8 kWh. The battery system is interfaced with the DC bus via a bidirectional DC-DC converter, which efficiently manages energy flow and maintains the desired DC bus voltage.

The RSOC technology enables dual functionality, operating as both a Solid Oxide Fuel Cell (SOFC) and a Solid Oxide Electrolyzer Cell (SOEC). The system transitions smoothly between generating electricity from hydrogen and producing hydrogen using electricity, adapting to the resort's energy demands and hydrogen storage status.

The DC load model reflects the resort's power consumption patterns. A protective circuit breaker is incorporated to safeguard against voltage irregularities.

Overall, the chapter provides a detailed analysis of the microgrid's core components, illustrating how each element contributes to its sustainable and resilient energy infrastructure.

5

Microgrid Integration and Control

This chapter explores the integration and control of a microgrid system comprising a solar PV array, lithium-ion battery system, reversible solid oxide cell (RSOC), and DC load, all interconnected through a 400V DC bus. A detailed simulation is conducted over a 24-hour period with a millisecond resolution to analyze the microgrid's performance under various conditions. This resolution balances the need for accurate control response with the computational demands of a full-day simulation. Furthermore, this chapter delves into the hierarchical rule-based control strategy employed to maintain system stability and efficiency. The control system continuously monitors critical parameters such as DC bus voltage, battery state of charge, hydrogen levels, and solar irradiance. By adjusting the operational modes of the PV array, battery, RSOC, and load, the control system ensures optimal microgrid performance. This chapter provides insights into the integration of diverse energy components into a cohesive microgrid system and outlines the control mechanisms essential for maintaining its stability and efficiency.

5.1. Microgrid Configuration

This section describes the integration of various components into a single microgrid system, as illustrated in Figure 5.2. The simplified scheme can be wieved in Figure 5.1. The microgrid includes a solar PV array, lithium-ion battery system, reversible solid oxide cell (RSOC), and DC load, all interconnected via a 400V DC bus. The simulation is conducted for 86400 seconds with millisecond resolution, resulting in a timeframe with 86,400,000 points. This setup balances control accuracy and computational efficiency, enabling a realistic simulation of 24-hour operation. The solver used for the simulation is ode3.

The ode3 solver in Simulink, also known as the Bogacki-Shampine method, is a third-order Runge-Kutta solver used for numerical integration of ordinary differential equations. It offers a balance between accuracy and computational efficiency, making it suitable for real-time simulations and applications where a fixed step size is required. By taking three intermediate steps to compute the solution at each time step, ode3 provides better accuracy than first-order methods while being less computationally intensive than higher-order methods like ode45. This solver is particularly useful for problems where moderate accuracy is sufficient, and higher computational costs are not justified.

A 2 µF capacitor is used to stabilize the DC bus and reduce voltage ripple. The solar PV array generates electricity from solar irradiance, feeding power into the DC bus via an average-value DC-DC converter. The lithium-ion battery system, with its bidirectional DC-DC converter, manages energy storage and voltage stabilization. It allows the system to store excess energy when production is high and discharge energy when production is low, thus maintaining the stability of the DC bus voltage.

The RSOC adds another layer of flexibility to the microgrid. Operating in both fuel cell and electrolyzer modes, the RSOC can either generate electricity from hydrogen or produce hydrogen using electricity, depending on the operational needs. This dual functionality enables effective energy conversion and storage, further enhancing the microgrid's efficiency and resilience.

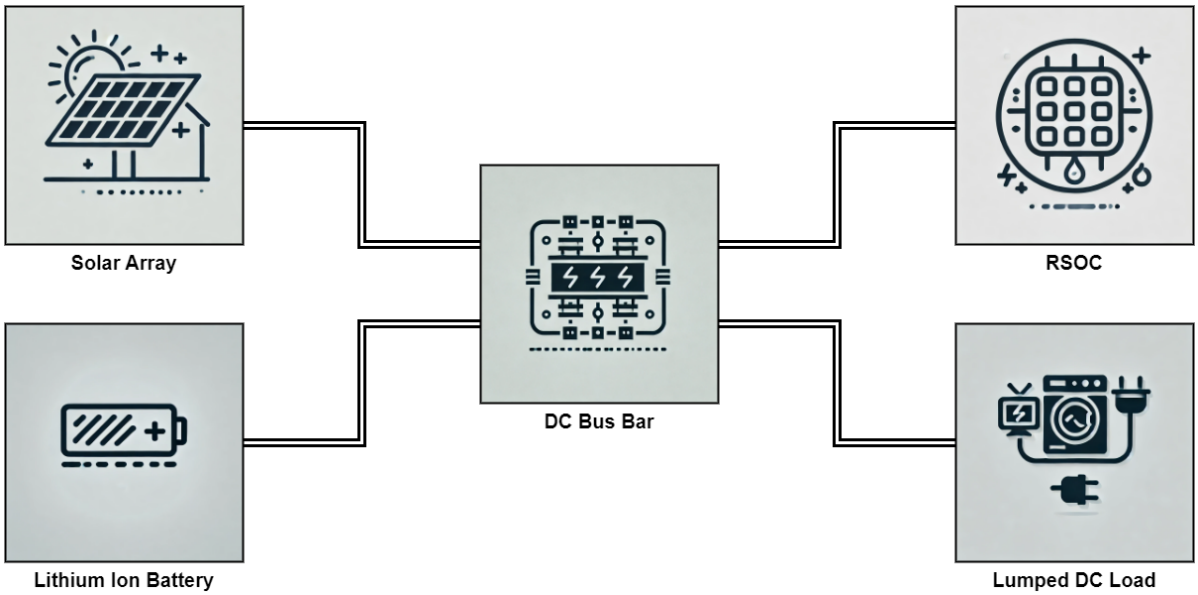

Figure 5.1: Simpliefied Microgrid Scheme

The DC load in the microgrid represents actual power consumption patterns, ensuring that the system is tested under realistic conditions. The supervisory control system is essential for managing the operation of all components. By continuously monitoring key parameters such as DC bus voltage, SoC, SoH, and solar irradiance, the control system dynamically adjusts the operational modes of the PV array, battery, and RSOC to ensure optimal performance and stability of the microgrid.

The microgrid configuration used here is an active topology, which means that it actively manages the flow of energy between its various components to optimize performance and maintain stability. This approach allows for real-time adjustments and responses to changing conditions, enhancing the overall reliability and efficiency of the system.

Overall, the integration of these components into a single microgrid system, as depicted in Figure 5.2, demonstrates a well-coordinated approach to managing renewable energy resources, storage solutions, and load demands, ensuring a reliable and efficient power supply.

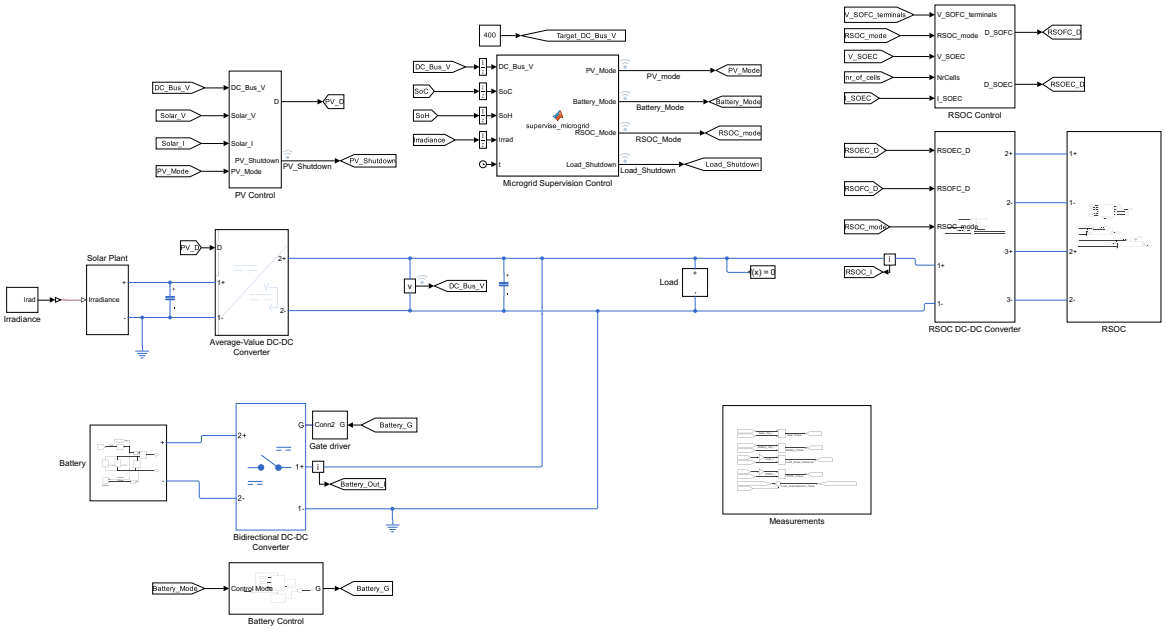

Figure 5.2: Microgrid Configuration

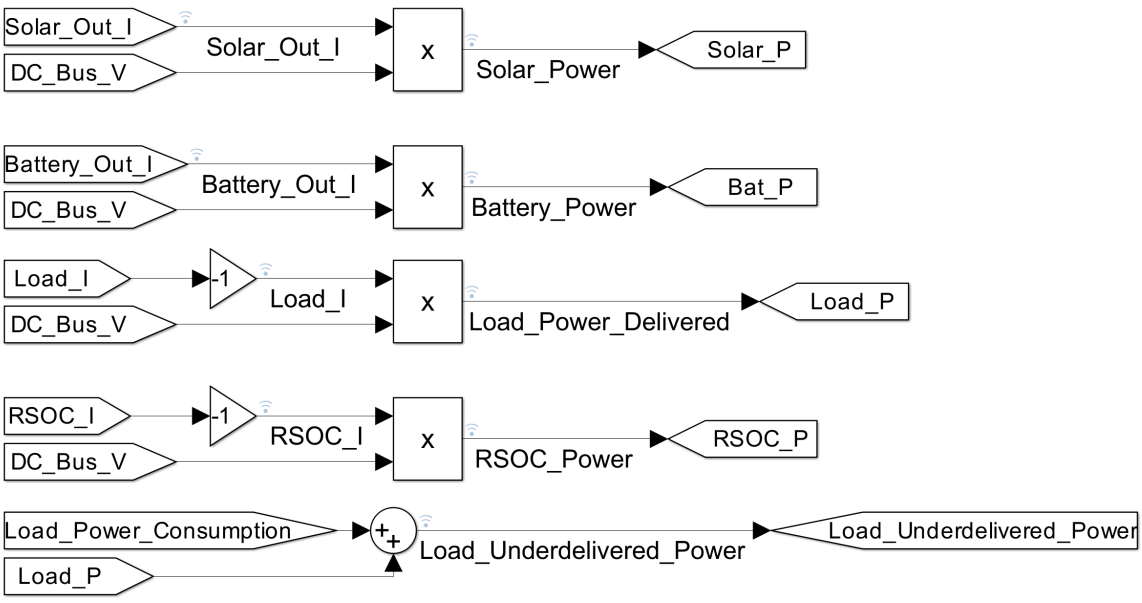

Figure 5.3: Power Measurements in the Microgrid

There is also a block depicted in Figure 5.3, where most of the measurements are aggregated. These

measurements mostly allow to track currents and power flows in the system.

5.2. Microgrid Control System

The control system for the microgrid is crucial for maintaining stability and efficient operation. The supervision control function, implemented in MATLAB, manages the modes of the PV array, battery, RSOC, and load shutdown based on input signals. The control logic is designed to ensure the microgrid operates within predefined thresholds and adapts to changing conditions. The supervisory control function determines the operational modes of the microgrid components based on predefined thresholds and current state measurements. The control strategy ensures that the DC bus voltage remains stable, the battery's state of charge is maintained within safe limits, and the RSOC operates efficiently. Load shutdown is initiated if the DC bus voltage exceeds critical thresholds for an extended period. The function dynamically adjusts the PV array mode between isolation, MPPT, and constant voltage, and the battery mode between controlling the DC bus voltage and being off. The RSOC switches between SOFC, SOEC, and off modes based on solar irradiance, battery state of charge, and DC bus voltage.

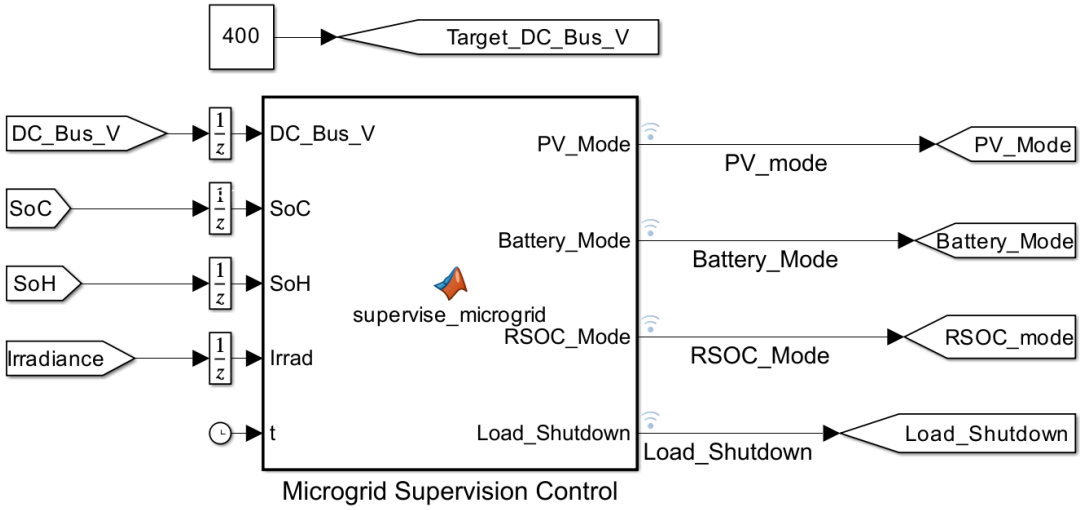

Figure 5.4: Microgrid Supervision Control

The control logic continuously monitors key parameters, including the DC Bus Voltage (DC_Bus_V), State of Charge (SoC) of the battery, State of Hydrogen (SoH), solar irradiance (Irrad), and the current time (t). These parameters are critical in determining the appropriate operational modes for each component.

The operational modes for each component are determined as follows:

- The PV Mode can be isolate (100), MPPT (010), or constant voltage (001).
- The Battery Mode can be control DC (10) or battery off (01).
- The RSOC Mode can be SOFC (0), SOEC (1), or turned off (-1).
- Load Shutdown indicates whether to shut down the load (1) or maintain normal operation (0).

Several predefined threshold values guide the control logic. The DC Bus Voltage goal is set at a nominal value of 400V, with lower and upper bounds defined at 380V (5% below nominal) and 420V (5% above nominal) respectively. The voltage level of 380V is more commonly used as a DC bus voltage, although 400V is also used [189]. Critical shutdown thresholds are established at 320V (20% below nominal) and 480V (20% above nominal). The State of Charge (SoC) thresholds for the battery include a low threshold at 20%, a very low threshold at 5%, and a mid-level threshold at 50%. Solar irradiance thresholds are set with a lower bound at 15 W/m² and an upper bound at 200 W/m². The State of

Hydrogen (SoH) has a very low threshold set at 10%. Additionally, an allowed transient duration of 20 seconds is defined to manage transient conditions, meaning the DC bus voltage can be in overvoltage or undervoltage conditions (below 320V or above 480V) for up to 20 seconds.

Persistent variables are used within the control function to track states and transitions. These include the current state of load shutdown (load_shutdown_state), the time duration below critical voltage thresholds (time_below_threshold), the last operational mode of the PV array (previous_PV_mode), the last operational mode of the battery (previous_battery_mode), the time of the last transition for battery mode (battery_transition_time), the start time for stability check (stable_start_time), a flag indicating if the voltage is stabilized by the battery (DC_Bus_Voltage_stabilized_by_battery), the last operational mode of the RSOC (previous_RSOC_mode), the time of the last transition for solar control (solar_transition_time), the start time for checking that PV array can stabilize the DC bus voltage (solar_stable_start_time), and a flag indicating if the voltage is stabilized by the solar array (DC_Bus _Voltage_stabilized_by_solar).

The load shutdown control ensures that the load is turned off if the DC bus voltage goes beyond critical thresholds for more than the allowed transient duration. It maintains normal operation when the voltage is within safe bounds. Battery mode control decides whether the battery should control the DC bus voltage or be turned off based on the DC bus voltage and the state of charge. It also considers whether the voltage has been stabilized by solar input or battery input. PV mode control determines the operational mode of the PV array based on the solar irradiance and battery state of charge. It switches between isolate, MPPT, and constant voltage modes to ensure optimal performance. RSOC mode control decides the operational mode of the RSOC based on solar irradiance, state of charge, and DC bus voltage. It switches between SOFC, SOEC, and off modes to manage energy conversion and storage efficiently.

The supervisory control system, as illustrated in Figure 5.4, integrates all these elements to ensure the microgrid operates within safe and efficient bounds. The control logic of the microgrid is shown below:

```
function [PV_Mode, Battery_Mode, RSOC_Mode, Load_Shutdown] = supervise_microgrid(DC_Bus_V,
    SoC, SoH, Irrad, t)
    % This function sets the PV_Mode, Battery_Mode, RSOC_Mode, and Load_Shutdown based on
        input signals.
    % Inputs:
    %   DC_Bus_V - Voltage of the DC Bus
    %   SoC - State of Charge of the battery
    %   SoH - State of Hydrogen of the system
    %   Irrad - Solar irradiance
    % Outputs:
    %   PV_Mode - a 3-element vector specifying the PV mode (100 for isolate, 010 for MPPT,
        001 for Constant Voltage)
    %   Battery_Mode - a 2-element vector specifying the Battery mode (10 for Control DC, 01
        for Battery Off)
    %   RSOC_Mode - a scalar specifying the RSOC mode (0 for SOFC, 1 for SOEC, -1 for Turned
        Off)
    %   Load_Shutdown - a scalar specifying whether to shut down the load (1 for shutdown, 0
        for normal operation)

    % Define threshold values for conditions
    DC_Bus_V_Goal = 400;               % Goal value for DC Bus Voltage
    DC_Bus_V_Low = 0.95 * DC_Bus_V_Goal;   % Lower bound for DC Bus Voltage
    DC_Bus_V_High = 1.05 * DC_Bus_V_Goal;  % Upper bound for DC Bus Voltage
    DC_Bus_V_Shutdown_Low = 0.8 * DC_Bus_V_Goal;  % Lower bound for shutdown
    DC_Bus_V_Shutdown_High = 1.2 * DC_Bus_V_Goal; % Upper bound for shutdown
    SoC_Threshold_Low = 20;            % Lower threshold for State of Charge
    SoC_Threshold_VeryLow = 5;         % Very low threshold for State of Charge
    SoC_Threshold_Mid = 50;            % Middle threshold for State of Charge
    Irrad_Threshold_Low = 15;          % Lower threshold for Solar Irradiance to turn off
        solar panels
    Irrad_Threshold_High = 200;        % Higher threshold for Solar Irradiance to turn on
        SOEC
    SoH_Threshold_Low = 10;            % Very low threshold for State of Hydrogen
    Allowed_Transient_Duration = 20;   % Duration threshold for shutdown in seconds

    % Persistent variables to track the load shutdown state and time below threshold
```

```
persistent load_shutdown_state time_below_threshold last_time previous_PV_mode
    previous_battery_mode battery_transition_time stable_start_time
    DC_Bus_Voltage_stabilized_by_battery previous_RSOC_mode solar_transition_time
    solar_stable_start_time DC_Bus_Voltage_stabilized_by_solar;
if isempty(load_shutdown_state)
    load_shutdown_state = 0; % Initialize to normal operation
    time_below_threshold = 0; % Initialize time below threshold
    last_time = t; % Initialize last time
    previous_PV_mode = [1 0 0];
    previous_battery_mode = [1 0];
    battery_transition_time = 0; % Initialize to no transition
    stable_start_time = 0; % Initialize stability start time
    DC_Bus_Voltage_stabilized_by_battery = 0; % Initialize stabilized flag
    previous_RSOC_mode = -1; % Initialize RSOC mode at the beginning of simulation
    solar_transition_time = 0; % Initialize to no transition for solar
    solar_stable_start_time = 0; % Initialize solar stability start time
    DC_Bus_Voltage_stabilized_by_solar = 0; % Initialize solar stabilized flag
end

% Update time_below_threshold
if DC_Bus_V < DC_Bus_V_Shutdown_Low || DC_Bus_V > DC_Bus_V_Shutdown_High
    time_below_threshold = time_below_threshold + (t - last_time);
else
    time_below_threshold = 0; % Reset if voltage is above threshold
end

last_time = t; % Update last time

% Determine Load_Shutdown
if time_below_threshold >= Allowed_Transient_Duration
    Load_Shutdown = 1; % Shut down the load
    load_shutdown_state = 1; % Update persistent state
elseif DC_Bus_V >= DC_Bus_V_Low && DC_Bus_V <= DC_Bus_V_High
    Load_Shutdown = 0; % Normal operation
    load_shutdown_state = 0; % Update persistent state
else
    Load_Shutdown = load_shutdown_state; % Keep previous state
end

% Determine Battery_Mode
if (DC_Bus_V < DC_Bus_V_Low && previous_battery_mode(1) == 0 || DC_Bus_V > DC_Bus_V_High
    && previous_battery_mode(1) == 0) && DC_Bus_Voltage_stabilized_by_solar == 1 && (SoC
    > 95 || SoC < 3)
    Battery_Mode = [0 1]; % Battery Off
elseif previous_battery_mode(1) == 1 && DC_Bus_Voltage_stabilized_by_battery == 0 ||
    DC_Bus_V < DC_Bus_V_Low && previous_battery_mode(1) == 0 || DC_Bus_V > DC_Bus_V_High
    && previous_battery_mode(1) == 0
    Battery_Mode = [1 0]; % Control DC
elseif SoC > 95 || SoC < 3
    Battery_Mode = [0 1]; % Battery Off
else
    Battery_Mode = [1 0]; % Control DC
end

% DC Bus Voltage stability control
% Check for transition from battery off to battery controlling DC voltage
if previous_battery_mode(1) == 0 && Battery_Mode(1) == 1
    battery_transition_time = t; % Record transition time
    stable_start_time = 0; % Reset stability start time on transition
    DC_Bus_Voltage_stabilized_by_battery = 0; % Reset stabilized flag on transition
end

% Check if DC bus voltage is stable
if DC_Bus_V >= 395 && DC_Bus_V <= 405
    if stable_start_time == 0
        stable_start_time = t; % Record start time of stability
    elseif t - stable_start_time >= 245 && t - battery_transition_time >= 245
        DC_Bus_Voltage_stabilized_by_battery = 1; % Set stabilized flag after 245 seconds
            of stability
    end
else
```

```
        stable_start_time = 0; % Reset stability start time if voltage is not stable
        DC_Bus_Voltage_stabilized_by_battery = 0; % Reset stabilized flag if voltage is not
            stable
    end
    previous_battery_mode = Battery_Mode;

    % DC Bus Voltage stability control by solar
    % Check for transition from battery controlling DC to battery off and solar controlling
        DC voltage
    if previous_battery_mode(1) == 1 && Battery_Mode(1) == 0
        solar_transition_time = t; % Record transition time
        solar_stable_start_time = 0; % Reset stability start time on transition
        DC_Bus_Voltage_stabilized_by_solar = 0; % Reset stabilized flag on transition
    end

    % Check if DC bus voltage is stable by solar
    if DC_Bus_V >= 395 && DC_Bus_V <= 405
        if solar_stable_start_time == 0
            solar_stable_start_time = t; % Record start time of stability
        elseif t - solar_stable_start_time >= 15 && t - solar_transition_time >= 15
            DC_Bus_Voltage_stabilized_by_solar = 1; % Set stabilized flag after 15 seconds of
                stability
        end
    else
        solar_stable_start_time = 0; % Reset stability start time if voltage is not stable
        DC_Bus_Voltage_stabilized_by_solar = 0; % Reset stabilized flag if voltage is not
            stable
    end

    % Determine PV_Mode
    if Irrad < Irrad_Threshold_Low && previous_PV_mode(2) == 1 || Irrad < Irrad_Threshold_Low
         && previous_PV_mode(3) == 1 || Irrad < (Irrad_Threshold_Low + 10) &&
        previous_PV_mode(1) == 1
        PV_Mode = [1 0 0]; % Isolate
    elseif Battery_Mode(1) == 0 % Battery off
        PV_Mode = [0 0 1]; % Constant Voltage
    elseif Battery_Mode(1) == 1 % Battery controls DC bus
        PV_Mode = [0 1 0]; % MPPT
    else
        PV_Mode = [0 1 0]; % MPPT
    end
    previous_PV_mode = PV_Mode;

    % Determine RSOC_Mode
    if Battery_Mode(1) == 1 && DC_Bus_V > DC_Bus_V_High && previous_RSOC_mode == 0 ||
        Battery_Mode(1) == 1 && DC_Bus_V < DC_Bus_V_Low && previous_RSOC_mode == 1
        RSOC_Mode = -1; % Turned Off
    elseif Irrad < Irrad_Threshold_Low || SoC < SoC_Threshold_Low  || (Battery_Mode(1) == 1
        && PV_Mode(2) == 1 && DC_Bus_V < DC_Bus_V_Low)
        RSOC_Mode = 0; % SOFC (Fuel Cell Mode)
    elseif (Irrad > Irrad_Threshold_High || SoC > SoC_Threshold_Mid || (DC_Bus_V >
        DC_Bus_V_High)) && DC_Bus_V > DC_Bus_V_Low
        RSOC_Mode = 1; % SOEC (Electrolyzer Mode)
    else
        RSOC_Mode = -1; % Turned Off
    end

    % Allow hydrogen system to discharge to 0 SoH if necessary
    if SoC < SoC_Threshold_VeryLow || (DC_Bus_V < DC_Bus_V_Low && SoH < SoH_Threshold_Low &&
        SoC < SoC_Threshold_Low)
        RSOC_Mode = 0; % SOFC (Fuel Cell Mode) - Allow discharge to 0
    end
    previous_RSOC_mode = RSOC_Mode;
end
```

Listing 5.1: Supervise Microgrid Function

5.3. Summary

This chapter explored the integration and control of a microgrid system consisting of a solar PV array, lithium-ion battery system, reversible solid oxide cell (RSOC), and a DC load. These components are interconnected via a 400V DC bus, and the system is simulated over a 24-hour period using millisecond resolution to enhance control accuracy and computational efficiency.

The hierarchical and rule-based control system is designed to maintain stability and efficiency within the microgrid. By continuously monitoring key parameters such as DC bus voltage, battery state of charge (SoC), state of hydrogen (SoH), and solar irradiance, the supervisory control function ensures optimal operation. The control logic dynamically adjusts the operational modes of the PV array, battery, RSOC, and load shutdown based on predefined thresholds and real-time measurements.

Several predefined threshold values guide the control logic, ensuring that the microgrid operates within safe and efficient bounds. The goal for the DC bus voltage is set at a nominal value of 400V and an acceptable fluctuation range of 5% above and below the nominal value (380V to 420V). Critical shutdown thresholds are established at 320V and 480V, corresponding to a 20% margin. The allowed transient duration of 20 seconds for the DC bus voltage to be in overvoltage or undervoltage conditions ensures that the system can handle short-term deviations without immediate shutdown.

Persistent variables within the control function track states and transitions, contributing to the robust performance of the microgrid. By managing the dynamic behavior of the PV array, battery, RSOC, and load, the supervisory control system effectively stabilizes the DC bus voltage, optimizes energy storage and conversion, and ensures reliable power delivery to the load.

The integration and control strategies presented in this chapter provide a foundation for the efficient and reliable operation of microgrids with reversible solid oxide cells.

6

Results and Discussion

This chapter explores the microgrid system's dynamic performance and energy management strategies during two contrasting 24-hour periods: a high power demand day in March and a typical day in July. The analysis highlights the system's adaptability to changing solar irradiance and varying load demands through effective operational mode transitions. Key transitions during peak solar hours and high load periods showcase the system's ability to maintain voltage and power stability. Furthermore, the study suggests improvements in control strategies, including the implementation of rule-based fuzzy logic and model predictive control based on weather forecasts, to optimize system efficiency and reliability.

6.1. A Case Study of a Day in March

6.1.1. System Dynamics and Mode Transitions

In Figure 6.1, the different modes of the microgrid, their transitions, and other influencing parameters such as voltage, load profile, state of charge, and irradiance are observable. At the outset of the simulation, the photovoltaic (PV) system is in isolation mode, the lithium-ion battery is regulating the DC bus voltage, and the reversible solid oxide cell (RSOC) is initially in Off mode but immediately transitions to Solid Oxide Fuel Cell (SOFC) mode. The first significant transition occurs at approximately 6 AM when the solar panel switches from isolation mode to Maximum Power Point Tracking (MPPT) mode due to increasing solar irradiation surpassing the lower threshold.

The second major transition happens shortly after 9 AM when state of charge(SoC) surpasses 20%, which allows the RSOC to attempt to switch from SOFC to Solid Oxide Electrolyzer Cell (SOEC) mode. However, this transition is not instantaneous; it requires the RSOC to spend 180 seconds in transition mode before fully adopting the SOEC mode. Subsequently, just before 1 PM, the SoC of the battery reaches 95%, prompting the battery to transition to Off mode and the PV system to assume control of the DC bus. At this moment, an excess of energy in the system (visible in Figure 6.2 from PV array power plot) causes a brief voltage spike to 407 V, necessitating a swift return to battery DC bus management and PV MPPT control. Consequently, the battery continues to charge for an additional 10 minutes, reaching approximately 98% SoC, after which the system successfully transitions to a state where the solar array regulates the DC bus voltage, and the battery is turned off.

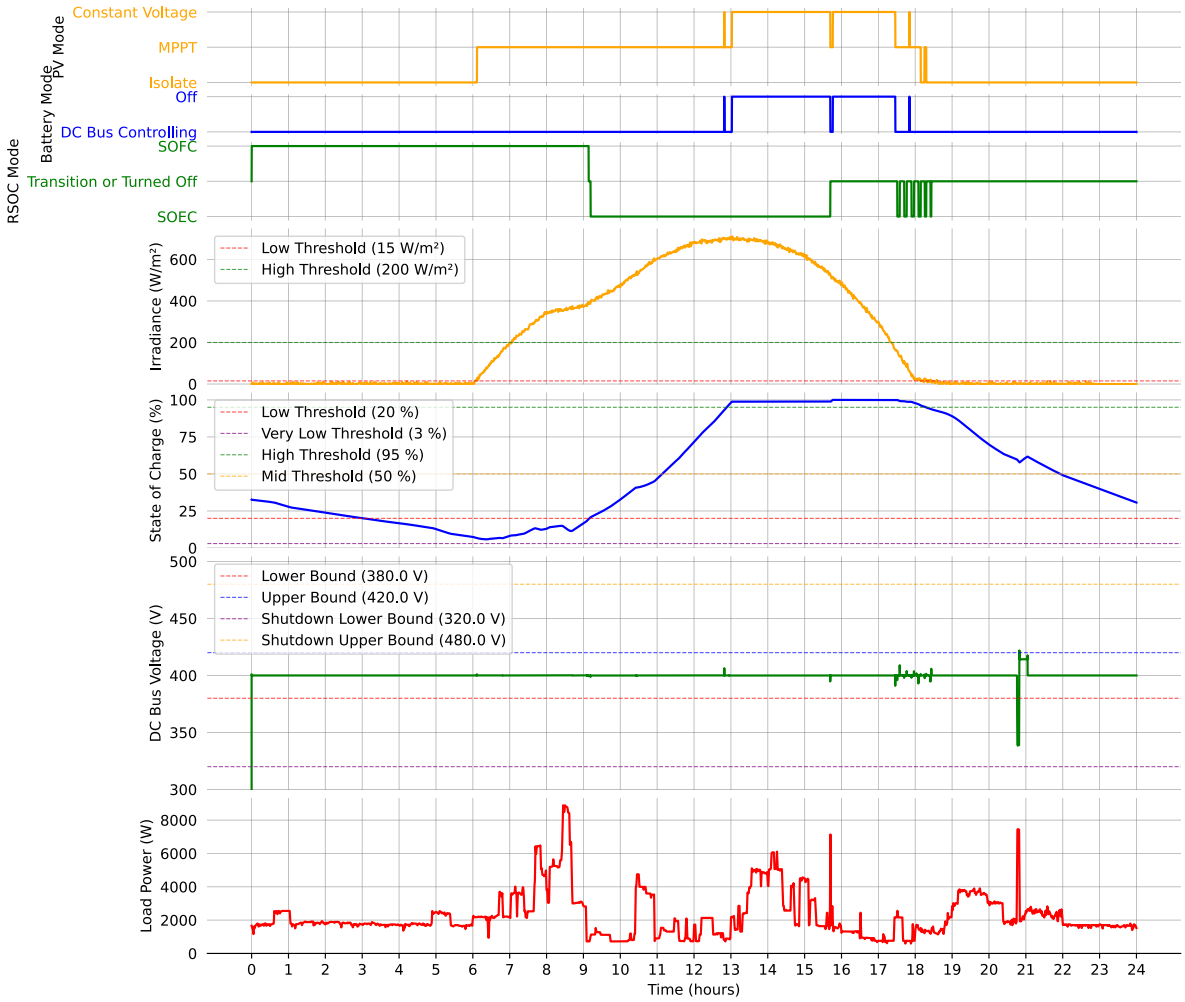

Figure 6.1: Dynamics of the microgrid

At around 15:40, a substantial and rapid increase in load demand causes the solar panel to lose control over the DC bus voltage, resulting in a minor voltage drop of about 5 volts below the nominal 400 V. This triggers the system to transition to battery management of the DC bus and the solar array to revert to MPPT mode. Simultaneously, the RSOC transitions to Off mode. The battery continues to charge and eventually reaches 100% SoC. Once the battery is fully charged and turns off again, the solar panel regains the capability to manage the load, and with the RSOC off, maintaining the DC bus voltage becomes more manageable.

At 17:30 PM, the solar irradiance decreases to a level where the PV array cannot generate sufficient energy to manage the load. Consequently, the DC bus voltage drops, prompting the battery to switch to DC bus voltage control mode and the solar array to MPPT mode. This operational mode persists for approximately an hour, albeit with voltage fluctuations induced by the RSOC's transitions between SOEC mode and Off mode. Although this RSOC behavior is not optimal, it is not detrimental and has been marked for future improvement, possibly through a modified control strategy such as rule-based fuzzy logic control.

Around 18:30, the oscillations in RSOC modes subside, with the RSOC remaining in Off mode. Just prior to this, the solar array transitions from MPPT to isolation mode due to insufficient solar irradiance. The simulation continues with the PV in isolation mode, RSOC in Off mode, and the battery in DC control mode until the end of the simulation at midnight. Notably, around 9 PM, a significant fluctuation occurs due to a large peak in load power consumption. This is the sole instance where the voltage exceeds the normal operating tolerance margin of $\pm 5\%$, but it does not drop below the load shutdown threshold of 320 V. Initially, the setup allowed the voltage to drop below this threshold, leading to load

shutdowns. However, after careful tuning of the PID voltage and current control loops of the battery management converter, a much more stable behavior was achieved, ensuring reliable load operation even under the most challenging conditions. It is also worth noting that the load profile utilized in this simulation corresponds to the most demanding day from a year of Kaya Imani load simulation.

6.1.2. Power Balance

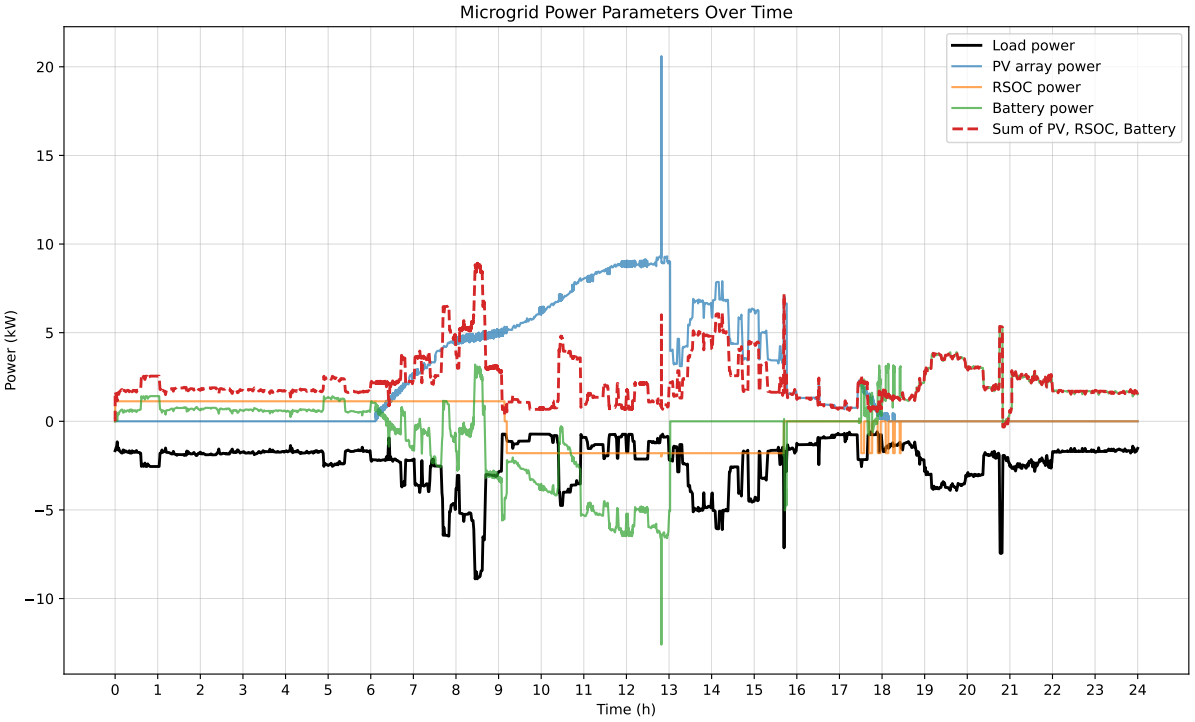

Figure 6.2: Microgrid Power Parameters Over Time

Figure 6.2 provides a comprehensive visualization of the different power components within a microgrid system over a period of 24 hours. The plot includes four key power parameters: Load Power, PV Array Power, RSOC Power, and Battery Power. Load Power, represented by a solid black line, indicates the total power consumption of the microgrid over time. The load power values are plotted as negative to visually represent consumption, distinguishing it from power generation sources. The PV Array Power, shown as a blue line, varies based on solar irradiance and other environmental factors. All the other components are influenced solely by the operating modes of the microgrid and its internal conditions, such as the voltage at the DC bus.

The RSOC and battery power lines indicate the times when these systems are either charging (negative values) or discharging (positive values).

Additionally, the plot includes a parameter called the Sum of PV, RSOC, and Battery Power, represented by a dashed red line. This parameter is the sum of the power contributions from the PV array, RSOC, and battery system. This cumulative power value helps to visualize how these sources collectively meet the load power demand. The plot visually demonstrates how the sum of the power generated by the PV array, RSOC, and battery system corresponds to the load power demand. Ideally, the sum should match the load power to ensure the microgrid's power balance. The plot clearly shows that the dashed red line closely mirrors the solid black line, indicating effective load following and stable grid performance.

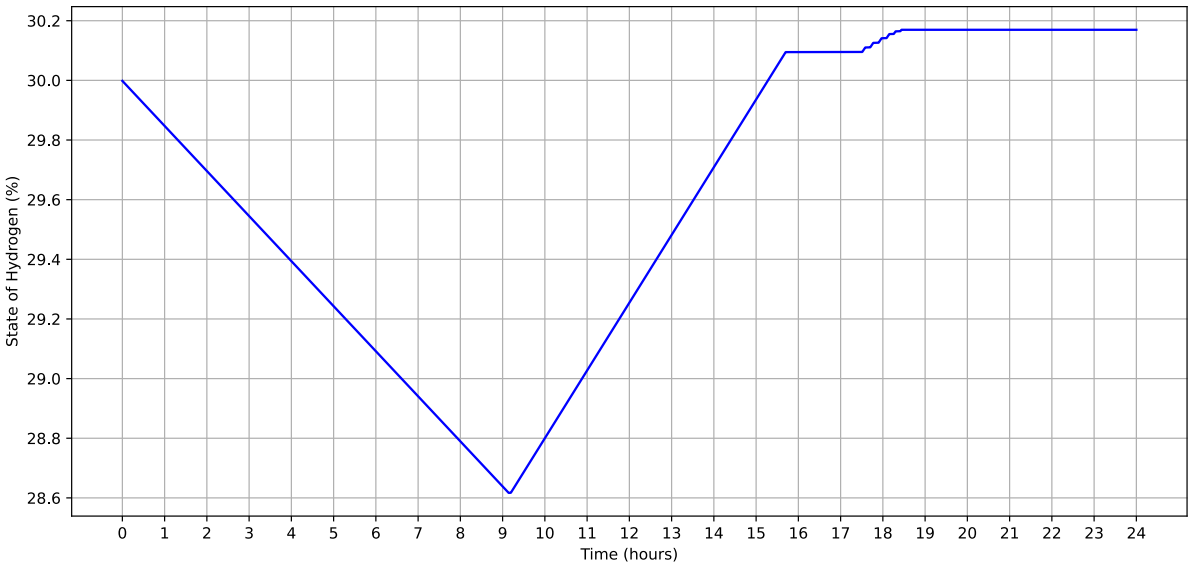

Figure 6.3: State of Hydrogen

6.1.3. Energy Balance

State of Hydrogen

The State of Hydrogen (SoH) was 30.00% at the beginning of the day and 30.17% at the end of the day. This indicates that the system was able to accumulate the extra energy obtained from the solar panels during the day in hydrogen.

To calculate the energy from hydrogen, the total mass of hydrogen was first converted to moles. Given the total mass of the hydrogen tank is 23550 grams and the molar mass of hydrogen (H_2) is 2.016 g/mol, the total moles of hydrogen is given by

$$\text{Total moles of hydrogen} = \frac{23550 \text{ g}}{2.016 \text{ g/mol}} = \text{ moles.} \tag{6.1}$$

Next, the initial and final energy contents were calculated. The initial energy content, with a SoH of 30%, is given by:

$$\text{Initial energy content} = 0.30 \times 11681.5 \text{ moles} \times 241.8 \text{ kJ/mol} = 847376 \text{ kJ.} \tag{6.2}$$

Similarly, the final energy content, with a SoH of 30.17%, is calculated as:

$$\text{Final energy content} = 0.3017 \times 11681.5 \text{ moles} \times 241.8 \text{ kJ/mol} = 852178 \text{ kJ.} \tag{6.3}$$

The net energy gain is the difference between the final and initial energy contents:

$$\text{Net energy gain} = 852178 \text{ kJ} - 847376 \text{ kJ} = 4802 \text{ kJ.} \tag{6.4}$$

Considering the efficiency of the fuel cell, which is 73.35%, the usable energy is:

$$\text{Usable energy} = 4802 \text{ kJ} \times 0.7335 = 3531.87 \text{ kJ.} \tag{6.5}$$

To better understand the energy metrics, the usable energy was converted from kJ to Wh:

$$\text{Usable energy} = \frac{3531.87 \text{ kJ}}{3.6 \text{ kJ/Wh}} = 981 \text{ Wh.} \tag{6.6}$$

State of Charge

The State of Charge (SoC) started at 32.64% and decreased to 30.68% by the end of the day.

To calculate the energy from the battery, the battery capacity was first converted to energy. Given the battery capacity is 378 A*h (2 packs of 189 A*h) and the nominal voltage is 51.8 V, the total energy capacity is:

$$\text{Total energy capacity} = 378 \text{ A*h} \times 51.8 \text{ V} = 19580.4 \text{ Wh}. \tag{6.7}$$

Next, the initial and final energy contents were calculated. The initial energy content, with a SoC of 32.64%, is given by:

$$\text{Initial energy content} = 0.3264 \times 19580.4 \text{ Wh} = 6391.04 \text{ Wh}. \tag{6.8}$$

Similarly, the final energy content, with a SoC of 30.68%, is calculated as:

$$\text{Final energy content} = 0.3068 \times 19580.4 \text{ Wh} = 6007.27 \text{ Wh}. \tag{6.9}$$

The net energy loss is the difference between the initial and final energy contents:

$$\text{Net energy loss} = 6391.04 \text{ Wh} - 6007.27 \text{ Wh} = 384 \text{ Wh}. \tag{6.10}$$

Overall Net Energy Change

By comparing the energy gained from hydrogen and the energy lost from the battery, the overall net energy change was determined. The energy gained from hydrogen is 2986.74 kJ and the energy lost from the battery is 1377.9 kJ. Thus, the net energy change is:

$$\text{Net energy change} = 981 \text{ Wh} - 384 \text{ Wh} = 597 \text{ Wh}. \tag{6.11}$$

During the course of the day, the system experienced a net energy gain, with an overall surplus of 597 Wh. While this is a positive outcome, the gain is relatively modest. This can be attributed to the combination of high solar irradiance in March, typical for Msambweni, Kenya, and the choice of a particularly demanding and dynamic load profile for the simulation. The high energy demand of the load profile offsets some of the potential gains from the abundant solar energy, resulting in a net gain that, although expected in March, is not as substantial as it might be under less demanding conditions.

6.2. A Case Study of a Day in July

6.2.1. System Dynamics and Mode Transitions

Figure 6.4 illustrates the various operational modes of the microgrid, the transitions between these modes, and the influencing parameters, including voltage, load profile, state of charge (SoC), and irradiance. At the start of the simulation, the photovoltaic (PV) system operates in isolation mode, the lithium-ion battery manages the DC bus voltage, and the reversible solid oxide cell (RSOC) is either in transition or turned off, soon transitioning to Solid Oxide Fuel Cell (SOFC) mode.

The first notable transition occurs at approximately 6:30 AM, when the PV system shifts from isolation mode to Maximum Power Point Tracking (MPPT) mode due to an increase in solar irradiance exceeding a specified lower threshold.

Around 9:25 AM, the RSOC transitions from SOFC mode to off mode, and by 9:32 AM, it switches to Solid Oxide Electrolyzer Cell (SOEC) mode. Although the RSOC typically requires a minimum of 3 minutes in transition mode before fully adopting SOEC mode, in this instance, the transition was more rapid. At approximately 5:30 PM, a significant and rapid increase in load demand causes a drop in DC bus voltage to nearly 380 V, prompting the RSOC to revert to off mode. This leads to a rapid decrease in overall load power demand, resulting in an increase in DC bus voltage to just over 420 V. The system subsequently reaches equilibrium swiftly. Around 6:00 PM, the solar irradiance falls below the lower threshold of 15 $\frac{W}{m^2}$, causing the PV system to revert to isolation mode. Simultaneously, the RSOC shifts to SOFC mode to supply additional power to the DC bus.

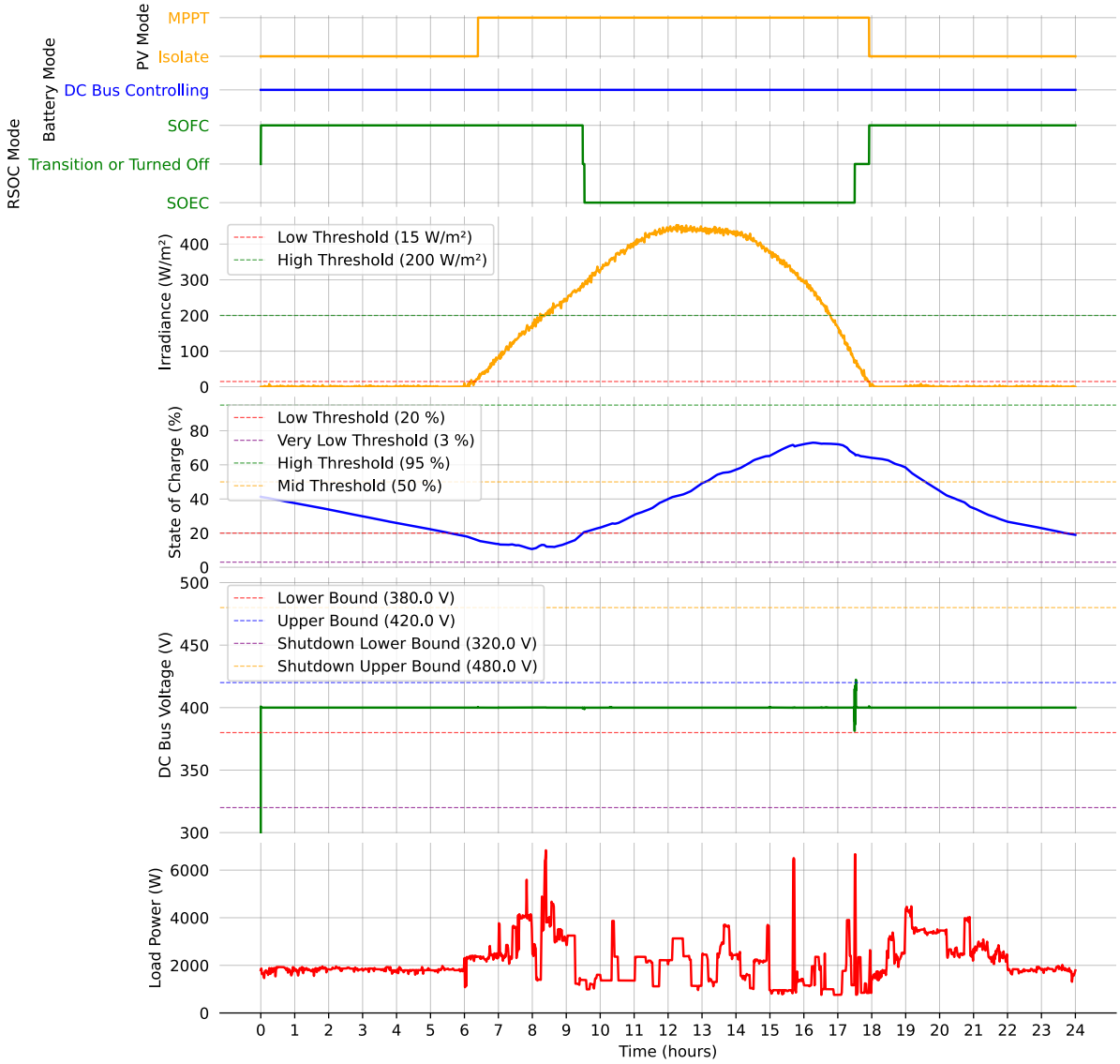

Figure 6.4: Dynamics of the microgrid for a day in July

The simulation proceeds with the PV in isolation mode, RSOC in SOFC mode, and the battery controlling the DC bus voltage until the end of the simulation at midnight. The load profile used in this simulation corresponds to a typical July day from the Kaya Imani year-long load simulation dataset. The solar irradiance data is based on the average July irradiance profile for the specified location[185].

6.2.2. Power Balance

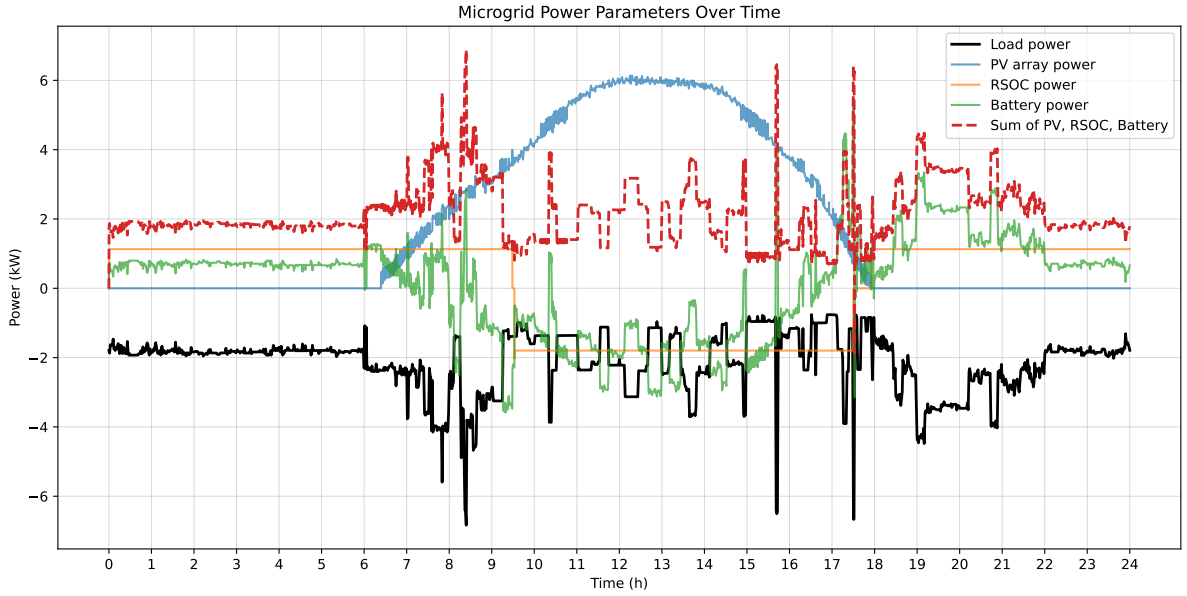

Figure 6.5: Microgrid Power Parameters Over Time

Figure 6.5 showcases the power dynamics within a microgrid system over a full day. The graph highlights four key power indicators: Load Power, PV Array Power, RSOC Power, and Battery Power. Load Power is depicted by a solid black line, signifying the microgrid's total energy consumption, and is presented as negative values to distinguish it from power generation. The PV Array Power, shown in blue, varies according to solar irradiance and environmental conditions. The RSOC and Battery Power lines reflect the charging (negative) and discharging (positive) states of these systems.

A dashed red line represents the Sum of PV, RSOC, and Battery Power, illustrating the combined power output from the PV array, RSOC, and battery system. This cumulative power line helps visualize how the collective power sources meet the microgrid's load demand. The graph reveals that the dashed red line closely follows the solid black line, indicating that the power supply from the PV array, RSOC, and battery system is well-matched to the microgrid's consumption needs. This alignment demonstrates effective load balancing and stable operation of the microgrid system throughout the 24-hour period. Moreover, the alignment here is even better than in the previous case, which depicted more challenging operational conditions. This improvement is logical as the current scenario represents more stable and predictable conditions, allowing for even better synchronization between power generation and consumption.

6.2.3. Energy Balance

Hydrogen Status

At the beginning of the day, the State of Hydrogen (SoH) was 30.00%, and it decreased slightly to 29.46% by the end of the day. This indicates that some of the stored hydrogen was utilized throughout the day to meet the energy demands.

To calculate the energy from hydrogen, the total mass of hydrogen was first converted to moles. With a total hydrogen tank mass of 23,550 grams and a molar mass of hydrogen (H_2) of 2.016 g/mol, the total moles of hydrogen are calculated as follows:

$$\text{Total moles of hydrogen} = \frac{23550 \text{ g}}{2.016 \text{ g/mol}} = 11681.5 \text{ moles}. \tag{6.12}$$

Next, the initial and final energy contents were calculated. The initial energy content, with an SoH of 30

$$\text{Initial energy content} = 0.30 \times 11681.5 \text{ moles} \times 241.8 \text{ kJ/mol} = 847376 \text{ kJ}. \tag{6.13}$$

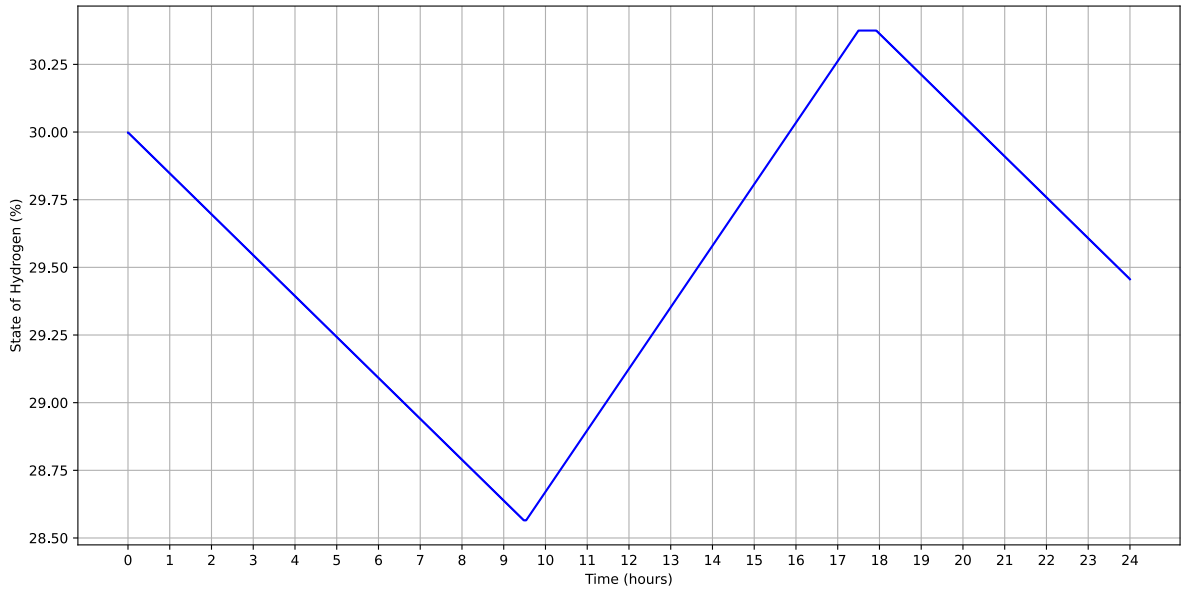

Figure 6.6: Hydrogen Status

The final energy content, with an SoH of 29.46

$$\text{Final energy content} = 0.2946 \times 11681.5 \text{ moles} \times 241.8 \text{ kJ/mol} = 832123 \text{ kJ}. \tag{6.14}$$

The net energy loss is the difference between the initial and final energy contents:

$$\text{Net energy loss} = 847376 \text{ kJ} - 832123 \text{ kJ} = 15253 \text{ kJ}. \tag{6.15}$$

Considering the efficiency of the fuel cell, which is 73.35%, the usable energy is:

$$\text{Usable energy loss} = 15253 \text{ kJ} \times 0.7335 = 11188 \text{ kJ}. \tag{6.16}$$

To better understand the energy metrics, the usable energy was converted from kJ to Wh:

$$\text{Usable energy loss} = \frac{11188 \text{ kJ}}{3.6 \text{ kJ/Wh}} = 3108 \text{ Wh}. \tag{6.17}$$

Battery Charge Status

The State of Charge (SoC) of the battery, extracted from the simulation data, started at 41.27% and decreased to 18.98% by the end of the day.

To calculate the energy stored in the battery, the battery capacity was first converted to energy. Given the battery capacity of 378 Ah (2 packs of 189 Ah each) and a nominal voltage of 51.8 V, the total energy capacity is:

$$\text{Total energy capacity} = 378 \text{ A*h} \times 51.8 \text{ V} = 19580.4 \text{ Wh}. \tag{6.18}$$

Next, the initial and final energy contents were calculated. The initial energy content, with a SoC of 41.27%, is:

$$\text{Initial energy content} = 0.4127 \times 19580.4 \text{ Wh} = 8080.83 \text{ Wh}. \tag{6.19}$$

The final energy content, with a SoC of 18.98%, is:

$$\text{Final energy content} = 0.1898 \times 19580.4 \text{ Wh} = 3716.36 \text{ Wh}. \tag{6.20}$$

The net energy loss is the difference between the initial and final energy contents:

$$\text{Net energy loss} = 8080.83 \text{ Wh} - 3716.36 \text{ Wh} = 4364.47 \text{ Wh}. \tag{6.21}$$

Overall Energy Balance

By comparing the energy lost from hydrogen and the energy lost from the battery, the overall net energy change was determined. The usable energy loss from hydrogen is 3108 Wh, while the energy loss from the battery is 4364 Wh. Thus, the net energy loss is:

$$\text{Net energy loss} = 3108 \text{ Wh} + 4364 \text{ Wh} = 7472 \text{ Wh}. \tag{6.22}$$

During the course of the day, the system experienced a net energy loss, resulting in an overall deficit of 7472 Wh. In July in Msambweni, Kenya the solar irradiation is the weakest compared to any other month. Hence, it is logical that to ride through this period with a solar array of this size it is necessary to have a comprehensive hydrogen energy storage.

6.3. Summary

The detailed examination of the microgrid system's performance across two distinct days, a demanding day in March and an ordinary day in July, provides comprehensive insights into the dynamic behavior and energy management strategies of the system.

During the hectic and high-demand day in March, characterized by great solar irradiation, the system effectively managed transitions between various operational modes, maintaining stability and efficiently managing voltage and power. Despite significant fluctuations and high load demands, the system demonstrated effective load-following capability and stable grid performance, achieving a small net energy gain of 597 Wh.

On the less challenging day in July, which represents an ordinary day in terms of load power demand and experiences the lowest solar irradiance of the year, the system also maintained stable operations with a close alignment between power generation and consumption. The PV system, RSOC, and battery collectively managed the DC bus voltage and load demands, ensuring reliable operation. However, due to lower solar irradiance the system relied more on stored hydrogen and battery energy and hence experienced a net energy loss of 7472 Wh.

Overall, the microgrid system demonstrated promising potential for stable and efficient energy management under varying conditions. The detailed insights into system dynamics, power balance, and energy balance provide valuable guidance for further optimization and development of control strategies, such as rule-based fuzzy logic. Furthermore, as a future development, the implementation of model predictive control based on weather forecasts could enhance system performance by preparing the most optimal levels of battery charge for the beginning and end of each day. This approach would help in achieving even greater efficiency and reliability in energy management.

7

Thesis Conclusion

This thesis has focused on the innovative integration of lithium-ion batteries and reversible solid oxide cells (RSOCs) as a novel energy storage solution within microgrids. The study explored the dynamic modeling and control strategies for this hybrid system using MATLAB/Simulink, addressing a gap in the existing literature. While most previous studies have concentrated on sizing, energy optimization, and the material science of solid oxide fuel cells (SOFCs), this research delved into the combination of RSOCs with lithium-ion batteries, examining their control and dynamics in a microgrid context.

7.1. Achieving the Overarching Aim

The primary aim of creating a stable standalone microgrid was successfully achieved. The integration of lithium-ion batteries and RSOCs leveraged their complementary characteristics to manage energy storage needs over different timescales. Lithium-ion batteries provided high power density and fast dynamic response, making them ideal for handling short-term power spikes and rapid fluctuations. They also managed mid-term storage requirements, providing a buffer for hours of energy supply during periods of intermittent renewable generation. Meanwhile, RSOCs offered a robust solution for long-term energy storage due to their high energy density and ability to efficiently convert hydrogen back to electricity. This hybrid approach not only enhanced the microgrid's ability to handle immediate power demands but also allowed for a smaller and more cost-effective RSOC system, optimizing long-term storage and maintaining overall system efficiency and reliability.

7.2. Hypothesis Validation

The hypothesis that integrating lithium-ion batteries and RSOCs within a standalone microgrid, coupled with MATLAB/Simulink for dynamic modeling and control strategy development, would result in an energy-efficient and reliable system was proven. The system adeptly managed energy needs across short-term, mid-term, and long-term timescales, ensuring stable and independent operation without relying on a traditional distribution network.

7.3. Scientific Novelty

The scientific novelty of this work lies in the integration and dynamic modeling of a microgrid that combines the high energy density of lithium-ion batteries with the extensive storage capacity of RSOCs. This hybrid storage architecture leverages the strengths of each technology while addressing their weaknesses: lithium-ion batteries provide rapid response and short-term power management, while RSOCs handle long-term energy storage with high efficiency and low self-discharge rates. The combination of these technologies addresses the variability of renewable energy sources and demand fluctuations, enhancing the performance and stability of the microgrid. Additionally, a detailed model of RSOCs was created from scratch based on commercially available cells, which represents a substantial achievement beyond the initial aims of this research. This microgrid model can serve as a solid foundation for further studies and development in the area of microgrid control and dynamics.

7.4. Confirmation of Research Technical Objectives

Objective 1: Creating a Detailed Load Profile

Methodology: Utilizing the open-source Python library RAMP, a detailed multi-energy load profile for the Kaya Imani Resort was generated. This involved systematic data collection and analysis to capture the resort's specific energy usage patterns and requirements. Multiple interviews with the resort owner helped clarify and integrate the consumption patterns of the resort residents along with the schedules for electrical devices.

Achievement: The detailed load profile served as a foundation for designing a microgrid that could meet real-world energy consumption patterns. It was a valuable asset for scientific research and provided critical data for the sizing of the microgrid components.

Objective 2: Developing and Sizing Microgrid Components

Methodology: Detailed models of the key components, including solar panels, RSOCs, lithium-ion batteries, and DC loads, were developed using MATLAB/Simulink. This involved simulating the physical characteristics of each component and selecting parameters based on the sizing requirements derived from the load profile.

Achievement: The developed models accurately represented the physical behavior of each component, ensuring optimal performance and reliability of the microgrid system.

Objective 3: Integrating Microgrid Component Models

Methodology: The individual component models were integrated into a comprehensive MATLAB/Simulink model to simulate dynamic interactions within the microgrid. Local controllers for each component were developed to simulate energy conversion, storage processes, and their interactions within the system.

Achievement: The integration focused on evaluating the system's performance in static states and during simple transitions, ensuring a realistic representation of the microgrid's behavior under common operational conditions.

Objective 4: Designing and Simulating Advanced Hierarchical Control Strategies

Methodology: Hierarchical rule-based control algorithms were implemented within Simulink. Each energy generation unit had its own local control, while an overarching control coordinated the units. Control actions were adjusted to maintain system stability, optimizing the levels of hydrogen and the state of charge of the batteries.

Achievement: The control strategies ensured stable operation even with minimal storage capacity, allowing efficient and reliable performance of the microgrid under hectic and challenging energy demands demonstrated for a period of 24 hours.

Objective 5: Theoretical Evaluation and Optimization of Microgrid Performance

Methodology: Simulations based on the most hectic day of the year in terms of load profile were performed to test the system for different transitions and realistically demonstrate its characteristics at its extremes. Results were analyzed to determine the effectiveness of control strategies and to propose improvements.

Achievement: The energy balance analysis indicated a net energy gain over the simulation period, underscoring the potential of combining lithium-ion batteries and RSOCs for efficient energy storage and management. The system maintained a positive energy balance, reflecting its resilience and capability to handle dynamic and demanding conditions.

7.5. Future Work

While this thesis has successfully demonstrated the potential of the combined lithium-ion battery and RSOC microgrid, further research is needed to refine and expand upon these findings. Future work could focus on:

- Developing and testing more advanced control strategies, such as fuzzy logic or machine learning-based approaches as well as model predictive control based on weather forecasts, to further enhance system stability and efficiency.
- Conducting experimental validation of the developed models and control strategies in real-world scenarios to verify their practicality and effectiveness.
- Exploring the integration of additional renewable energy sources and storage technologies to diversify and improve the resilience of the microgrid.
- Investigating the economic aspects and scalability of the proposed microgrid solution as well as developing more advanced microgrid component sizing algorithms.
- Adding dynamic thermal management of RSOCs to the microgrid simulation systems, which is an interesting topic for research in the area of combined heat and power.

7.6. Conclusion

This thesis has advanced the field of microgrid technology by successfully modeling a standalone microgrid using a novel combination of lithium-ion batteries and reversible solid oxide cells (RSOCs). This innovative approach provides a robust solution for energy storage and management. The dynamic modeling and control strategies developed through MATLAB/Simulink have shown promising results in managing energy demands and ensuring grid stability. The simulations have demonstrated the system's effectiveness in maintaining efficiency and stability even under most challenging conditions, thereby validating the hypothesis and achieving the research objectives. The insights gained from this study highlight the potential of hybrid energy storage systems based on lithium-ion batteries and reversible solid oxide cells (RSOCs) as well as offer a foundation for future research in the area of control and management of microgrids of this type.

References

[1] J. Xiao, L. Wang, Z. Qin, and P. Bauer, “A resilience enhanced secondary control for AC microgrids,” *IEEE Transactions on Smart Grid*, vol. 15, no. 1, pp. 810–820, Jan. 2024, ISSN: 1949-3053, 1949-3061.

[2] M. Ferraro, G. Brunaccini, F. Sergi, D. Aloisio, N. Randazzo, and V. Antonucci, “From uninterruptible power supply to resilient smart micro grid: The case of a battery storage at telecommunication station,” *Journal of Energy Storage*, vol. 28, p. 101 207, Apr. 1, 2020, ISSN: 2352-152X.

[3] E. Kuznetsova, “Microgrid agent-based modelling and optimization under uncertainty,”

[4] O. Anaya-Lara, N. Jenkins, J. Ekanayake, P. Cartwright, and M. Hughes, *Wind Energy Generation: Modelling and Control*. Wiley, 2011, ISBN: 978-1-119-96420-9.

[5] Z. Malekjamshidi, M. Jafari, J. Zhu, and D. Xiao, “Bidirectional power flow control with stability analysis of the matrix converter for microgrid applications,” *International Journal of Electrical Power & Energy Systems*, vol. 110, pp. 725–736, Sep. 2019, ISSN: 01420615.

[6] W.-N. Chang, C.-M. Chang, and S.-K. Yen, “Improvements in bidirectional power-flow balancing and electric power quality of a microgrid with unbalanced distributed generators and loads by using shunt compensators,” *Energies*, vol. 11, no. 12, p. 3305, Dec. 2018, ISSN: 1996-1073.

[7] N. Noroozi, S. Trip, and R. Geiselhart, “Model predictive control of DC microgrids: Current sharing and voltage regulation,” *IFAC-PapersOnLine*, vol. 51, no. 23, pp. 124–129, 2018, ISSN: 24058963.

[8] H. Golpîra and H. Bevrani, “Microgrids impact on power system frequency response,” *Energy Procedia*, vol. 156, pp. 417–424, Jan. 2019, ISSN: 18766102.

[9] L. Che, X. Shen, and M. Shahidehpour, “Primary frequency response based rescheduling for enhancing microgrid resilience,” *Journal of Modern Power Systems and Clean Energy*, vol. 7, no. 4, pp. 696–704, Jul. 2019, ISSN: 2196-5625, 2196-5420.

[10] T. Kerdphol, M. Watanabe, Y. Mitani, and V. Phunpeng, “Applying virtual inertia control topology to SMES system for frequency stability improvement of low-inertia microgrids driven by high renewables,” *Energies*, vol. 12, no. 20, p. 3902, Jan. 2019, ISSN: 1996-1073.

[11] A. Mehrizi-Sani, “Control strategies for the next generation microgrids,”

[12] H. Golpîra, “Bulk power system frequency stability assessment in presence of microgrids,” *Electric Power Systems Research*, vol. 174, p. 105 863, Sep. 2019, ISSN: 03787796.

[13] J. J. Justo, F. Mwasilu, J. Lee, and J.-W. Jung, “AC-microgrids versus DC-microgrids with distributed energy resources: A review,” *Renewable and Sustainable Energy Reviews*, vol. 24, pp. 387–405, Aug. 2013, ISSN: 13640321.

[14] A. Ghafouri, J. Milimonfared, and G. B. Gharehpetian, “Classification of microgrids for effective contribution to primary frequency control of power system,” *IEEE Systems Journal*, vol. 11, no. 3, pp. 1897–1906, Sep. 2017, ISSN: 1932-8184, 1937-9234, 2373-7816.

[15] K. Khani and G. Shahgholian, “Analysis and optimization of frequency control in isolated microgrid with double-fed induction-generators based wind turbine,” *Journal of International Council on Electrical Engineering*, vol. 9, no. 1, pp. 24–37, Jan. 1, 2019, ISSN: 2234-8972.

[16] S. K. Gudey and R. Gupta, “Recursive fast terminal sliding mode control in voltage source inverter for a low voltage microgrid system,” *IET Generation, Transmission & Distribution*, vol. 10, no. 7, pp. 1536–1543, May 2016, ISSN: 1751-8695, 1751-8695.

[17] L. K. Letting, J. L. Munda, and Y. Hamam, “Dynamic performance analysis of an integrated windphotovoltaic microgrid with storage,” *International Journal of Smart Grid and Clean Energy*, 2014, ISSN: 23154462.

[18] M. Uddin, H. Mo, D. Dong, S. Elsawah, J. Zhu, and J. M. Guerrero, “Microgrids: A review, outstanding issues and future trends,” *Energy Strategy Reviews*, vol. 49, p. 101 127, Sep. 2023, ISSN: 2211467X.

[19] G. Shahgholian, “A brief review on microgrids: Operation, applications, modeling, and control,” *International Transactions on Electrical Energy Systems*, vol. 31, no. 6, Jun. 2021, ISSN: 2050-7038, 2050-7038.

[20] M. Sorrentino, A. Adamo, and G. Nappi, “Optimal sizing of an rSOC-based renewable microgrid,” *Energy Procedia*, vol. 159, pp. 237–242, Feb. 2019, ISSN: 18766102.

[21] C. Marnay, S. Chatzivasileiadis, C. Abbey, *et al.*, “Microgrid evolution roadmap,” in *2015 International Symposium on Smart Electric Distribution Systems and Technologies (EDST)*, Vienna, Austria: IEEE, Sep. 2015, pp. 139–144, ISBN: 978-1-4799-7736-9.

[22] B. S. Hartono, Budiyanto, and R. Setiabudy, “Review of microgrid technology,” in *2013 International Conference on QiR*, Yogyakarta: IEEE, Jun. 2013, pp. 127–132, ISBN: 978-1-4673-5785-2.

[23] P. Degobert, S. Kreuawan, and X. Guillaud, “Micro-grid powered by photovoltaic and micro turbine,” *Renewable Energy and Power Quality Journal*, vol. 1, no. 4, pp. 188–191, Apr. 2006, ISSN: 2172038X.

[24] R. Lasseter, A. Akhil, C. Marnay, *et al.*, “Integration of distributed energy resources. the CERTS microgrid concept,” LBNL–50829, 799644, Apr. 1, 2002, LBNL–50 829, 799 644.

[25] W. Xu, S. Martel, and K. Mauch, “An assessment of distributed generation islanding detection methods and issues for canada,” Jul. 1, 2004.

[26] A. Keyhani, M. N. Marwali, and M. Dai, *Integration of Green and Renewable Energy in Electric Power Systems*, 1st ed. Wiley, Nov. 30, 2009, ISBN: 978-0-470-18776-0 978-0-470-55677-1.

[27] G. Xiao, A. Sun, H. Liu, M. Ni, and H. Xu, “Thermal management of reversible solid oxide cells in the dynamic mode switching,” *Applied Energy*, vol. 331, p. 120 383, Feb. 2023, ISSN: 03062619.

[28] A. Dimeas and N. Hatziargyriou, “Operation of a multiagent system for microgrid control,” *IEEE Transactions on Power Systems*, vol. 20, no. 3, pp. 1447–1455, Aug. 2005, ISSN: 0885-8950.

[29] S. Hajiaghasi, A. Salemnia, and M. Hamzeh, “Hybrid energy storage system for microgrids applications: A review,” *Journal of Energy Storage*, vol. 21, pp. 543–570, Feb. 1, 2019, ISSN: 2352-152X.

[30] T. M. I. Mahlia, T. J. Saktisahdan, A. Jannifar, M. H. Hasan, and H. S. C. Matseelar, “A review of available methods and development on energy storage; technology update,” *Renewable and Sustainable Energy Reviews*, vol. 33, pp. 532–545, May 1, 2014, ISSN: 1364-0321.

[31] H. Zhang, J. Baeyens, G. Cáceres, J. Degrève, and Y. Lv, “Thermal energy storage: Recent developments and practical aspects,” *Progress in Energy and Combustion Science*, vol. 53, pp. 1–40, Mar. 1, 2016, ISSN: 0360-1285.

[32] E. Chemali, M. Preindl, P. Malysz, and A. Emadi, “Electrochemical and electrostatic energy storage and management systems for electric drive vehicles: State-of-the-art review and future trends,” *IEEE Journal of Emerging and Selected Topics in Power Electronics*, vol. 4, no. 3, pp. 1117–1134, Sep. 2016, ISSN: 2168-6785.

[33] A. Cansiz, “4.14 electromechanical energy conversion,” in *Comprehensive Energy Systems*, I. Dincer, Ed., Oxford: Elsevier, Jan. 1, 2018, pp. 598–635, ISBN: 978-0-12-814925-6.

[34] G. J. May, A. Davidson, and B. Monahov, “Lead batteries for utility energy storage: A review,” *Journal of Energy Storage*, vol. 15, pp. 145–157, Feb. 1, 2018, ISSN: 2352-152X.

[35] G. Venkataramani, P. Parankusam, V. Ramalingam, and J. Wang, “A review on compressed air energy storage – a pathway for smart grid and polygeneration,” *Renewable and Sustainable Energy Reviews*, vol. 62, pp. 895–907, Sep. 1, 2016, ISSN: 1364-0321.

[36] S. Rehman, L. M. Al-Hadhrami, and M. M. Alam, “Pumped hydro energy storage system: A technological review,” *Renewable and Sustainable Energy Reviews*, vol. 44, pp. 586–598, Apr. 1, 2015, ISSN: 1364-0321.

[37] S. M. Mousavi G, F. Faraji, A. Majazi, and K. Al-Haddad, “A comprehensive review of flywheel energy storage system technology,” *Renewable and Sustainable Energy Reviews*, vol. 67, pp. 477–490, Jan. 1, 2017, ISSN: 1364-0321.

[38] A. A. K. Arani, H. Karami, G. B. Gharehpetian, and M. S. A. Hejazi, “Review of flywheel energy storage systems structures and applications in power systems and microgrids,” *Renewable and Sustainable Energy Reviews*, vol. 69, pp. 9–18, Mar. 1, 2017, ISSN: 1364-0321.

[39] M. Ghanaatian and S. Lotfifard, “Control of flywheel energy storage systems in the presence of uncertainties,” *IEEE Transactions on Sustainable Energy*, vol. 10, no. 1, pp. 36–45, Jan. 2019, ISSN: 1949-3037.

[40] T. A. Coombs, A. Cansiz, and A. M. Campbell, “A superconducting thrust-bearing system for an energy storage flywheel,” *Superconductor Science and Technology*, vol. 15, no. 5, p. 831, Apr. 2002, ISSN: 0953-2048.

[41] L. Zhang, X. Hu, Z. Wang, F. Sun, and D. G. Dorrell, “A review of supercapacitor modeling, estimation, and applications: A control/management perspective,” *Renewable and Sustainable Energy Reviews*, vol. 81, pp. 1868–1878, Jan. 1, 2018, ISSN: 1364-0321.

[42] A. Colmenar-Santos, E.-L. Molina-Ibáñez, E. Rosales-Asensio, and J.-J. Blanes-Peiró, “Legislative and economic aspects for the inclusion of energy reserve by a superconducting magnetic energy storage: Application to the case of the spanish electrical system,” *Renewable and Sustainable Energy Reviews*, vol. 82, pp. 2455–2470, Feb. 1, 2018, ISSN: 1364-0321.

[43] A. Alzahrani, S. K. Ramu, G. Devarajan, I. Vairavasundaram, and S. Vairavasundaram, “A review on hydrogen-based hybrid microgrid system: Topologies for hydrogen energy storage, integration, and energy management with solar and wind energy,” *Energies*, vol. 15, no. 21, p. 7979, Oct. 27, 2022, ISSN: 1996-1073.

[44] A. Etxeberria, I. Vechiu, H. Camblong, and J. Vinassa, “Hybrid energy storage systems for renewable energy sources integration in microgrids: A review,” in *2010 Conference Proceedings IPEC*, Oct. 2010, pp. 532–537.

[45] R. Hemmati and H. Saboori, “Emergence of hybrid energy storage systems in renewable energy and transport applications – a review,” *Renewable and Sustainable Energy Reviews*, vol. 65, pp. 11–23, Nov. 1, 2016, ISSN: 1364-0321.

[46] T. Zimmermann, P. Keil, M. Hofmann, M. F. Horsche, S. Pichlmaier, and A. Jossen, “Review of system topologies for hybrid electrical energy storage systems,” *Journal of Energy Storage*, vol. 8, pp. 78–90, Nov. 1, 2016, ISSN: 2352-152X.

[47] L. W. Chong, Y. W. Wong, R. K. Rajkumar, R. K. Rajkumar, and D. Isa, “Hybrid energy storage systems and control strategies for stand-alone renewable energy power systems,” *Renewable and Sustainable Energy Reviews*, vol. 66, pp. 174–189, Dec. 1, 2016, ISSN: 1364-0321.

[48] M. A. Hannan, M. M. Hoque, A. Mohamed, and A. Ayob, “Review of energy storage systems for electric vehicle applications: Issues and challenges,” *Renewable and Sustainable Energy Reviews*, vol. 69, pp. 771–789, Mar. 1, 2017, ISSN: 1364-0321.

[49] T. Bocklisch, “Hybrid energy storage approach for renewable energy applications,” *Journal of Energy Storage*, vol. 8, pp. 311–319, Nov. 1, 2016, ISSN: 2352-152X.

[50] W. Jing, C. Hung Lai, S. H. W. Wong, and M. L. D. Wong, “Battery-supercapacitor hybrid energy storage system in standalone DC microgrids: Areview,” *IET Renewable Power Generation*, vol. 11, no. 4, pp. 461–469, 2017, ISSN: 1752-1424.

[51] V. A. Boicea, “Energy storage technologies: The past and the present,” *Proceedings of the IEEE*, vol. 102, no. 11, pp. 1777–1794, Nov. 2014, ISSN: 1558-2256.

[52] R. K. Sharma and S. Mishra, “Dynamic power management and control of a PV PEM fuel-cell-based standalone ac/dc microgrid using hybrid energy storage,” *IEEE Transactions on Industry Applications*, vol. 54, no. 1, pp. 526–538, Jan. 2018, ISSN: 1939-9367.

[53] T. Alnejaili, S. Drid, D. Mehdi, L. Chrifi-Alaoui, R. Belarbi, and A. Hamdouni, “Dynamic control and advanced load management of a stand-alone hybrid renewable power system for remote housing,” *Energy Conversion and Management*, vol. 105, pp. 377–392, Nov. 15, 2015, ISSN: 0196-8904.

[54] G. Wang, M. Ciobotaru, and V. G. Agelidis, “Power smoothing of large solar PV plant using hybrid energy storage,” *IEEE Transactions on Sustainable Energy*, vol. 5, no. 3, pp. 834–842, Jul. 2014, ISSN: 1949-3037.

[55] Y. Y. Chia, L. H. Lee, N. Shafiabady, and D. Isa, “A load predictive energy management system for supercapacitor-battery hybrid energy storage system in solar application using the support vector machine,” *Applied Energy*, vol. 137, pp. 588–602, Jan. 1, 2015, ISSN: 0306-2619.

[56] A. J. Pimm and S. D. Garvey, “The economics of hybrid energy storage plant,” *International Journal of Environmental Studies*, vol. 71, no. 6, pp. 787–795, Nov. 2, 2014, ISSN: 0020-7233.

[57] P. Zhao, J. Wang, and Y. Dai, “Capacity allocation of a hybrid energy storage system for power system peak shaving at high wind power penetration level,” *Renewable Energy*, vol. 75, pp. 541–549, Mar. 1, 2015, ISSN: 0960-1481.

[58] Q. Jiang and H. Hong, “Wavelet-based capacity configuration and coordinated control of hybrid energy storage system for smoothing out wind power fluctuations,” *IEEE Transactions on Power Systems*, vol. 28, no. 2, pp. 1363–1372, May 2013, ISSN: 1558-0679.

[59] N. Mendis, K. M. Muttaqi, and S. Perera, “Management of low- and high-frequency power components in demand-generation fluctuations of a DFIG-based wind-dominated RAPS system using hybrid energy storage,” *IEEE Transactions on Industry Applications*, vol. 50, no. 3, pp. 2258–2268, May 2014, ISSN: 1939-9367.

[60] J. Li, A. M. Gee, M. Zhang, and W. Yuan, “Analysis of battery lifetime extension in a SMES-battery hybrid energy storage system using a novel battery lifetime model,” *Energy*, vol. 86, pp. 175–185, Jun. 15, 2015, ISSN: 0360-5442.

[61] Z. Zhang, R. Miyajima, Y. Sato, *et al.*, “Characteristics of compensation for fluctuating output power of a solar power generator in a hybrid energy storage system using a bi2223 SMES coil cooled by thermosiphon with liquid hydrogen,” *IEEE Transactions on Applied Superconductivity*, vol. 26, no. 4, pp. 1–5, Jun. 2016, ISSN: 1051-8223, 1558-2515.

[62] J. Li, R. Xiong, H. Mu, *et al.*, “Design and real-time test of a hybrid energy storage system in the microgrid with the benefit of improving the battery lifetime,” *Applied Energy*, vol. 218, pp. 470–478, May 15, 2018, ISSN: 0306-2619.

[63] T. Weitzel, M. Schneider, C. H. Glock, F. Löber, and S. Rinderknecht, “Operating a storage-augmented hybrid microgrid considering battery aging costs,” *Journal of Cleaner Production*, vol. 188, pp. 638–654, Jul. 1, 2018, ISSN: 0959-6526.

[64] F. Ongaro, S. Saggini, and P. Mattavelli, “Li-ion battery-supercapacitor hybrid storage system for a long lifetime, photovoltaic-based wireless sensor network,” *IEEE Transactions on Power Electronics*, vol. 27, no. 9, pp. 3944–3952, Sep. 2012, ISSN: 1941-0107.

[65] J. Zhuo, C. Chakrabarti, N. Chang, and S. Vrudhula, “Maximizing the lifetime of embedded systems powered by fuel cell-battery hybrids,” in *Proceedings of the 2006 international symposium on Low power electronics and design*, ser. ISLPED ’06, New York, NY, USA: Association for Computing Machinery, Oct. 4, 2006, pp. 424–429, ISBN: 978-1-59593-462-8.

[66] S. Mane, M. Mejari, F. Kazi, and N. Singh, “Improving lifetime of fuel cell in hybrid energy management system by lure–lyapunov-based control formulation,” *IEEE Transactions on Industrial Electronics*, vol. 64, no. 8, pp. 6671–6679, Aug. 2017, ISSN: 1557-9948.

[67] U. Akram. “A coordinated frequency regulation framework based on hybrid battery-ultracapacitor energy storage technologies | IEEE journals & magazine | IEEE xplore.” (),

[68] J. Fang, Y. Tang, H. Li, and X. Li, “A battery/ultracapacitor hybrid energy storage system for implementing the power management of virtual synchronous generators,” *IEEE Transactions on Power Electronics*, vol. 33, no. 4, pp. 2820–2824, Apr. 2018, ISSN: 1941-0107.

[69] D. Shin, Y. Kim, J. Seo, N. Chang, Y. Wang, and M. Pedram, “Battery-supercapacitor hybrid system for high-rate pulsed load applications,” in *2011 Design, Automation & Test in Europe*, Mar. 2011, pp. 1–4.

[70] C. R. Lashway, A. T. Elsayed, and O. A. Mohammed, “Hybrid energy storage management in ship power systems with multiple pulsed loads,” *Electric Power Systems Research*, vol. 141, pp. 50–62, Dec. 1, 2016, ISSN: 0378-7796.

[71] U. Manandhar, N. R. Tummuru, S. K. Kollimalla, A. Ukil, G. H. Beng, and K. Chaudhari, “Validation of faster joint control strategy for battery- and supercapacitor-based energy storage system,” *IEEE Transactions on Industrial Electronics*, vol. 65, no. 4, pp. 3286–3295, Apr. 2018, ISSN: 1557-9948.

[72] S. K. Kollimalla, M. K. Mishra, and N. L. Narasamma, “Design and analysis of novel control strategy for battery and supercapacitor storage system,” *IEEE Transactions on Sustainable Energy*, vol. 5, no. 4, pp. 1137–1144, Oct. 2014, ISSN: 1949-3037.

[73] S. Hajiaghasi, A. Salemnia, and M. Hamzeh, “Hybrid energy storage for microgrid performance improvement under unbalanced load conditions,” *Journal of Energy Management and Technology*, vol. 2, no. 1, pp. 30–39, Apr. 1, 2018, ISSN: 2588-3372.

[74] Y. Zhu, F. Zhuo, and F. Wang, “Coordination control of lithium battery-supercapacitor hybrid energy storage system in a microgrid under unbalanced load condition,” in *2014 16th European Conference on Power Electronics and Applications*, Aug. 2014, pp. 1–10.

[75] Q. Tabart, I. Vechiu, A. Etxeberria, and S. Bacha, “Hybrid energy storage system microgrids integration for power quality improvement using four-leg three-level NPC inverter and second-order sliding mode control,” *IEEE Transactions on Industrial Electronics*, vol. 65, no. 1, pp. 424–435, Jan. 2018, ISSN: 1557-9948.

[76] Z. Shuai, Y. Sun, Z. J. Shen, *et al.*, “Microgrid stability: Classification and a review,” *Renewable and Sustainable Energy Reviews*, vol. 58, pp. 167–179, May 1, 2016, ISSN: 1364-0321.

[77] L. Yang, N. Tai, and C. Fan, “Regulation and stabilization by ice storage air-conditioning and battery energy storage system in microgrids,” *IEEJ Transactions on Electrical and Electronic Engineering*, vol. 12, no. 2, pp. 176–184, 2017, ISSN: 1931-4981.

[78] L. Chen, H. Chen, Y. Li, *et al.*, “SMES-battery energy storage system for the stabilization of a photovoltaic-based microgrid,” *IEEE Transactions on Applied Superconductivity*, vol. 28, no. 4, pp. 1–7, Jun. 2018, ISSN: 1558-2515.

[79] Y. Yang, S. Bremner, C. Menictas, and M. Kay, “Battery energy storage system size determination in renewable energy systems: A review,” *Renewable and Sustainable Energy Reviews*, vol. 91, pp. 109–125, Aug. 1, 2018, ISSN: 1364-0321.

[80] S. Günther, A. Bensmann, and R. Hanke-Rauschenbach, “Theoretical dimensioning and sizing limits of hybrid energy storage systems,” *Applied Energy*, vol. 210, pp. 127–137, Jan. 15, 2018, ISSN: 0306-2619.

[81] Y. Liu, W. Du, L. Xiao, H. Wang, S. Bu, and J. Cao, “Sizing a hybrid energy storage system for maintaining power balance of an isolated system with high penetration of wind generation,” *IEEE Transactions on Power Systems*, vol. 31, no. 4, pp. 3267–3275, Jul. 2016, ISSN: 1558-0679.

[82] I. San Martín, A. Ursúa, and P. Sanchis, “Integration of fuel cells and supercapacitors in electrical microgrids: Analysis, modelling and experimental validation,” *International Journal of Hydrogen Energy*, vol. 38, no. 27, pp. 11 655–11 671, Sep. 10, 2013, ISSN: 0360-3199.

[83] G. Wang, M. Ciobotaru, and V. G. Agelidis, “Optimal capacity design for hybrid energy storage system supporting dispatch of large-scale photovoltaic power plant,” *Journal of Energy Storage*, vol. 3, pp. 25–35, Oct. 1, 2015, ISSN: 2352-152X.

[84] A. Abbassi, M. A. Dami, and M. Jemli, “A statistical approach for hybrid energy storage system sizing based on capacity distributions in an autonomous PV/wind power generation system,” *Renewable Energy*, vol. 103, pp. 81–93, Apr. 1, 2017, ISSN: 0960-1481.

[85] H. Jia, Y. Mu, and Y. Qi, “A statistical model to determine the capacity of battery–supercapacitor hybrid energy storage system in autonomous microgrid,” *International Journal of Electrical Power & Energy Systems*, vol. 54, pp. 516–524, Jan. 1, 2014, ISSN: 0142-0615.

[86] T. Zhou and W. Sun, “Optimization of battery–supercapacitor hybrid energy storage station in wind/solar generation system,” *IEEE Transactions on Sustainable Energy*, vol. 5, no. 2, pp. 408–415, Apr. 2014, ISSN: 1949-3037.

[87] M. Masih-Tehrani, M.-R. Ha'iri-Yazdi, V. Esfahanian, and A. Safaei, "Optimum sizing and optimum energy management of a hybrid energy storage system for lithium battery life improvement," *Journal of Power Sources*, 16th International Meeting on Lithium Batteries (IMLB), vol. 244, pp. 2–10, Dec. 15, 2013, ISSN: 0378-7753.

[88] S. Wen, H. Lan, D. C. Yu, *et al.*, "Optimal sizing of hybrid energy storage sub-systems in PV/diesel ship power system using frequency analysis," *Energy*, vol. 140, pp. 198–208, Dec. 1, 2017, ISSN: 0360-5442.

[89] Y. Ghiassi-Farrokhfal, C. Rosenberg, S. Keshav, and M.-B. Adjaho, "Joint optimal design and operation of hybrid energy storage systems," *IEEE Journal on Selected Areas in Communications*, vol. 34, no. 3, pp. 639–650, Mar. 2016, ISSN: 1558-0008.

[90] I. Janghorban Esfahani, P. Ifaei, J. Kim, and C. Yoo, "Design of hybrid renewable energy systems with battery/hydrogen storage considering practical power losses: A MEPoPA (modified extended-power pinch analysis)," *Energy*, vol. 100, pp. 40–50, Apr. 1, 2016, ISSN: 0360-5442.

[91] A. S. Jacob, R. Banerjee, and P. C. Ghosh, "Sizing of hybrid energy storage system for a PV based microgrid through design space approach," *Applied Energy*, vol. 212, pp. 640–653, Feb. 15, 2018, ISSN: 0306-2619.

[92] Y. Zhang, X. Tang, Z. Qi, and Z. Liu, "The ragone plots guided sizing of hybrid storage system for taming the wind power," *International Journal of Electrical Power & Energy Systems*, vol. 65, pp. 246–253, Feb. 1, 2015, ISSN: 0142-0615.

[93] J. Cao, W. Du, H. Wang, and M. McCulloch, "Optimal sizing and control strategies for hybrid storage system as limited by grid frequency deviations," *IEEE Transactions on Power Systems*, vol. 33, no. 5, pp. 5486–5495, Sep. 2018, ISSN: 1558-0679.

[94] T. Bocklisch, "Hybrid energy storage systems for renewable energy applications," *Energy Procedia*, 9th International Renewable Energy Storage Conference, IRES 2015, vol. 73, pp. 103–111, Jun. 1, 2015, ISSN: 1876-6102.

[95] H. Chen, T. N. Cong, W. Yang, C. Tan, Y. Li, and Y. Ding, "Progress in electrical energy storage system: A critical review," *Progress in Natural Science*, vol. 19, no. 3, pp. 291–312, Mar. 10, 2009, ISSN: 1002-0071.

[96] C. Spataru, Y. C. Kok, and M. Barrett, "Physical energy storage employed worldwide," *Energy Procedia*, 6th International Conference on Sustainability in Energy and Buildings, SEB-14, vol. 62, pp. 452–461, Jan. 1, 2014, ISSN: 1876-6102.

[97] T. S. Babu, K. R. Vasudevan, V. K. Ramachandaramurthy, S. B. Sani, S. Chemud, and R. M. Lajim, "A comprehensive review of hybrid energy storage systems: Converter topologies, control strategies and future prospects," *IEEE Access*, vol. 8, pp. 148 702–148 721, 2020, ISSN: 2169-3536.

[98] J. Zheng, T. Jow, and M. Ding, "Hybrid power sources for pulsed current applications," *IEEE Transactions on Aerospace and Electronic Systems*, vol. 37, no. 1, pp. 288–292, Jan. 2001, ISSN: 1557-9603.

[99] A. Lahyani, P. Venet, A. Guermazi, and A. Troudi, "Battery/supercapacitors combination in uninterruptible power supply (UPS)," *IEEE Transactions on Power Electronics*, vol. 28, no. 4, pp. 1509–1522, Apr. 2013, ISSN: 1941-0107.

[100] Z. Song, H. Hofmann, J. Li, X. Han, and M. Ouyang, "Optimization for a hybrid energy storage system in electric vehicles using dynamic programing approach," *Applied Energy*, vol. 139, pp. 151–162, Feb. 1, 2015, ISSN: 0306-2619.

[101] A. M. Gee, F. V. P. Robinson, and R. W. Dunn, "Analysis of battery lifetime extension in a small-scale wind-energy system using supercapacitors," *IEEE Transactions on Energy Conversion*, vol. 28, no. 1, pp. 24–33, Mar. 2013, ISSN: 1558-0059.

[102] I. J. Cohen, D. A. Wetz, J. M. Heinzel, and Q. Dong, "Design and characterization of an actively controlled hybrid energy storage module for high-rate directed energy applications," *IEEE Transactions on Plasma Science*, vol. 43, no. 5, pp. 1427–1433, May 2015, ISSN: 1939-9375.

[103] S. K. Kollimalla, M. K. Mishra, A. Ukil, and H. B. Gooi, “DC grid voltage regulation using new HESS control strategy,” *IEEE Transactions on Sustainable Energy*, vol. 8, no. 2, pp. 772–781, Apr. 2017, ISSN: 1949-3037.

[104] P. Bajpai and V. Dash, “Hybrid renewable energy systems for power generation in stand-alone applications: A review,” *Renewable and Sustainable Energy Reviews*, vol. 16, no. 5, pp. 2926–2939, Jun. 1, 2012, ISSN: 1364-0321.

[105] Y. Zhang, Z. Jiang, and X. Yu, “Control strategies for battery/supercapacitor hybrid energy storage systems,” in *2008 IEEE Energy 2030 Conference*, Nov. 2008, pp. 1–6.

[106] S.-J. Ahn, J.-W. Park, I.-Y. Chung, S.-I. Moon, S.-H. Kang, and S.-R. Nam, “Power-sharing method of multiple distributed generators considering control modes and configurations of a microgrid,” *IEEE Transactions on Power Delivery*, vol. 25, no. 3, pp. 2007–2016, Jul. 2010, ISSN: 1937-4208.

[107] K. Jin, X. Ruan, M. Yang, and M. Xu, “A hybrid fuel cell power system,” *IEEE Transactions on Industrial Electronics*, vol. 56, no. 4, pp. 1212–1222, Apr. 2009, ISSN: 1557-9948.

[108] S. Teleke, M. E. Baran, S. Bhattacharya, and A. Q. Huang, “Rule-based control of battery energy storage for dispatching intermittent renewable sources,” *IEEE Transactions on Sustainable Energy*, vol. 1, no. 3, pp. 117–124, Oct. 2010, ISSN: 1949-3037.

[109] R. Cozzolino, L. Tribioli, and G. Bella, “Power management of a hybrid renewable system for artificial islands: A case study,” *Energy*, vol. 106, pp. 774–789, Jul. 1, 2016, ISSN: 0360-5442.

[110] B. Wang, U. Manandhar, X. Zhang, H. B. Gooi, and A. Ukil, “Deadbeat control for hybrid energy storage systems in DC microgrids,” *IEEE Transactions on Sustainable Energy*, vol. 10, no. 4, pp. 1867–1877, Oct. 2019, ISSN: 1949-3037.

[111] Q. Xu, J. Xiao, P. Wang, X. Pan, and C. Wen, “A decentralized control strategy for autonomous transient power sharing and state-of-charge recovery in hybrid energy storage systems,” *IEEE Transactions on Sustainable Energy*, vol. 8, no. 4, pp. 1443–1452, Oct. 2017, ISSN: 1949-3037.

[112] M. Shi, X. Chen, J. Zhou, Y. Chen, J. Wen, and H. He, “Advanced secondary voltage recovery control for multiple HESSs in a droop-controlled DC microgrid,” *IEEE Transactions on Smart Grid*, vol. 10, no. 4, pp. 3828–3839, Jul. 2019, ISSN: 1949-3061.

[113] D. N. Huu, “An adaptive control of hybrid battery-supercapacitor storage for integration of wind and solar,” in *2016 IEEE International Conference on Sustainable Energy Technologies (ICSET)*, Nov. 2016, pp. 157–162.

[114] D. B. Wickramasinghe Abeywardana, B. Hredzak, and V. G. Agelidis, “A fixed-frequency sliding mode controller for a boost-inverter-based battery-supercapacitor hybrid energy storage system,” *IEEE Transactions on Power Electronics*, vol. 32, no. 1, pp. 668–680, Jan. 2017, ISSN: 1941-0107.

[115] B. Wang, J. Xu, R.-J. Wai, and B. Cao, “Adaptive sliding-mode with hysteresis control strategy for simple multimode hybrid energy storage system in electric vehicles,” *IEEE Transactions on Industrial Electronics*, vol. 64, no. 2, pp. 1404–1414, Feb. 2017, ISSN: 1557-9948.

[116] B.-H. Nguyễn, J. P. F. Trovão, R. German, and A. Bouscayrol, “Real-time energy management of parallel hybrid electric vehicles using linear quadratic regulation,” *Energies*, vol. 13, no. 21, p. 5538, Oct. 22, 2020, ISSN: 1996-1073.

[117] J. P. Torreglosa, P. García, L. M. Fernández, and F. Jurado, “Energy dispatching based on predictive controller of an off-grid wind turbine/photovoltaic/hydrogen/battery hybrid system,” *Renewable Energy*, vol. 74, pp. 326–336, Feb. 1, 2015, ISSN: 0960-1481.

[118] F. Garcia-Torres, L. Valverde, and C. Bordons, “Optimal load sharing of hydrogen-based microgrids with hybrid storage using model-predictive control,” *IEEE Transactions on Industrial Electronics*, vol. 63, no. 8, pp. 4919–4928, Aug. 2016, ISSN: 1557-9948.

[119] A. Vahidi, A. Stefanopoulou, and H. Peng, “Current management in a hybrid fuel cell power system: A model-predictive control approach,” *IEEE Transactions on Control Systems Technology*, vol. 14, no. 6, pp. 1047–1057, Nov. 2006, ISSN: 1558-0865.

[120] B. Hredzak, V. G. Agelidis, and M. Jang, “A model predictive control system for a hybrid battery-ultracapacitor power source,” *IEEE Transactions on Power Electronics*, vol. 29, no. 3, pp. 1469–1479, Mar. 2014, ISSN: 1941-0107.

[121] B. Hredzak, V. G. Agelidis, and G. D. Demetriades, “A low complexity control system for a hybrid DC power source based on ultracapacitor–lead–acid battery configuration,” *IEEE Transactions on Power Electronics*, vol. 29, no. 6, pp. 2882–2891, Jun. 2014, ISSN: 0885-8993, 1941-0107.

[122] J. Nunez Forestieri and M. Farasat, “Integrative sizing/real-time energy management of a hybrid supercapacitor/undersea energy storage system for grid integration of wave energy conversion systems,” *IEEE Journal of Emerging and Selected Topics in Power Electronics*, vol. 8, no. 4, pp. 3798–3810, Dec. 2020, ISSN: 2168-6777, 2168-6785.

[123] Chao Sun, Xiaosong Hu, S. J. Moura, and Fengchun Sun, “Velocity predictors for predictive energy management in hybrid electric vehicles,” *IEEE Transactions on Control Systems Technology*, vol. 23, no. 3, pp. 1197–1204, May 2015, ISSN: 1063-6536, 1558-0865.

[124] A. Brka, Y. M. Al-Abdeli, and G. Kothapalli, “Predictive power management strategies for stand-alone hydrogen systems: Operational impact,” *International Journal of Hydrogen Energy*, vol. 41, no. 16, pp. 6685–6698, May 4, 2016, ISSN: 0360-3199.

[125] I. H. Altas and A. M. Sharaf, “A novel maximum power fuzzy logic controller for photovoltaic solar energy systems,” *Renewable Energy*, vol. 33, no. 3, pp. 388–399, Mar. 1, 2008, ISSN: 0960-1481.

[126] R. Yumurtaci, “Role of energy management in hybrid renewable energy systems: Case study based analysis considering varying seasonal conditions,” *TURKISH JOURNAL OF ELECTRICAL ENGINEERING & COMPUTER SCIENCES*, 2013, ISSN: 13000632, 13036203.

[127] A. T. Azar, *Fuzzy Systems*.

[128] X. Feng, H. B. Gooi, and S. X. Chen, “Hybrid energy storage with multimode fuzzy power allocator for PV systems,” *IEEE Transactions on Sustainable Energy*, vol. 5, no. 2, pp. 389–397, Apr. 2014, ISSN: 1949-3029, 1949-3037.

[129] P. García, J. P. Torreglosa, L. M. Fernández, and F. Jurado, “Optimal energy management system for stand-alone wind turbine/photovoltaic/hydrogen/battery hybrid system with supervisory control based on fuzzy logic,” *International Journal of Hydrogen Energy*, vol. 38, no. 33, pp. 14 146–14 158, Nov. 4, 2013, ISSN: 0360-3199.

[130] P. Garcia, C. A. Garcia, L. M. Fernandez, F. Llorens, and F. Jurado, “ANFIS-based control of a grid-connected hybrid system integrating renewable energies, hydrogen and batteries,” *IEEE Transactions on Industrial Informatics*, vol. 10, no. 2, pp. 1107–1117, May 2014, ISSN: 1551-3203, 1941-0050.

[131] A. M. Ajmal, T. Sudhakar Babu, V. K. Ramachandaramurthy, D. Yousri, and J. B. Ekanayake, “Static and dynamic reconfiguration approaches for mitigation of partial shading influence in photovoltaic arrays,” *Sustainable Energy Technologies and Assessments*, vol. 40, p. 100 738, Aug. 1, 2020, ISSN: 2213-1388.

[132] S. Safari, M. M. Ardehali, and M. J. Sirizi, “Particle swarm optimization based fuzzy logic controller for autonomous green power energy system with hydrogen storage,” *Energy Conversion and Management*, Global Conference on Renewable energy and Energy Efficiency for Desert Regions 2011 “GCREEDER 2011”, vol. 65, pp. 41–49, Jan. 1, 2013, ISSN: 0196-8904.

[133] M. Sarvi and I. N. Avanaki, “An optimized fuzzy logic controller by water cycle algorithm for power management of stand-alone hybrid green power generation,” *Energy Conversion and Management*, vol. 106, pp. 118–126, Dec. 1, 2015, ISSN: 0196-8904.

[134] A. M. O. Haruni, M. Negnevitsky, M. E. Haque, and A. Gargoom, “A novel operation and control strategy for a standalone hybrid renewable power system,” *IEEE Transactions on Sustainable Energy*, vol. 4, no. 2, pp. 402–413, Apr. 2013, ISSN: 1949-3037.

[135] M. H. Athari and M. M. Ardehali, “Operational performance of energy storage as function of electricity prices for on-grid hybrid renewable energy system by optimized fuzzy logic controller,” *Renewable Energy*, vol. 85, pp. 890–902, Jan. 1, 2016, ISSN: 0960-1481.

[136] M.-E. Choi, S.-W. Kim, and S.-W. Seo, “Energy management optimization in a battery/supercapacitor hybrid energy storage system,” *IEEE Transactions on Smart Grid*, vol. 3, no. 1, pp. 463–472, Mar. 2012, ISSN: 1949-3053, 1949-3061.

[137] N. R. Tummuru, M. K. Mishra, and S. Srinivas, “Dynamic energy management of renewable grid integrated hybrid energy storage system,” *IEEE Transactions on Industrial Electronics*, vol. 62, no. 12, pp. 7728–7737, Dec. 2015, ISSN: 1557-9948.

[138] R. Sathishkumar, S. K. Kollimalla, and M. K. Mishra, “Dynamic energy management of micro grids using battery super capacitor combined storage,” in *2012 Annual IEEE India Conference (INDICON)*, Dec. 2012, pp. 1078–1083.

[139] U. Manandhar, A. Ukil, H. B. Gooi, *et al.*, “Energy management and control for grid connected hybrid energy storage system under different operating modes,” *IEEE Transactions on Smart Grid*, vol. 10, no. 2, pp. 1626–1636, Mar. 2019, ISSN: 1949-3053.

[140] N. Korada and M. K. Mishra, “Grid adaptive power management strategy for an integrated microgrid with hybrid energy storage,” *IEEE Transactions on Industrial Electronics*, vol. 64, no. 4, pp. 2884–2892, Apr. 2017, ISSN: 1557-9948.

[141] S. Kotra and M. K. Mishra, “A supervisory power management system for a hybrid microgrid with HESS,” *IEEE Transactions on Industrial Electronics*, vol. 64, no. 5, pp. 3640–3649, May 2017, ISSN: 1557-9948.

[142] “TalTech DC innovation hub | TalTech.” (Sep. 6, 2023),

[143] A. S. Dahane and R. B. Sharma, “Hybrid AC-DC microgrid coordinated control strategies: A systematic review and future prospect,” *Renewable Energy Focus*, vol. 49, p. 100 553, Jun. 1, 2024, ISSN: 1755-0084.

[144] A. Kirubakaran, S. Jain, and R. Nema, “A review on fuel cell technologies and power electronic interface,” *Renewable and Sustainable Energy Reviews*, vol. 13, no. 9, pp. 2430–2440, Dec. 2009, ISSN: 13640321.

[145] F. Ramadhani, M. A. Hussain, and H. Mokhlis, “A comprehensive review and technical guideline for optimal design and operations of fuel cell-based cogeneration systems,” *Processes*, vol. 7, no. 12, p. 950, Dec. 12, 2019, ISSN: 2227-9717.

[146] M. Perfil’ev, A. Demin, B. Kuzin, and A. Lipilin, *Vysokotemperaturnyj Jelektroliz Gazov*.

[147] N. Q. Minh, “Ceramic fuel cells,” *Journal of the American Ceramic Society*, vol. 76, no. 3, pp. 563–588, 1993, ISSN: 1551-2916.

[148] N. Minh, “Solid oxide fuel cell technology?features and applications,” *Solid State Ionics*, vol. 174, no. 1, pp. 271–277, Oct. 29, 2004, ISSN: 01672738.

[149] M. Ni and T. S. Zhao, *Solid Oxide Fuel Cells: From Materials to System Modeling*. Royal Society of Chemistry, Aug. 16, 2013, 539 pp., ISBN: 978-1-84973-777-7.

[150] K. A. Kuterbekov, A. V. Nikonov, K. Z. Bekmyrza, *et al.*, “Classification of solid oxide fuel cells,” *Nanomaterials*, vol. 12, no. 7, p. 1059, Mar. 24, 2022, ISSN: 2079-4991.

[151] W. Chin, J. Huang, Y. Liu, Y. Wu, and Y. Lee, “Correlation between the thickness of NiFe2o4 and hydrogen production performance for solid oxide electrolysis cells,” *International Journal of Hydrogen Energy*, vol. 52, pp. 994–1001, Jan. 2, 2024, ISSN: 0360-3199.

[152] K. Yang, Y. Wang, L. Jiang, Y. Jin, and Z. Yang, “Cobalt-free perovskite ba0.95la0.05feo3-δ as efficient and durable oxygen electrode for solid oxide electrolysis cells,” *International Journal of Hydrogen Energy*, vol. 48, no. 71, pp. 27 464–27 472, Aug. 19, 2023, ISSN: 0360-3199.

[153] Y. Tian, S. He, Y. Liu, *et al.*, “Comprehensive understanding of alkaline-earth elements effects on electrocatalytic activity and stability of LaFe0.8ni0.2o3 electrode for high-temperature CO2 electrolysis,” *Journal of CO2 Utilization*, vol. 53, p. 101 727, Nov. 1, 2021, ISSN: 2212-9820.

[154] Y. Tian, N. Abhishek, C. Yang, *et al.*, “Progress and potential for symmetrical solid oxide electrolysis cells,” *Matter*, vol. 5, no. 2, pp. 482–514, Feb. 2, 2022, ISSN: 2590-2385.

[155] R. Küngas, P. Blennow, T. Heiredal-Clausen, *et al.*, “Progress in SOEC development activities at haldor topsøe,” *ECS Transactions*, vol. 91, no. 1, p. 215, Jul. 10, 2019, ISSN: 1938-5862.

[156] Y. Liu, Y. Tian, Y. Wang, *et al.*, “Nano film pr2ni0.8cu0.2o4+δ decorated la0.6sr0.4co0.2fe0.8o3-δ oxygen electrode for highly efficient and stable reversible solid oxide cells,” *Electrochimica Acta*, vol. 430, p. 141 032, Oct. 20, 2022, ISSN: 0013-4686.

[157] Y. Xu, S. Cai, B. Chi, and Z. Tu, “Technological limitations and recent developments in a solid oxide electrolyzer cell: A review,” *International Journal of Hydrogen Energy*, vol. 50, pp. 548–591, Jan. 2024, ISSN: 03603199.

[158] Q. Guo, J. Geng, J. Pan, *et al.*, “Brief review of hydrocarbon-reforming catalysts map for hydrogen production,” *Energy Reviews*, vol. 2, no. 3, p. 100 037, Sep. 1, 2023, ISSN: 2772-9702.

[159] Y. Sun, J. Lu, Q. Liu, *et al.*, “Multi-objective optimizations of solid oxide co-electrolysis with intermittent renewable power supply via multi-physics simulation and deep learning strategy,” *Energy Conversion and Management*, vol. 258, p. 115 560, Apr. 15, 2022, ISSN: 0196-8904.

[160] A. Khouya, “Levelized costs of energy and hydrogen of wind farms and concentrated photovoltaic thermal systems. a case study in morocco,” *International Journal of Hydrogen Energy*, vol. 45, no. 56, pp. 31 632–31 650, Nov. 13, 2020, ISSN: 0360-3199.

[161] A. Mohammadi and M. Mehrpooya, “Thermodynamic and economic analyses of hydrogen production system using high temperature solid oxide electrolyzer integrated with parabolic trough collector,” *Journal of Cleaner Production*, vol. 212, pp. 713–726, Mar. 1, 2019, ISSN: 0959-6526.

[162] L. Lei, J. Zhang, Z. Yuan, J. Liu, M. Ni, and F. Chen, “Progress report on proton conducting solid oxide electrolysis cells,” *Advanced Functional Materials*, vol. 29, no. 37, p. 1 903 805, 2019, ISSN: 1616-3028.

[163] K.-Y. Park, T.-H. Lee, J.-T. Kim, *et al.*, “Highly conductive barium zirconate-based carbonate composite electrolytes for intermediate temperature-protonic ceramic fuel cells,” *Journal of Alloys and Compounds*, vol. 585, pp. 103–110, Feb. 5, 2014, ISSN: 0925-8388.

[164] N. Radenahmad, A. Afif, M. I. Petra, S. M. H. Rahman, S. Eriksson, and A. K. Azad, “High conductivity and high density proton conducting ba1−xSrxCe0.5zr0.35y0.1sm0.05o3−δ (x = 0.5, 0.7, 0.9, 1.0) perovskites for IT-SOFC,” *International Journal of Hydrogen Energy*, Special Issue: 1st International Conference on Hydrogen Energy, 20-22 July 2015, Aveiro, Portugal, vol. 41, no. 27, pp. 11 832–11 841, Jul. 20, 2016, ISSN: 0360-3199.

[165] Y. Wang, B. Zu, R. Zhan, Q. Du, M. Ni, and K. Jiao, “Three-dimensional modeling and performance optimization of proton conducting solid oxide electrolysis cell□,” *Fuel Cells*, vol. 20, no. 6, pp. 701–711, 2020, ISSN: 1615-6854.

[166] H. Boyer, S. Shimpalee, J. W. Weidner, and Z. Ma, “Mathematical modeling of a proton-conducting solid oxide electrolyzer cell using computational fluid dynamics simulation,” *ECS Meeting Abstracts*, vol. MA2019-02, no. 54, p. 2359, Sep. 1, 2019, ISSN: 2151-2043.

[167] L. Lei, J. Zhang, R. Guan, J. Liu, F. Chen, and Z. Tao, “Energy storage and hydrogen production by proton conducting solid oxide electrolysis cells with a novel heterogeneous design,” *Energy Conversion and Management*, vol. 218, p. 113 044, Aug. 15, 2020, ISSN: 0196-8904.

[168] R. Yang, Y. Tian, Y. Liu, J. Pu, and B. Chi, “Pd–la0.6sr0.4co0.2fe0.8o3–δ composite as active and stable oxygen electrode for reversible solid oxide cells,” *Journal of Rare Earths*, vol. 41, no. 4, pp. 599–604, Apr. 1, 2023, ISSN: 1002-0721.

[169] Y. Li, Y. Tian, J. Li, J. Pu, and B. Chi, “Sr-free orthorhombic perovskite pr0.8ca0.2fe0.8co0.2o3-δ as a high-performance air electrode for reversible solid oxide cell,” *Journal of Power Sources*, vol. 528, p. 231 202, Apr. 30, 2022, ISSN: 0378-7753.

[170] V. Subotić, T. Thaller, B. Königshofer, *et al.*, “Performance assessment of industrial-sized solid oxide cells operated in a reversible mode: Detailed numerical and experimental study,” *International Journal of Hydrogen Energy*, vol. 45, no. 53, pp. 29 166–29 185, Oct. 30, 2020, ISSN: 0360-3199.

[171] L. Blum, Q. Fang, L. G. J. d. Haart, *et al.*, “SOC development at forschungszentrum jülich,” *ECS Transactions*, vol. 78, no. 1, p. 1791, May 30, 2017, ISSN: 1938-5862.

[172] C. Yang, P. Li, R. Guo, *et al.*, “Modeling and evaluation of sintered microstructure and its properties for rSOFC fuel electrodes by coarse-grained molecular dynamics,” *Journal of Alloys and Compounds*, vol. 891, p. 161 977, Jan. 25, 2022, ISSN: 0925-8388.

[173] M. Preininger, B. Stoeckl, V. Subotić, F. Mittmann, and C. Hochenauer, "Performance of a ten-layer reversible solid oxide cell stack (rSOC) under transient operation for autonomous application," *Applied Energy*, vol. 254, p. 113 695, Nov. 15, 2019, ISSN: 0306-2619.

[174] X. Xing, J. Lin, N. Brandon, A. Banerjee, and Y. Song, "Time-varying model predictive control of a reversible-SOC energy-storage plant based on the linear parameter-varying method," *IEEE Transactions on Sustainable Energy*, vol. 11, no. 3, pp. 1589–1600, Jul. 2020, ISSN: 1949-3037.

[175] S. Srikanth, M. P. Heddrich, S. Gupta, and K. A. Friedrich, "Transient reversible solid oxide cell reactor operation – experimentally validated modeling and analysis," *Applied Energy*, vol. 232, pp. 473–488, Dec. 15, 2018, ISSN: 0306-2619.

[176] S. Y. Gómez and D. Hotza, "Current developments in reversible solid oxide fuel cells," *Renewable and Sustainable Energy Reviews*, vol. 61, pp. 155–174, Aug. 1, 2016, ISSN: 1364-0321.

[177] C. Wang, M. Chen, M. Liu, and J. Yan, "Dynamic modeling and parameter analysis study on reversible solid oxide cells during mode switching transient processes," *Applied Energy*, vol. 263, p. 114 601, Apr. 1, 2020, ISSN: 0306-2619.

[178] L. Barelli, G. Bidini, G. Cinti, and A. Ottaviano, "Study of SOFC-SOE transition on a RSOFC stack," *International Journal of Hydrogen Energy*, vol. 42, no. 41, pp. 26 037–26 047, Oct. 12, 2017, ISSN: 0360-3199.

[179] O. Posdziech, K. Schwarze, and J. Brabandt, "Efficient hydrogen production for industry and electricity storage via high-temperature electrolysis," *International Journal of Hydrogen Energy*, A Special Issue with the Papers Selected from the 7th World Hydrogen Technologies Convention, vol. 44, no. 35, pp. 19 089–19 101, Jul. 19, 2019, ISSN: 0360-3199.

[180] G. Vialetto, M. Noro, P. Colbertaldo, and M. Rokni, "Enhancement of energy generation efficiency in industrial facilities by SOFC – SOEC systems with additional hydrogen production," *International Journal of Hydrogen Energy*, Special Issue on Power To Gas and Hydrogen applications to energy systems at different scales - Building, District and National level, vol. 44, no. 19, pp. 9608–9620, Apr. 12, 2019, ISSN: 0360-3199.

[181] J. Mermelstein and O. Posdziech, "Development and demonstration of a novel reversible SOFC system for utility and micro grid energy storage," *Fuel Cells*, vol. 17, no. 4, pp. 562–570, 2017, ISSN: 1615-6854.

[182] L. Wang, Y. Zhang, M. Pérez-Fortes, *et al.*, "Reversible solid-oxide cell stack based power-to-x-to-power systems: Comparison of thermodynamic performance," *Applied Energy*, vol. 275, p. 115 330, Oct. 1, 2020, ISSN: 0306-2619.

[183] J. Elio, P. Phelan, R. Villalobos, and R. J. Milcarek, "A review of energy storage technologies for demand-side management in industrial facilities," *Journal of Cleaner Production*, vol. 307, p. 127 322, Jul. 2021, ISSN: 09596526.

[184] "RAMP documentation" (https://rampdemand.readthedocs.io/en/latest/).

[185] "Global solar atlas," (https://globalsolaratlas.info/).

[186] *JINKO JKM245p-60 datasheet*.

[187] RESU10, 9.8kwh battery pack specification.

[188] "Elcogen | solid oxide fuel cells and stacks" (https://elcogen.com/), Affordable Green Hydrogen.

[189] M. Noritake, K. Yuasa, T. Takeda, *et al.*, "Experimental study of a 400 v class DC microgrid for commercial buildings," in *2015 9th International Conference on Power Electronics and ECCE Asia (ICPE-ECCE Asia)*, Seoul, South Korea: IEEE, Jun. 2015, pp. 1730–1735, ISBN: 978-89-5708-254-6.

A

Source Code of stochastic load profile simulation

The following code is fully written by the author of the thesis and is using RAMP Python library for stochastic simulations of load profiles. This is the main part of the code. Smaller parts, used for plotting or specific tests are not included, but can be easily obtained from here.

```
"""
# -*- coding: utf-8 -*-

# %% Definition of the inputs
"""
Input data definition
"""



from ramp.core.core import User
import numpy as np
import pandas as pd
import matplotlib.pyplot as plt

resortOccupancyLevel = 1.0 # A parameter which describes how full the resort is. It
    influences the load profile.


User_list = []



# Create new user classes
Private_House = User("Private House")
Staff_Quarter = User("Staff Quarter")
Rafiki_House = User("Rafiki House")
Kitchen_and_Storage = User("Kitchen and Storage")
Reception = User("Reception")
Tumaini_House = User("Tumaini House")
Security_Lights = User("Security Lights")
Dance_Hall = User("Dance Hall")
Open_Space = User("Open Space")
Workshop = User("Workshop")
Other = User("Other")
Future_Cottages = User("Future Cottages")

User_list = [Private_House, Staff_Quarter, Rafiki_House, Kitchen_and_Storage, Reception,
    Tumaini_House, Security_Lights, Dance_Hall, Open_Space, Workshop, Other, Future_Cottages]
```

```
# Create new appliances

# Private house
Indoor_LED_lights_PH = Private_House.Appliance(number=40,
power=10,
num_windows=1,
func_time = 240, #total time (minutes) the appliance is on during the day (not dependant on
    windows). Acceptable values are in range 0 to 1440, by default 0
fixed = "no" #if ‘’yes, all the ‘’n appliances of this kind are always switched-on together,
    by default ""no
)
Indoor_LED_lights_PH.windows(window_1 =[1080, 1320],
random_var_w =0.2 #variability of the windows, the same for all windows, by default 0
)

Floor_fans_PH = Private_House.Appliance(number=2,
power=45,
num_windows=2,
func_time = 660, #total time (minutes) the appliance is on during the day (not dependant on
    windows). Acceptable values are in range 0 to 1440, by default 0
fixed = "no", #if ‘’yes, all the ‘’n appliances of this kind are always switched-on together,
     by default ""no
)

Floor_fans_PH.windows(window_1 =[0, 480],
window_2 =[1260, 1440],
random_var_w =0.1 #variability of the windows, the same for all windows, by default 0
)

Floor_fans_for_guests_PH = Private_House.Appliance(number=4,
power=45,
num_windows=2,
func_time = 660, #total time (minutes) the appliance is on during the day (not dependant on
    windows). Acceptable values are in range 0 to 1440, by default 0
fixed = "no", #if ‘’yes, all the ‘’n appliances of this kind are always switched-on together,
     by default ""no
occasional_use=0.25
)

Floor_fans_for_guests_PH.windows(window_1 =[0, 480],
window_2 =[1260, 1440],
random_var_w =0.1 #variability of the windows, the same for all windows, by default 0
)

Computers_PH = Private_House.Appliance(
    number=2,
    power=80, # Power consumption of each computer
    num_windows=1, # Number of operating windows during the day
    func_time=60, # Computer is used for 1 hour per person per day on average
    fixed="no", # If ‘’yes, all the ‘’n appliances of this kind are always switched-on
        together. By default ""no
)

Computers_PH.windows(
    window_1=[420, 1320], # Operating windows for the computers, 7am to 10pm in minutes (from
         7*60=420 to 22*60=1320)
    random_var_w=0.0 # Variability of the windows, the same for all windows, by default 0
)

Computers_for_Guests_PH = Private_House.Appliance(
    number=4,
    power=80, # Power consumption of each computer
    num_windows=1, # Number of operating windows during the day
    func_time=60, # Computer is used for 1 hour per person per day on average
    fixed="no", # If ‘’yes, all the ‘’n appliances of this kind are always switched-on
        together. By default ""no
    occasional_use=0.25
)

Computers_for_Guests_PH.windows(
```

```
    window_1=[420, 1320], # Operating windows for the computers, 7am to 10pm in minutes (from
        7*60=420 to 22*60=1320)
    random_var_w=0.0 # Variability of the windows, the same for all windows, by default 0
)


Phone_charging_PH = Private_House.Appliance(
    number=2,
    power=5, # Power consumption of each phone charger in watts
    num_windows=1, # Number of operating windows during the day, which is only at night in
        this case
    func_time=60,
    fixed="no", # If ''yes, all the ''n appliances of this kind are always switched-on
        together. By default ""no
    func_cycle=10, #minimum time(minutes) the appliance is kept on after switch-on event
)

Phone_charging_PH.windows(
    window_1=[0, 1440], # Operating window for charging phones, representing night time.
        Might need adjustment for exact times.
    random_var_w=0.0 # Variability of the windows, the same for all windows, by default 0
)


Phone_charging_for_Guests_PH = Private_House.Appliance(
    number=4,
    power=5, # Power consumption of each phone charger in watts
    num_windows=1, # Number of operating windows during the day, which is only at night in
        this case
    func_time=60,
    fixed="no", # If ''yes, all the ''n appliances of this kind are always switched-on
        together. By default ""no
    func_cycle=10, #minimum time(minutes) the appliance is kept on after switch-on event
    occasional_use=0.25
)

Phone_charging_for_Guests_PH.windows(
    window_1=[0, 1440], # Operating window for charging phones, representing night time.
        Might need adjustment for exact times.
    random_var_w=0.0 # Variability of the windows, the same for all windows, by default 0
)


""" # Connected to the distribution grid """


Filter_coffee_machine = Private_House.Appliance(
    number=1, # Only one coffee machine
    power=1400, # Power consumption in watts
    num_windows=1, # Number of operating windows during the day
    func_time=20, # Total time the appliance is on during the day: 20 minutes
    fixed="yes", # If ''yes, all the ''n appliances of this kind are always switched-on
        together. By default ""no
    func_cycle=3, # minimum time(minutes) the appliance is kept on after switch-on event, by
        default 1
)

Filter_coffee_machine.windows(
    window_1=[360, 480], # Operating window between 6 to 8 am (converted to minutes: 6*60=360
        to 8*60=480)
    random_var_w=0.3 # Variability of the window, allowing for some fluctuation in start/end
        times
)

Washing_machine_PH = Private_House.Appliance(
    number=1, # Typically one washing machine
    power=2100, # Power consumption in watts
    num_windows=1, # Assuming one operational window per day it's used
    func_time=60,
    fixed="yes", # # If ''yes, all the ''n appliances of this kind are always switched-on
        together. By default ""no
```

```
    occasional_use=0.5, # Defines how often the appliance is used, e.g. every second day will
         be 0.5, by default 1
    func_cycle=60, # minimum time(minutes) the appliance is kept on after switch-on event, by
         default 1
)

Washing_machine_PH.windows(
    window_1=[360, 1020], # Daytime operation, but we specify the appliance might operate any
         time in a broad window since exact timing may vary; every other day handling is
        outside this configuration
    random_var_w=0.0 # Variability of the window
)



Fridge_big_PH = Private_House.Appliance(
    number=2, # Two big fridges
    power=85, # Power consumption in watts
    num_windows=1, # Operates continuously, but window is formalized for consistency
    func_time=1440, # On 24 hours a day
    fixed="yes", #if ‘’yes, all the ‘’n appliances of this kind are always switched-on
        together, by default ""no
)

Fridge_big_PH.windows(
    window_1=[0, 1440], # 24-hour operation, from midnight to midnight
    random_var_w=0 # No variability; these appliances are always on
)

Fridge_small_PH = Private_House.Appliance(
    number=1, # One small fridge, but only used occasionally
    power=50, # Power consumption in watts
    num_windows=1, # Operates continuously, but only when visitors come
    func_time=1440, # On 24 hours a day, but only activated occasionally
    fixed="yes", #if ‘’yes, all the ‘’n appliances of this kind are always switched-on
        together, by default ""no
    occasional_use=0.2
)

Fridge_small_PH.windows(
    window_1=[0, 1440], # 24-hour operation, from midnight to midnight, when in use
    random_var_w=0 # No variability; this appliance is always on when it's needed
)


Blender = Private_House.Appliance(
    number=1, # Only one blender
    power=400, # Power consumption in watts
    num_windows=1, # One operational window during the day
    func_time=5, # Used for only a few minutes once per day
    fixed="yes", #if ‘’yes, all the ‘’n appliances of this kind are always switched-on
        together, by default ""no

)

Blender.windows(
    window_1=[420, 1140], # Operational window from 7 am to 7 pm (7*60=420 to 19*60=1140 in
        minutes)
    random_var_w=0.3 # Variability of the window, allowing for fluctuation in operation time
        within the window
)



Toaster = Private_House.Appliance(
    number=1, # Typically one toaster
    power=400, # Power consumption in watts
    num_windows=1, # One operational window in the morning
    func_time=5, # Used for only a few minutes
    fixed="yes", #if ‘’yes, all the ‘’n appliances of this kind are always switched-on
        together, by default ""no
```

```
)

Toaster.windows(
    window_1=[420, 480], # Operating window from 7 am to 8 am (7*60=420 to 8*60=480 in
        minutes)
    random_var_w=0.3 # Variability of the window
)



Kitchen_oven_PH = Private_House.Appliance(
    number=1, # One kitchen oven
    power=1100, # Power consumption in watts
    num_windows=1,
    func_time=130, # Assuming 3 hours total use for bread making or lunch/dinner preparation,
         and decrease in this amount if the resort is not full
    fixed="yes", #if ‘’yes, all the ‘’n appliances of this kind are always switched-on
        together, by default ""no
    func_cycle=25, # minimum time(minutes) the appliance is kept on after switch-on event, by
         default 1
)

Kitchen_oven_PH.windows(
    window_1=[360, 1200], # Broad operational window from 6 am to 8 pm to cover potential use
         for bread making, lunch, or dinner (6*60=360 to 20*60=1200 in minutes)
    random_var_w=0.05 # Variability of the window, allowing for fluctuation in operation
        times within the broad window
)



Vacuum_cleaner_PH = Private_House.Appliance(
    number=1, # Only one vacuum cleaner
    power=1200, # Power consumption
    num_windows=1, # One operational window during the week
    func_time=60, # Used once per week for a maximum of 1 hour
    fixed="yes", #if ‘’yes, all the ‘’n appliances of this kind are always switched-on
        together, by default ""no
    occasional_use = 0.1, # Defines how often the appliance is used, e.g. every second day
        will be 0.5, by default 1
    func_cycle=5, # minimum time(minutes) the appliance is kept on after switch-on event, by
        default 1
)

Vacuum_cleaner_PH.windows(
    window_1=[480, 1080], # Operational window from 8 am to 6 pm
    random_var_w=0.1 # Variability of the window, allowing for fluctuation in operation time
        within the window
)

Dehumidifier_PH = Private_House.Appliance(
    number=1,  # Only one dehumidifier
    power=400,  # Power consumption in watts
    num_windows=1,
    func_time=360,  # 6 hours per day
    fixed="yes",  #if ‘’yes, all the ‘’n appliances of this kind are always switched-on
        together, by default ""no
)

Dehumidifier_PH.windows(
    window_1=[480, 1200],  # Potential operational window
    random_var_w=0.0  # Variability of the window
)

Instant_water_heater = Private_House.Appliance(
    number= 1,
    power= 5500,
    num_windows= 1,
    func_time=5, #07:00-22:00
)
Instant_water_heater.windows(
```

```
    window_1=[420, 1320],  # 07:00-22:00
)



# Staff Quarter

Indoor_LED_lights_SQ = Staff_Quarter.Appliance(
    number=10,  # 10 LED lights in the staff quarter
    power=10,  # Power consumption of each LED light in watts
    num_windows=1,  # One operational window during the day
    func_time=240,
    fixed="no",  # If ‘’yes, all the ‘’n appliances of this kind are always switched-on
        together, by default ""no
)

Indoor_LED_lights_SQ.windows(
    window_1=[1080, 1320],
    random_var_w=0.0  # No variability of the windows, consistent usage every day
)

Floor_fans_SQ = Staff_Quarter.Appliance(
    number=2,  # 2 floor fans in the staff quarter
    power=45,  # Power consumption of each floor fan in watts
    num_windows=2,  # One operational window during the night
    func_time=540,  # Total time (minutes) the fans are on during the night (9 pm to 6 am is
        9 hours, so 9*60 = 540 minutes)
    fixed="no",  # If ‘’yes, all the ‘’n appliances of this kind are always switched-on
        together, by default ""no
)

Floor_fans_SQ.windows(
    window_1=[0, 360],  # Operational window from 9 pm to 6 am (21*60=1260 to 6*60=360 in
        minutes)
    window_2=[1260, 1440],
    random_var_w=0.0  # No variability of the windows, consistent usage every night
)


Phone_charging_SQ = Staff_Quarter.Appliance(
    number=6,  # 6 spots for phone charging in the staff quarter
    power=5,  # Power consumption of each phone charger in watts
    num_windows=1,  # Available for charging 24 hours but only used for a few hours
    func_time=180,
    fixed="no",  # If ‘’yes, all the ‘’n appliances of this kind are always switched-on
        together, by default ""no
    func_cycle=10,  # Minimum time (minutes) the appliance is kept on after switch-on event
)

Phone_charging_SQ.windows(
    window_1=[0, 1440],  # Available for charging any time during the 24-hour period
    random_var_w=0.0  # No variability of the windows, consistent availability
)


""" # Connected to the distribution grid """

Fridge_SQ = Staff_Quarter.Appliance(
    number=1,  # One fridge in the staff quarter
    power=85,  # Power consumption in watts
    num_windows=1,  # Operates continuously, so technically only one window
    func_time=1440,  # On 24 hours a day
    fixed="yes",  # If ‘’yes, the appliance is always switched-on together
)

Fridge_SQ.windows(
    window_1=[0, 1440],  # 24-hour operation, from midnight to midnight
    random_var_w=0  # No variability; the appliance is always on
)
```

```
Iron_SQ = Staff_Quarter.Appliance(
    number=1,  # One iron in the staff quarter
    power=1000,  # Power consumption in watts
    num_windows=1,  # Assuming one operational window during the day when the iron is used
    func_time=60,  # Used for a maximum of 1 hour per day
    fixed="yes",  # If ‘’yes, the appliance is always switched-on together for its duration
)

Iron_SQ.windows(
    window_1=[600, 1080],  # Operational window from 10 am to 6 pm (10*60=600 to 18*60=1080
        in minutes)
    random_var_w=0.0  # No variability of the window, consistent usage every day
)



Washing_machine_SQ = Staff_Quarter.Appliance(
    number=1,  # One washing machine in the staff quarter
    power=2100,  # Power consumption in watts
    num_windows=1,  # Assuming one operational window per day it's used
    func_time=60 ,
    fixed="yes",  # If ‘’yes, the appliance is always switched-on together for its duration
    occasional_use= 0.25,
    func_cycle=60,  # Minimum time (minutes) the appliance is kept on after switch-on event,
        by default 1
)

Washing_machine_SQ.windows(
    window_1=[0, 1440],  # Broad daytime operation window, exact timing may vary
    random_var_w=0.0  # No variability of the window
)



# Rafiki House setup


# Indoor LED lights
Indoor_LED_lights_RH = Rafiki_House.Appliance(
    number=round(22*resortOccupancyLevel),
    power=10,
    num_windows=1,
    func_time=240,
    fixed="no"
)
Indoor_LED_lights_RH.windows(window_1=[1080, 1320])

# Floor fans
Floor_fans_RH = Rafiki_House.Appliance(
    number=round(3*resortOccupancyLevel),
    power=45,
    num_windows=3,
    func_time=900,  # 15 hours total: 9pm to 9am + 1pm to 4pm
    fixed="no"
)
Floor_fans_RH.windows(window_1=[0, 540],
window_2=[780, 960],
window_3=[1260, 1440]
)  # 9pm to 9am and 1pm to 4pm in minutes

# Computers
Computers_RH = Rafiki_House.Appliance(
    number=round(4*resortOccupancyLevel),
    power=80,
    num_windows=1,
    func_time=120,
    fixed="no"
)
Computers_RH.windows(window_1=[420, 1320])  # 7am to 10pm in minutes
```

```
Phone_charging_RH = Rafiki_House.Appliance(
    number=round(6*resortOccupancyLevel),
    power=5, # Power consumption of each phone charger in watts
    num_windows=1, # Number of operating windows during the day, which is only at night in
        this case
    func_time=60,
    fixed="no", # If ''yes, all the ''n appliances of this kind are always switched-on
        together. By default ""no
    func_cycle=10, #minimum time(minutes) the appliance is kept on after switch-on event
)

Phone_charging_RH.windows(
    window_1=[0, 1440], # Operating window for charging phones, representing night time.
        Might need adjustment for exact times.
    random_var_w=0.0 # Variability of the windows, the same for all windows, by default 0
)

Heating_element_RH = Rafiki_House.Appliance(
    number=1,
    power=1500,  # Power in watts
    num_windows=1,
    func_time=4.65*4*resortOccupancyLevel,  # Actual time the device is used during the day,
        in minutes
    occasional_use=0.3, # Used only on cold days
)
Heating_element_RH.windows(
    window_1=[420, 1320],  # Operational window: 07:00-22:00 in minutes from midnight
)




# Kitchen and Storage setup

# Indoor LED lights
Indoor_LED_lights_KS = Kitchen_and_Storage.Appliance(
    number=10,
    power=12,
    num_windows=1,
    func_time=240*resortOccupancyLevel,  # 4 hours from 6pm to 10pm: 4 * 60 = 240 minutes
    fixed="no"
)
Indoor_LED_lights_KS.windows(window_1=[1080, 1320])  # 6pm to 10pm in minutes

# Kettle
Kettle_KS = Kitchen_and_Storage.Appliance(
    number=1,
    power=1500,
    num_windows=1,
    func_time=2+13*resortOccupancyLevel,
    fixed="yes"
)
Kettle_KS.windows(window_1=[360, 1140])  # 6 am to 7pm in minutes

# Bread machine
Bread_machine_KS = Kitchen_and_Storage.Appliance(
    number=1,
    power=1000,
    num_windows=1,
    func_time=40 * resortOccupancyLevel,  # Only 40 min per day max
    fixed="yes"
)
Bread_machine_KS.windows(window_1=[780, 900])  # 1 pm to 3 pm in minutes

# Toaster
Toaster_KS = Kitchen_and_Storage.Appliance(
    number=1,
    power=400,
    num_windows=1,
    func_time=40 * resortOccupancyLevel,  # Only 40 min per day max
```

```
    fixed="yes"
)
Toaster_KS.windows(window_1=[420, 540])  # 7 am to 9 am in minutes

# Soup blender
Soup_blender_KS = Kitchen_and_Storage.Appliance(
    number=1,
    power=800,
    num_windows=1,
    func_time=20 * resortOccupancyLevel,  # Max 30 min per day
    fixed="yes"
)
Soup_blender_KS.windows(window_1=[600, 1140])  # 10 am to 7 pm in minutes

# Blender
Blender_KS = Kitchen_and_Storage.Appliance(
    number=1,
    power=400,
    num_windows=1,
    func_time=30 * resortOccupancyLevel,  # Max 30 min per day
    fixed="yes"
)
Blender_KS.windows(window_1=[420, 540])  # 7 am to 9 am in minutes

# Fridge small
Fridge_small_KS = Kitchen_and_Storage.Appliance(
    number=1,
    power=50,
    num_windows=1,
    func_time=1440,  # 24 hours
    fixed="yes"
)
Fridge_small_KS.windows(window_1=[0, 1440])  # 24 hours

# Fridge medium
Fridge_medium_KS = Kitchen_and_Storage.Appliance(
    number=1,
    power=85,
    num_windows=1,
    func_time=1440,  # 24 hours
    fixed="yes"
)
Fridge_medium_KS.windows(window_1=[0, 1440])  # 24 hours

# Fridge big
Fridge_big_KS = Kitchen_and_Storage.Appliance(
    number=1,
    power=150,
    num_windows=1,
    func_time=1440,  # 24 hours
    fixed="yes"
)
Fridge_big_KS.windows(window_1=[0, 1440])  # 24 hours

# Freezer
Freezer_KS = Kitchen_and_Storage.Appliance(
    number=1,
    power=180,
    num_windows=1,
    func_time=1440,  # 24 hours
    fixed="yes"
)
Freezer_KS.windows(window_1=[0, 1440])  # 24 hours

# Music speaker
Music_speaker_KS = Kitchen_and_Storage.Appliance(
    number=1,
    power=40,
    num_windows=1,
    func_time=300*resortOccupancyLevel,  # 5 hours from 4 pm to 9 pm
    fixed="no"
```

```
)
Music_speaker_KS.windows(window_1=[960, 1260])  # 4 pm to 9pm in minutes

# Filter coffee machine
Filter_coffee_machine_KS = Kitchen_and_Storage.Appliance(
    number=1,
    power=1400,
    num_windows=1,
    func_time=30*resortOccupancyLevel,  # Only 30 min per day max
    fixed="yes"
)
Filter_coffee_machine_KS.windows(window_1=[420, 540])  # 7 am to 9 am in minutes

# Wall fans
Wall_fans_KS = Kitchen_and_Storage.Appliance(
    number=2,
    power=60,
    num_windows=1,
    func_time=180,  # 3 hours from 1pm to 4pm, only on hot days
    fixed="no",
    occasional_use=0.3  # Assuming a 30% probability of hot days
)
Wall_fans_KS.windows(window_1=[780, 960])  # 1pm to 4pm in minutes


# Reception setup


# Indoor LED lights
Indoor_LED_lights_Rec = Reception.Appliance(
    number=10,
    power=5,
    num_windows=1,
    func_time=180,  # 3 hours from 6pm to 9pm
    fixed="no"
)
Indoor_LED_lights_Rec.windows(window_1=[1080, 1260])  # 6pm to 9pm in minutes

# Phone charging
Phone_charging_Rec = Reception.Appliance(
    number=3,
    power=5,
    num_windows=1,
    func_time=150,  # Assuming "Daytime" is 12 hours
    fixed="no"
)
Phone_charging_Rec.windows(window_1=[480, 1200])  # Assuming "Daytime" from 8 am to 8 pm

# Computer
Computer_Rec = Reception.Appliance(
    number=1,
    power=80,
    num_windows=1,
    func_time=60,  # Max 1 hour per day
    fixed="yes"
)
Computer_Rec.windows(window_1=[540, 1260])  # 9 am to 9 pm in minutes

# Printer
Printer_Rec = Reception.Appliance(
    number=1,
    power=250,
    num_windows=1,
    func_time=10 * resortOccupancyLevel,  # Max 10 min per day
    fixed="yes"
)
Printer_Rec.windows(window_1=[540, 1260])  # 9 am to 9 pm in minutes
```

```
# Tumaini House setup


# Indoor LED lights
Indoor_LED_lights_TH = Tumaini_House.Appliance(
    number=round(30*resortOccupancyLevel),
    power=10,
    num_windows=1,
    func_time=240,
    fixed="no"
)
Indoor_LED_lights_TH.windows(window_1=[1080, 1320])

# Floor fans
Floor_fans_TH = Tumaini_House.Appliance(
    number=round(3*resortOccupancyLevel),
    power=45,
    num_windows=3,
    func_time=900,  # 15 hours total
    fixed="no"
)
Floor_fans_TH.windows(window_1=[0, 540],
window_2=[780, 960],
window_3=[1260, 1440]
)  # 9pm to 9am and 1pm to 4pm in minutes  # 9pm to 9am and 1pm to 4pm in minutes

# Computers
Computers_TH = Tumaini_House.Appliance(
    number=round(4*resortOccupancyLevel),
    power=80,
    num_windows=1,
    func_time=120,  #
    fixed="no"
)
Computers_TH.windows(window_1=[420, 1320])  # 7am to 10pm in minutes

# Phone charging
Phone_charging_TH = Tumaini_House.Appliance(
    number=round(6*resortOccupancyLevel),
    power=5, # Power consumption of each phone charger in watts
    num_windows=1, # Number of operating windows during the day, which is only at night in
        this case
    func_time=60,
    fixed="no", # If ‘’yes, all the ‘’n appliances of this kind are always switched-on
        together. By default ""no
    func_cycle=10, #minimum time(minutes) the appliance is kept on after switch-on event
)
Phone_charging_TH.windows(window_1=[0, 1440])  # 24 hours

Heating_element_TH = Tumaini_House.Appliance(
    number=1,
    power=1500,  # Power in watts
    num_windows=1,
    func_time=4.65*6*resortOccupancyLevel,  # Actual time the device is used during the day,
        in minutes
    occasional_use=0.3, # Used only on cold days
)
Heating_element_TH.windows(
    window_1=[420, 1320],  # Operational window: 07:00-22:00 in minutes from midnight
)



# Security Lights setup


# Private House Security Lights
LED_lights_PH_SL = Security_Lights.Appliance(
```

```
    number=5,
    power=10,
    num_windows=2,
    func_time=660,  # 11 hours from 7pm to 6am
    fixed="yes"
)
LED_lights_PH_SL.windows(window_1=[0, 360],
window_2=[1140, 1440]
)  # From 7pm to 6am next day

# Staff House Security Lights
LED_lights_SH_SL = Security_Lights.Appliance(
    number=5,
    power=10,
    num_windows=2,
    func_time=660,  # 11 hours
    fixed="yes"
)
LED_lights_SH_SL.windows(window_1=[0, 360], window_2=[1140, 1440])  # 7pm to 6am next day

# Entrance/Parking Security Lights
Entrance_Parking_SL = Security_Lights.Appliance(
    number=10,
    power=10,
    num_windows=2,
    func_time=660,  # 11 hours
    fixed="yes"
)
Entrance_Parking_SL.windows(window_1=[0, 360], window_2=[1140, 1440])

# Stairs Security Lights
Stairs_SL = Security_Lights.Appliance(
    number=6,
    power=10,
    num_windows=2,
    func_time=660,  # 11 hours
    fixed="yes"
)
Stairs_SL.windows(window_1=[0, 360], window_2=[1140, 1440])

# Lower Area Between Stairs and Ocean Security Lights
Lower_Area_SL = Security_Lights.Appliance(
    number=15,
    power=10,
    num_windows=2,
    func_time=660,  # 11 hours
    fixed="yes"
)
Lower_Area_SL.windows(window_1=[0, 360], window_2=[1140, 1440])

# Ferry Lights in Mango Tree
Ferry_Lights_SL = Security_Lights.Appliance(
    number=20,
    power=10,
    num_windows=2,
    func_time=660,  # 11 hours
    fixed="yes"
)
Ferry_Lights_SL.windows(window_1=[0, 360], window_2=[1140, 1440])

# Open Space Security Lights
Open_Space_SL = Security_Lights.Appliance(
    number=6,
    power=10,
    num_windows=2,
    func_time=660,  # 11 hours
    fixed="yes"
)
Open_Space_SL.windows(window_1=[0, 360], window_2=[1140, 1440])
```

```
# Dance Hall setup


# Indoor LED lights
Indoor_LED_lights_DH = Dance_Hall.Appliance(
    number=round(10*resortOccupancyLevel),
    power=10,
    num_windows=1,
    func_time=240,  # 4 hours from 6pm to 10pm
    fixed="no"
)
Indoor_LED_lights_DH.windows(window_1=[1080, 1320])  # 6pm to 10pm in minutes

# Floor fans
Floor_fans_DH = Dance_Hall.Appliance(
    number=round(3*resortOccupancyLevel),
    power=45,
    num_windows=1,
    func_time=180,  # 3 hours from 1pm to 4pm, only on very hot days
    fixed="no",
    occasional_use=0.3  # Assuming use on 30% of days, adjust based on actual hot day
        frequency
)
Floor_fans_DH.windows(window_1=[780, 960])  # 1pm to 4pm in minutes

# Phone charging
Phone_charging_DH = Dance_Hall.Appliance(
    number=round(6*resortOccupancyLevel),
    power=5, # Power consumption of each phone charger in watts
    num_windows=1, # Number of operating windows during the day, which is only at night in
        this case
    func_time=60,
    fixed="no", # If ‘’yes, all the ‘’n appliances of this kind are always switched-on
        together. By default ""no
    func_cycle=10, #minimum time(minutes) the appliance is kept on after switch-on event
)
Phone_charging_DH.windows(window_1=[0, 1440])  # 24 hours




# Workshop setup


# Drill
Drill_WS = Workshop.Appliance(
    number=1,
    power=600,  # Average power consumption for a drill, in watts
    num_windows=1,
    func_time=60,  # Max 1 hour per day
    occasional_use=0.25
)
Drill_WS.windows(window_1=[600, 1080])  # 10am to 6pm in minutes

# Sanding Machine
Sanding_Machine_WS = Workshop.Appliance(
    number=1,
    power=1200,  # Average power consumption for a sanding machine, in watts
    num_windows=1,
    func_time=60,  # Max 1 hour per day
    occasional_use=0.25
)
Sanding_Machine_WS.windows(window_1=[600, 1080])  # 10am to 6pm in minutes

# Circular Saw
Circular_Saw_WS = Workshop.Appliance(
    number=2,
    power=1400,  # Average power consumption for a circular saw, in watts
    num_windows=1,
```

```
    func_time=60,  # Max 1 hour per day
    occasional_use=0.25
)
Circular_Saw_WS.windows(window_1=[600, 1080])  # 10am to 6pm in minutes




# Other category setup


# Pool Pump
Pool_Pump = Other.Appliance(
    number=1,
    power=1225,  # Power consumption in watts
    num_windows=1,
    func_time=120,  # 2 hours from 6am to 8am
)
Pool_Pump.windows(window_1=[360, 480])  # 6am to 8am in minutes

# Water Pump
Water_Pump = Other.Appliance(
    number=1,
    power=750,  # Power consumption in watts
    num_windows=1,
    func_time=60,
)
Water_Pump.windows(window_1=[0, 1440])  # 24 hours

# Projector
Projector = Other.Appliance(
    number=1,
    power=85,  # Power consumption in watts
    num_windows=1,
    func_time=240,  # 4 hours from 7pm to 11pm, but only once a week
    occasional_use= float(1/7)  # Operates 1 time per week
)
Projector.windows(window_1=[1140, 1380])  # 7pm to 11pm in minutes




# Future Cottages setup


# Indoor LED lights
Indoor_LED_lights_FC = Future_Cottages.Appliance(
    number=round(30*resortOccupancyLevel),
    power=10,
    num_windows=1,
    func_time=240,  # 14 hours from 8am to 10pm
    fixed="no"
)
Indoor_LED_lights_FC.windows(window_1=[1080, 1320])  # 8am to 10pm in minutes

# Floor fans
Floor_fans_FC = Future_Cottages.Appliance(
    number=round(3*resortOccupancyLevel),
    power=45,
    num_windows=3,
    func_time=900,  # 15 hours total
    fixed="no"
)
Floor_fans_FC.windows(window_1=[0, 540],
window_2=[780, 960],
window_3=[1260, 1440]
)  # 9pm to 9am and 1pm to 4pm in minutes  # 9pm to 9am and 1pm to 4pm in minutes
```

```
# Computers
Computers_FC = Future_Cottages.Appliance(
    number=round(4*resortOccupancyLevel),
    power=80,
    num_windows=1,
    func_time=120,
    fixed="no"
)
Computers_FC.windows(window_1=[420, 1320])  # 7am to 10pm in minutes

# Phone charging
Phone_charging_FC = Future_Cottages.Appliance(
    number=round(6*resortOccupancyLevel),  # Adjusted based on occupancy level
    power=5,
    num_windows=1,
    func_time=60,  # Assuming actual charging time is concentrated within an hour, though
        available 24 hours
    fixed="no",
    func_cycle=10
)
Phone_charging_FC.windows(window_1=[0, 1440])  # 24 hours

Heating_element_FC = Future_Cottages.Appliance(
    number=1,
    power=1500,  # Power in watts
    num_windows=1,
    func_time=4.65*4*resortOccupancyLevel,  # Actual time the device is used during the day,
        in minutes
    occasional_use=0.3, # Used only on cold days
)
Heating_element_FC.windows(
    window_1=[420, 1320],  # Operational window: 07:00-22:00 in minutes from midnight
)



def plot_load_duration_curve(data, resortOccupancyLevel=1, **kwargs):
    # Sort data in descending order
    sorted_data = np.sort(data)[::-1]
    # Determine x_ticks_frequency and label format based on the length of data
    if len(data) < 2000:
        x_ticks_frequency = 100
        label_format = 'minutes'  # Default to minutes for smaller datasets
    elif len(data) < 20000:
        x_ticks_frequency = 1000
        label_format = 'minutes'
    elif len(data) < 200000:
        x_ticks_frequency = 10000
        label_format = 'hours'  # Change to hours for this dataset size
    else:
        x_ticks_frequency = 30000
        label_format = 'hours'  # Assuming larger datasets might also benefit from hour
            labels

    # Generate the plot
    if resortOccupancyLevel>0.66:
        color='red'
    elif resortOccupancyLevel>0.33:
        color='#ebb734'
    else:
        color='green'
    kwargs.pop('marker', None)  # Ensure no marker conflict
    plt.figure(figsize=kwargs.get('figsize', (10, 6)))
    plt.plot(range(0, len(sorted_data)), sorted_data, marker='', color = color, **kwargs)

    # Calculate x-ticks and set labels based on the selected format
    x_ticks = np.arange(0, len(sorted_data), x_ticks_frequency)
    if label_format == 'hours':
        x_tick_labels = [f"{tick/60:.0f}" for tick in x_ticks]  # Convert minutes to hours
        plt.xticks(x_ticks, x_tick_labels)
```

```
    else:
        plt.xticks(x_ticks)

    plt.xlabel('Duration (Ranked Order)' + (' (Hours)' if label_format == 'hours' else ' (
        Minutes)'))
    plt.ylabel('Load (W)')
    plt.title('Load Duration Curve')
    plt.grid(True)
    plt.show()




if __name__ == "__main__":
    from ramp.core.core import UseCase

    uc = UseCase(
        users=User_list,
        parallel_processing=False,
    )
    uc.initialize(peak_enlarge=0.15)

    Profiles_list = uc.generate_daily_load_profiles(flat=False)

    # post-processing
    from ramp.post_process import post_process as pp

    Profiles_avg, Profiles_list_kW, Profiles_series = pp.Profile_formatting(
        Profiles_list
    )

    plot_load_duration_curve(Profiles_series, resortOccupancyLevel=resortOccupancyLevel)

    # Define the base path for the output files
    base_path = 'C:/Users/volodin/Desktop/googlesync/thesis/RAMP2/RAMP-main/ramp/example/'
    # Format the occupancy level as a string, replacing '.' with '_' for the filename
    occupancy_str = str(resortOccupancyLevel).replace('.', '_')
    # Construct the output filename incorporating the occupancy level
    ofname = f'{base_path}Profiles_Series_occupancy_{occupancy_str}.csv'

    pp.export_series(Profiles_series, ofname=ofname)
    pp.Profile_series_plot(
        Profiles_series
    )  # by default, profiles are plotted as a series
    if (
        len(Profiles_list) > 1
    ):  # if more than one daily profile is generated, also cloud plots are shown
        pp.Profile_cloud_plot(Profiles_list, Profiles_avg)

    print(str(np.mean(Profiles_avg)))
```